AFOSR-TR-96

C321

SC71062.FTR

Development of Combined Asymptotic and Numerical Procedures for Transonic and Hypersonic Flows

Final Technical Report

November 01, 1991 thru December 31 1995

Contract No. F49620-92-C-0006

Prepared for:
Air Force Office of Scientific Research, AFOSR/NM
Directorate of Mathematical and Information Sciences
Bldg 410
Bolling, AFB, DC 20332-6448
Attn: Dr. A. Nachman

Prepared by:
N. Malmuth, A. Fedorov, A. Khokhlov and J. Cole
Rockwell Science Center
1049 Camino Dos Rios
Thousand Oaks, CA 91360
April 1996

19960626 033

Rockwell

Science Center

DTIC QUALITY INSPECTED 1

Copy # 2

ADA310408

DISCLAIMER NOTICE

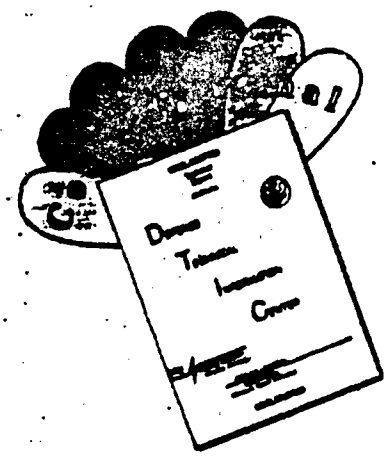

THIS DOCUMENT IS BEST QUALITY AVAILABLE. THE COPY FURNISHED TO DTIC CONTAINED A SIGNIFICANT NUMBER OF COLOR PAGES WHICH DO NOT REPRODUCE LEGIBLY ON BLACK AND WHITE MICROFICHE.

REPORT DOCUMENTATION PAGE

Form Approved
OMB No. 0704-0188

Public reporting burden for this collection of information is estimated to average 1 hour per response, including the time for reviewing instructions, searching existing data sources, gathering and maintaining the data r eeded, and completing and reviewing the collection of information. Send comments regarding this burden estimate of any other aspect of this collection of information, including suggestions for reducing this burden, to Washington Headquarters Services, Directorate for Information Operations and Reports, 1215 Jefferson Davis Highway, Suite 1204, Arlington, VA 22202-4302, and to the Office of Management and Budget, Paperwork Reduction Project (0704-0188), Washington, DC 20503

1. AGENCY USE ONLY (Leave Blank)	2. REPORT DATE	3. REPORT TYPE AND DATES COVERED
	23 April 1996	Final Report, 01 Nov 91—31 Dec 95

4. TITLE AND SUBTITLE
Development of Combined Asymptotic and Numerical Procedures for Transonic and Hypersonic Flows

5. FUNDING NUMBERS
CF49620-92-C-0006

4. AUTHOR(S)
N.D. Malmuth, A.V. Fedorov, A. Khokhlov, and J.D. Cole

7. PERFORMING ORGANIZATION NAME(S) AND ADDRESS(ES)
Rockwell International
Science Center
1049 Camino Dos Rios
Thousand Oaks, CA 91360

7. PERFORMING ORGANIZATION REPORT NUMBER
SC71062.FTR

9. SPONSORING / MONITORING AGENCY NAME(S) AND ADDRESS(ES)
Air Force Office of Scientific Research
AFOSR/NM
Directorate of Mathematical and Information Sciences
Bldg 410
Bolling AFB, DC 20332-6448

9. SPONSORING / MONITORING AGENCY REPORT NUMBER

11. SUPPLEMENTARY NOTES

12a. DISTRIBUTING/AVAILABILITY STATEMENT

12b. DISTRIBUTION CODE

13. ABSTRACT *(Maximum 200 Words)*

Hypersonic and transonic flows of practical interest were investigated using combined asymptotic and numerical methods. In the hypersonic regime, strong, moderate and weak interaction between shock and boundary layers were emphasized in relation to stability and transition. A new instability was identified in which disturbances reflect from the boundary layer edge of a waveguide formed by the boundary layer and a flat plate. Other new amplification phenomena were discovered related to three-dimensional disturbances and finite amplitude fluctuations in thin Newtonian shock layers. It was shown that the latter can produce inflectional instabilities that can be exploited to enhance mixing in scramjet combustors. Similitudes were used to collapse Reentry-F cone data to a universal curve, forming a basis for quick-response hypersonic transition prediction. Another theoretical analysis showed that ultrasonically absorptive thermal protection surfaces can damp inviscid second-mode acoustic instabilities with the possibility of transition control. In the transonic speed range, an area rule for wall interference was developed as well as asymptotic theories for lifting interference and the effect of non circular walls. These provide systematic approximation procedures for quick correction methods and optimal model sizing for maximum unit Reynolds number and minimum wall interference.

14. SUBJECT TERMS	15. NUMBER OF PAGES
Hypersonic, transonic flow, asymptotic expansions, wind tunnel wall interference, theoretical aerodynamics, fluid dynamics, shock waves, stability, transition	132
	16. PRICE CODE

17. SECURITY CLASSIFICATION OF REPORT	18. SECURITY CLASSIFICATION OF THIS PAGE	19. SECURITY CLASSIFICATION OF ABSTRACT	20. LIMITATION OF ABSTRACT
UNCLASSIFIED			

NSN 7540-01-280-5500
F-0046-SC

Standard Form 298 (Rev. 2-89)
Prescribed by ANSI Std. Z39-18 298-102

ADA310406

TABLE OF CONTENTS

TABLE OF CONTENTS (CONT'D)

List of Figures

List of Figures, (cont'd)

List of Figures, (cont'd)

List of Figures, (cont'd)

List of Figures, (cont'd)

1. Executive Summary

1.1 Survey of effort

This document summarizes effort conducted under the contract F49620-92-C-0006, "Development of Combined Asymptotic and Numerical Procedures for Transonic and Hypersonic Flows." In the hypersonic portion of the effort, stability and transition, unsteady aerodynamic characteristics and stability, strong inviscid/viscous interactions and potential application of instabilities to scramjet combustors were emphasized. Major aspects of the work included a study of three-dimensional disturbances in hypersonic boundary layers. These are particularly important to scramjet inlet design. We have investigated low frequency instabilities of viscous hypersonic flow over a flat plate using triple-deck methods. Our eigensolutions indicate the existence of an upstream propagating stable mode which is the unsteady counterpart of the steady two-dimensional Neiland-Brown-Stewartson solutions. We have also discovered a downstream-propagating unstable mode. This leads to a three-dimensional instability and is controlled moderately supersonic flow physics. Calculations of growth rates and analysis of the forced problem for the experimentally significant time-harmonic vibrator show that at sufficiently low frequencies, the downstream far field transverse projection consists of Gaussian lobes symmetrically displaced about the source axis. For frequencies exceeding a critical value, only one lobe occurs. The width of this lobe contracts, in contrast to the expansion of conventional wakes. For wavelengths of the order of the boundary layer thickness and phase speeds less than unity, we have discovered new waveguide reflectional instability mechanisms that can be important for strong, moderate and weak interaction between the shock and boundary layers. These results can be readily extended to three-dimensional flows. Our asymptotic analyses show that to first order in the displacement thickness, the upper boundary layer edge behaves as a solid wall that reflects boundary-layer disturbances. This is a viscous generalization of energy trapping instability mechanisms discussed by the Principal Investigator in an inviscid context in [C1]. These compete with other more well known instability modes that produce premature transition and are therefore of importance to hypersonic design and propulsion-airframe integration. In addition to this boundary layer "lower" wave guide, and "upper" one exists between the shock and the sonic line. At mode synchronism points between upper and lower wave guides, singular growth spikes occur that invalidate the modal decomposition used in state-of-the-art linear stability/transition prediction theories/codes. **The waveguide concepts have been studied in connection with control of transition by absorbing walls and demonstrated reduction of amplification with increased wall absorption. From the stability asymptotics, practical transition delay concepts have been identified using conventional thermal protection materials having ultrasonically selective properties.** For thin shock layers, we have extended steady Newtonian asymptotic theory to the unsteady case. **We have used the theory to demonstrate the existence of a new finite-amplitude inflectional instability that may be useful to promote pre-mixing and enhanced burning efficiency for scramjet combustors.** The unsteady Newtonian model is useful in other contexts such as hypersonic aeroelasticity and flutter. **As another application of our hypersonic**

theories, similitudes have been used to collapse re-entry cone transition data to provide an efficient prediction tool for the scientist, engineer and designer. In the transonic regime, we have developed the basis for wind tunnel wall interference predictions for slender and not-so-slender bodies in wind tunnels. The singular perturbation theory is interacting with experiments that we are conducting in the Russian TsAGI T-128 wind tunnel leading to the generalization of our Transonic Area Rule for Wind Tunnel Wall Interference (TARWI) to test articles of length comparable to the wall height. The TsAGI tests have validated our matched asymptotics derivation of the TARWI. **The TARWI reduces the three-dimensional wall interference correction problem to one in two-dimensions.** This will provide test engineers a basis for estimation of transonic blockage corrections and optimization of model size for maximum unit Reynolds number and minimum wall interference. Also to be described in what follows are other theories for lift interference in porous wind tunnels as well as corrections for non-circular walls that we have derived in the effort. To our knowledge, this is the first time such corrections have been embedded in systematic asymptotic approximation procedures.

1.2 Personnel associated with research effort

- Dr. Norman D. Malmuth
- Professor Julian D. Cole
- Dr. Alexander V. Fedorov
- Dr. André Khokhlov
- Professor Vladimir Ya Neiland
- Dr. Vera M. Neyland
- Professor Oleg Ryzhov

1.3 Cumulative list of publications associated with effort

C1. Malmuth, N.D. "Stability of the inviscid shock layer in strong interaction flow over a hypersonic flat plate," in *Instabilities and Turbulence in Engineering Flows*, eds. D.E. Ashpis, T.B. Gatski and R. Hirsh. Kluwer Academic Publishers, 1993.

C2. Malmuth, N.D., Jafroudi, H., Wu, .C.C, McLachlan, R. and Cole, J.D. "Asymptotic methods applied to transonic wall interference," *AIAA J.* **31** 5, pp. 911-918, May 1993.

C3. Malmuth, N. "Unsteady hypersonic thin shock layers and flow stability," invited paper at Wright Patterson Hypersonics Meeting, Wright Patterson AFB OH, May 17-19, 1993 also invited paper International Workshop on Modeling of Aerodynamic Flows, Hotel Amber Baltic, Miedzyzdroje, Poland, July 12-14, 1993 in *Advances in analytical Methods in Modeling Aerodynamic Flows*, edited by J.D.A. Walker, M. Barnett and F.T. Smith. AIAA , 1994.

C4. Fedorov A. and N. Malmuth, "High Mach number similarity in the prediction of boundary layer transition on circular cones," *AIAA J.*, 33 8, August 1995, 1523.

C5. Malmuth, N.D. Neyland, V.M. and Neiland, V. Ya "Wall Interference Over Small and Large Aspect Ratio Wings in Wind Tunnels," *invited paper*, Second Pacific International Meeting in Aerospace Technology PICAST2-AAC6, *in peer-reviewed proceedings*, Melbourne, Australia, March 1995.

C6. Malmuth, N.D.and Cole, J.D. "Wind tunnel wall interference involving slender wings and non-circular walls," 1st Theoretical Fluid Dynamics Meeting, New Orleans, LA, June, 1996.

C7. Khokhlov, A.P. and Malmuth, N.D. "Low Frequency Instability of Hypersonic Interactive Boundary Layers on a Cooled Surface," submitted to the *Journal of Fluid Mechanics*, 1996.

C8. Malmuth, N.D., Crites, R., Everhart, J. and Sickles, W., "Transonic wind tunnel wall interference," invited chapter in *AGARDOgraph* 336-17-94 , 1996.

2. Mechanism of Hypersonic Flow Stabilization by a Semi-Transparent Wall

2.1 Introduction

The ability to predict and control the location of boundary layer transition is of critical importance in the design and optimization of aerospace vehicles [1]. Transition causes significant increases in heat transfer and skin friction. This leads to diminished vehicle performance, primarily because of the additional weight of thermal protection system (TPS).

If external disturbances are small and the TPS roughness is negligible, then the transition process is due to amplification of unstable modes in the boundary layer [1], [2]. In this case, stability theory and experiment form a foundation for the prediction and control of transition [3], [4], [5]. Several different instability mechanisms may be responsible for transition on the hypersonic vehicle surface, namely

1. the first and second modes which are dominant in 2-D or quasi 2-D boundary layers on a flat plate, axisymmetric bodies, wings, etc.
2. Gortler vortices which can play a major role on concave surfaces.
3. cross flow instability which can be dominant in 3-D boundary layers on the leading edge of a swept wing, axisymmetric bodies at the angle of attack, *etc.*

Our analysis addresses the mechanism in Item (1). Its relation to other types of instability will be discussed at the end of this chapter.

The first mode is an extension to high speeds of the Tollmien-Schlichting waves. They represent viscous instability at low Mach numbers. However the inviscid nature of the first mode begins to dominate when the Mach number increases, since the compressible boundary layer profiles contain a generalized inflection point [3]. This mode may be stabilized by wall cooling, suction and favorable pressure gradient.

The second mode is the result of an inviscid instability present due to a region of supersonic mean flow relative to the disturbance phase velocity. It belongs to the family of trapped acoustic modes. For an insulated surface, these higher modes appear for Mach numbers $M > 2.2$. However, it is not until the Mach number is of the order of 4 or greater that the second mode is at low enough frequency to have experimental consequences. Once the second mode sets in, it becomes the dominant instability since its growth rate tends to exceed that of the first mode. For insulated surfaces, this occurs for $M > 4$. For cooled surfaces, the second mode can dominate at even lower Mach numbers. In contrast to the first mode, the higher subsonic modes are destabilized by cooling. The existence of the second modes was established by the experiments of

Kendall [6], Demetriades [7], and Stetson et al. [8]-[10]. The most amplified second mode wavelengths tend to be approximately twice the boundary layer thickness, and the second mode phase velocities tend to be approximately equal to the edge velocity of mean flow.

The second mode induces pressure disturbances of very high frequency. For example, the most amplified waves observed in the experiment of Stetson *et al.* [8] at Mach 8 correspond to a frequency of about 100 kHz. TPS porous surfaces can absorb these high frequency fluctuations. It is assumed that **the absorption can cause stabilization of the second and higher modes by this energy extraction mechanism.** This assumption has been examined in a theoretical study that is summarized in what follows. The eigenvalue problem for inviscid disturbances in a supersonic boundary layer is formulated in Section 2.2.* The WKB method is used to specify the boundary condition on the semi-transparent wall for the acoustic normal modes of high frequency including the second mode. In Section 2.3, the eigenvalue problem is solved numerically and it is shown that absorption stabilizes the second mode. A discussion of the future effort concludes this chapter.

2.2 Eigenvalue problem for inviscid disturbances

A supersonic boundary-layer flow over a flat plate or sharp cone schematically shown in Fig. 1 is considered. The coordinates x, y are made nondimensionless using the boundary layer displacement thickness δ^*. In the locally parallel approximation, the mean flow is characterized by the profile of x-component velocity $U(y)$ and temperature $T(y)$ nondimensionalized using their corresponding reference quantities U_e and T_e at the upper boundary layer edge. The inviscid stability equations are obtained from the linearized, parallel flow, viscous equations for a perfect gas with constant specific heat by setting all viscous and heat-conduction terms equal to zero [11]. Since the second, third and higher modes have maximum growth rate in the two-dimensional case†, we consider 2-D disturbances in normal-mode form as

$$[\tilde{u},\tilde{v},\tilde{p},\tilde{\theta}]^T(x,y,t) = [u,v,p,\theta]^T(y)\exp[i(\alpha x - \omega t)] \qquad (1)$$

where $\tilde{u}$ and $\tilde{v}$ are the velocity components in the x and y directions, $\tilde{p}$ is the pressure normalized by the dynamic pressure, $\rho_e U_e^2$, $\tilde{\theta}$ is the temperature, α is the wavenumber, and ω is frequency.

---

* This work and a portion of that described in the other chapters was partially funded by other sources in addition to the contract.

† This is also termed the most dangerous case.

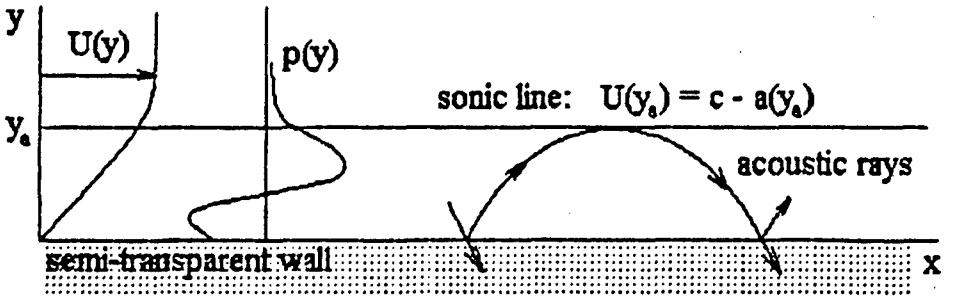

Fig. 1 Acoustic mode in a supersonic boundary layer on semi-transparent wall.

The system of equations for $v(y)$ and $p(y)$ (see for example [11]) is

$$\left.\begin{aligned} v' &= \frac{U'}{U-c}v + i\alpha\left(\frac{T - M^2(U-c)^2}{U-c}\right)p \\ p' &= -i\alpha\left(\frac{U-c}{T}\right)v. \end{aligned}\right\} \qquad (2)$$

where $c = \omega / \alpha$ is the phase speed, and prime denotes the derivative with respect to y. The boundary conditions for Eqs. (2) are

$$v(0) = A \cdot p(0) \qquad (3)$$

$$p(\infty) = 0 \qquad (4)$$

Equation (3) is a general form (Darcy's Law) of the inviscid boundary condition on porous or compliant walls. The coefficient A is a complex quantity which depends on properties of the wall material, mean flow characteristics on the wall surface, and flow perturbation parameters such as a wave frequency and wavelength. Note that the boundary condition (4) requires the normal mode to vanish outside the boundary layer. The eigenvalue problem (2)-(4) provides the dispersion relation $F(\alpha,\omega) = 0$. For temporal stability, the wavenumber α is real, and $\omega(\alpha)$ is the complex eigenvalue. If $\mathrm{Im}(\omega) > 0$, then the disturbance is unstable.

The system of equations (2) can be reduced to one equation for the pressure amplitude

$$p'' - \left(\frac{2U'}{U-c} - \frac{T'}{T}\right)p' + \lambda^2 p = 0$$
$$\lambda^2 = \alpha^2\left[\frac{M^2(U-c)^2}{T} - 1\right] \tag{5}$$

with the following boundary conditions

$$p'(0) = A\cdot\frac{ic\alpha}{T(0)}p(0) \tag{6}$$
$$p(\infty) = 0 \tag{7}$$

According to the asymptotic analysis [12] characteristics of the second, third and higher modes can be obtained by the WKB method. Without going into details, we briefly describe the results of this analysis. For a subsonic disturbance with phase speed

$$1 - \frac{1}{M} < \mathrm{Re}(c) < 1 + \frac{1}{M} \tag{8}$$

the boundary layer behaves as an acoustic waveguide schematically shown in Fig. 1. In the waveguide region between the wall and the sonic line: $y = y_a, U(y_a) = \mathrm{Re}(c) - a(y_a)$, the pressure amplitude $p(y)$ oscillates in the y direction. Here the real part of the function $\lambda(y)$ is large and positive, and hence the solution of Eq. (5) can be expressed in the following WKB form

$$p(y) = \left[\hat{p}_1(y)\exp\left(-i\int_0^y \lambda dy\right) + \hat{p}_2(y)\exp\left(i\int_0^y \lambda dy\right)\right] + O(\varepsilon) \tag{9}$$

$$\hat{p}_{1,2}(y) = Const_{1,2}\frac{U-c}{\sqrt{T}}q^{-1/4}, q = \frac{M^2(U-c)^2}{T} - 1$$

where $\varepsilon = 1/\max(|\lambda|)$ is a small parameter. The first and second terms respectively represent incident and reflected acoustic waves to the wall. Near the sonic line, the acoustic ray turns around as schematically shown in Fig. 1. In the upper region $y > y_a$, the real part of $\lambda(y)$ is negative and the pressure amplitude decays exponentially. For the neutral modes, the dispersion relation obtained by the WKB method has the following form for the case of a non-transparent wall ($A = 0$)

$$\int_0^{y_1} \sqrt{\frac{M^2(\alpha U-\omega)^2}{T}-\alpha^2}\,dy=\frac{\pi}{4}+\pi\cdot n \qquad (10)$$

The solution of Eq. (10), $\omega_n(\alpha)$, corresponds to the second mode for $n=0$, to the third mode at $n=1$ etc.

To obtain the explicit form of the coefficient A on a semi-transparent wall, we use the WKB approximation (9). The reflection coefficient τ is defined as

$$\tau=\frac{\hat{p}_2(0)}{\hat{p}_1(0)}. \qquad (11)$$

If $\tau=1$, then disturbances are completely reflected by the wall. If $\tau<1$, then some portion of the disturbance energy is absorbed by the wall material. Differentiating the expression (9) we obtain in the first order approximation

$$p'(0)=-i\lambda(0)\cdot[\hat{p}_1(0)-\hat{p}_2(0)] \qquad (12)$$

Substituting (12) into the boundary condition (6) and using Eqs. (9), (11), we get

$$p'(0)=-i\lambda(0)p(0)\cdot\frac{1-\tau}{1+\tau} \qquad (13)$$

From Eqs. (6), (13) we obtain the explicit form for the absorption coefficient

$$A=-\frac{T(0)}{c}\sqrt{\frac{M^2c^2}{T(0)}-1}\,\frac{1-\tau}{1+\tau} \qquad (14)$$

2.3 Results and discussion

The eigenvalue problem (2)-(4) is solved by numerical integration using the method of Mack [11]. The absorption coefficient A is specified by the expression (14). The integration starts at the upper freestream and continues to the wall along an indented contour in the complex plane. The contour lies below the critical point $y_c: U(y_c)=c$. The eigenvalue $\omega(\alpha)$ is found by the iterative Newton method.

In Fig. 2, the second-mode growth rate $\mathrm{Im}(\omega)$ is shown as a function of the wavenumber α, at various values of the reflection coefficient τ. Calculations were performed for the flat-plate boundary layer on a cool wall with a temperature ratio typical of a hypersonic vehicle surface. Here, T_w is the surface temperature, and T_{ad} is the temperature ratio $T_w / T_{ad} \approx 0.2$ on an adiabatic wall. The freestream parameters have the following values: Mach number $M = 6$, specific heat ratio $\gamma = 1.4$, and Prandtl number $\mathrm{Pr} = 0.72$. It is seen that the semi-transparent wall reduces the growth rate by the factor of 4 at the reflection coefficient $\tau = 0.6$. A similar stabilization effect has been obtained for other Mach numbers, and wall temperatures. Since the physics of the third and higher modes is similar to that of the second mode, it is assumed that the absorption of acoustic energy can cause similar stabilization of these higher modes.

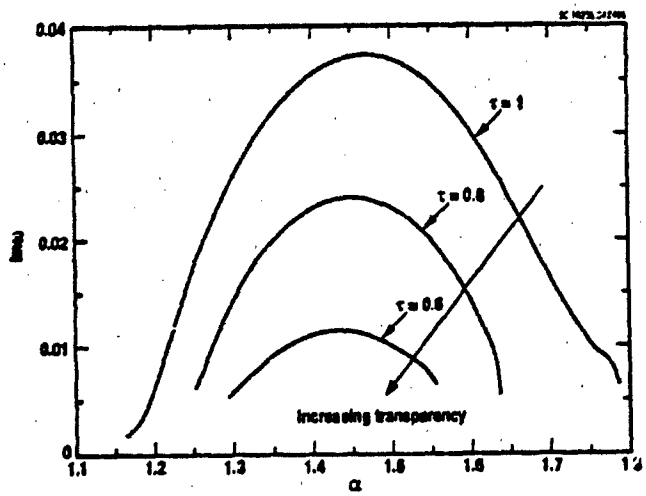

Fig. 2 Effect of the wall reflection coefficient τ on the second mode growth rate $\mathrm{Im}(\omega)$ for hypersonic boundary layer at $M = 6$, $T_w / T_{ad} = 0.1986$, $\mathrm{Pr} = 0.72$, and $\gamma = 1.4$.

2.4 Conclusions

1. According to inviscid stability theory, the absorption of acoustic energy by a semi-transparent wall can essentially stabilize the second mode of a hypersonic boundary layer. This stabilization may lead to delay of transition on hypersonic vehicle surfaces.

2. Since frequency of pressure disturbances incident on the wall by the second mode are very high (of the order of 100 kHz), TPS porous materials used on hypersonic vehicle

surfaces can be semi-transparent with respect to these disturbances. It is this property that provides an opportunity to use absorption to maintain or increase the laminar flow run.

Since the boundary layer stabilization is due to the absorption of disturbance energy by the wall, we believe that a similar effect may occur for other high-frequency instabilities such as unsteady cross flow vortices. A semi-transparent wall may also affect transition past TPS roughness elements. It is recommended that these assumptions be verified by wind tunnel experiments using models with porous surfaces.

In our analysis, we have used a simple model for the boundary condition on a semi-transparent wall. This model permits rough estimates of the absorption effect and formulations for its experimental verification. For reliable quantitative results, more comprehensive models of the absorption mechanism as well as detailed experimental studies are required. In order to demonstrate the effect of transition delay on a semi-transparent surface and apply it to hypersonic vehicle design, the following effort should be performed:

- Test current TPS materials and obtain their transparency characteristics in a frequency band relevant to hypersonic instability

- Demonstrate the effect of surface transparency on transition by experiment on models of a simple shape (such as a flat plate or sharp cone) in hypersonic wind tunnels

- If the demonstration is successful:

  - Develop theoretical models accounting for viscous effects as well as physics of interaction between the flow disturbance and the TPS material microstructure.
  - Conduct detailed experiments in hypersonic wind tunnels.
  - Perform flight testing.
  - Develop new TPS materials providing maximum stabilization of hypersonic boundary layer and transition delay.

2.5 References

1. Malik, M.R., Zang, T.A., and Bushnell, D.M., "Boundary Layer Transition in Hypersonic Flows," AIAA Paper No. 90-5232, 1990.

2. Reshotko, E., "Boundary Layer Instability, Transition and Control," AIAA Paper No. 94-0001, 1994.

3. Mack, L.M., "Boundary-Layer Stability Theory," Special Course on Stability and Transition of Laminar Flow, edited by R. Michel, AGARD Rep. No. 709, pp. 3-1 to 3-81, 1984.

4. Reshotko, E., "Stability Theory as a Guide to the Evaluation of Transition Data," *AIAA J.*, 7 6, pp. 1086-1091, 1969.

5. Malik, M.R., "Prediction and Control of Transition in Supersonic and Hypersonic Boundary Layers," *AIAA J.* 27 11, pp. 1487-1493, 1989.

6. Kendall, J.M., "Wind Tunnel Experiments Relating to Supersonic and Hypersonic Boundary-Layer Transition," *AIAA J.* 13 3, pp. 290-299, 1975.

7. Demetriades, A., "Hypersonic Viscous Flow over a Slender Cone, Part III: Laminar Instability and Transition," AIAA Paper No. 74-535, 1974.

8. Stetson, K.F., Thompson, E.R., Donaldson, J.C., and Siler, L.G., "Laminar Boundary Layer Stability Experiments on a Cone at Mach 8, Part 1: Sharp Cone," AIAA Paper No. 83-1761, 1983.

9. Stetson, K.F., and Kimmel, R.G., "On the Breakdown of a Hypersonic Laminar Boundary Layer," AIAA Paper No. 93-0896, 1993.

10. Kimmel, R., Demetriades, A., and Donaldson, J., "Space-Time Correlation Measurements in a Hypersonic Transitional Boundary Layer," AIAA Paper No. 95-2292, 1995.

11. Mack, L.M., "Boundary Layer Stability Theory," JPL Rep. No. 900-277, Rev. B, Pasadena, California, 1969.

12. Gushchin, V.R., and Fedorov, A.V., "Asymptotic Analysis of Inviscid Perturbations in a Supersonic Boundary Layer," *Zhurnal Prikladnoi Mekhaniki i Tekhnicheskoi Fiziki*, No. 1, pp. 69-75, 1989 (translated in English).

3. Reflectional Instability of a Hypersonic Boundary Layer

3.1 Introduction

The hypersonic speed range contains some of the most important problems in boundary layer transition. At high Mach numbers, early transition causes temperatures high enough to destroy air vehicle surfaces. Uncertainty in the transition locus leads to diminished performance, primarily because of the additional weight of the thermal protection system. This has stimulated considerable experimental and theoretical studies. The transition problem is an initial boundary value problem which requires the identification of the freestream disturbance field, understanding of the laminar flow receptivity to external disturbances including surface irregularities, as well as linear and nonlinear amplification of unstable disturbances [1]. Current knowledge is inadequate to solve and apply the initial value problem to design, even at low speeds. However, it has been found that transition can be correlated with linear stability theory if the external-disturbances are relatively small. This motivates development of hypersonic flow stability theory.

Hypersonic instability is more complicated than for moderate speeds. In addition to Tollmien-Schlichting waves, cross flow and Görtler vortices, the following special observations apply at high Mach numbers:

- In the region of the boundary layer that is supersonic relative to the phase velocity, Mack [2] showed that multiple solutions of the inviscid stability equations occur. These additional solutions are called higher modes. Physically they represent acoustic modes which propagate in a "waveguide" located between the wall and the sonic line. The first mode of this family, which is called the second mode, is the most unstable. Its wavelength is of the order of boundary layer thickness.

- Fedorov and Khokhlov [3] demonstrated that the second mode instability is related to synchronization between the first and second modes. Near the synchronism point, where frequencies and phase speeds of both modes coincide, the eigenvalues split into two branches. In the vicinity of branch points the dispersion relation is singular, causing a strong exchange between modes due to nonparallellism. This implies that a multi-mode approach is required for transition prediction rather than the conventional single mode method.

- If the shock wave is close to the surface, which is relevant to the windward side of re-entry vehicle at the high angle of attack, a new class of unstable modes occurs due to reflection of disturbances by the shock. Qualitative asymptotic analyses of Fedorov and Gushchin [4], [5] showed that, in addition to the lower waveguide of the boundary layer, there is an upper waveguide located between the shock wave and the sonic line. At certain conditions acoustic waves of the lower waveguide are in resonance with those of the upper waveguide and have identical phase speeds. The synchronization between modes causes a new type of instability.

- In the hypersonic limit, the inflectional instability is related to a thin transitional layer located near the upper boundary layer edge. This inviscid instability is called the vorticity mode. It has been studied by Blackaby, Cowley and Hall [6], Smith and Brown [7], Grubin and Trigub [8] using asymptotic methods. They analyzed stability of the hypersonic flow over a flat plate for weak and strong viscous-inviscid interaction. It has been found that the vorticity mode weakly disturbs the flow outside the transitional layer which separates a hot flow of the boundary layer from a cool inviscid flow. The phase speed of the vorticity mode tends to unity with increasing Mach number. Its wavelength is much less than the boundary layer thickness.

- Malmuth [9] studied disturbance flowfield in a thin shock layer between the shock wave and the upper boundary layer edge. He examined the strong interaction regime on a flat plate at the Newtonian limit when the specific heat ratio $\gamma \to 1$. His studies show that disturbances of longitudinal scale of the order of the length of the strong interaction region can strongly amplify in a thin shock layer. This new instability does not relate to the normal-mode decomposition normally used in stability theory. It was revealed only by solving the complete initial boundary value problem for strongly nonparallel flow.

- Hypersonic flow past a blunt body generates a strong curved shock near the nose. This causes an entropy layer in the inviscid region between the shock and the boundary layer. As the shock wave approaches the limit of a sharp cone solution, the entropy layer thickness decreases and eventually it is swallowed by the boundary layer. The entropy layer can be unstable due to presence of the inflection point [5], [10]. Reshotko and Khan [10] found that within the swallowing region, the boundary layer stability is affected by the nonuniform flow near the boundary layer edge. The interplay between the entropy modes and the boundary modes may strongly affect their amplification.

Coexistence of several instabilities of essentially different scale make it difficult to predict transition from a universal stability code. Computations of the hypersonic mean flow and its stability from codes developed for moderate Mach number flows are very time-consuming. Computational time and intensity grows dramatically with increasing Mach number because of the strong non-uniformity of hypersonic mean flow profiles and the high sensitivity of the related eigenvalue problem to its first and second derivatives [1]. Solution procedures based on combined asymptotics and numerics deal effectively with this difficulty since they systematically guide accurate resolution of the high gradient regions in a robust way. This has stimulated the research described here.

Asymptotic models have been developed to treat the short-scale vorticity mode of the transitional layer in [6] - [8], and large-scale disturbances in [9] of the inviscid shock layer. Both instabilities convect with a phase speed close to the freestream velocity. The intermediate case in which the disturbance scale is of the order of boundary layer thickness and its phase speed is less than the freestream speed has not been studied by

asymptotic methods. This gap is targeted in the analysis that follows. In Section 3.2, the composite system of stability equations for a strong interaction hypersonic boundary layer is derived. The disturbance field in the inviscid shock layer is treated in Section 3.3. In Section 3.4, matching between the boundary layer and shock layer is used to establish boundary conditions at the upper boundary layer edge. The weak interaction case is considered in Section 3.5. Section 3.6 generalizes consideration of the eigenvalue problem to 3-D mean flows and fluctuations. In Section 3.7, a self-similar solution for steady strong interaction boundary-layer flow is obtained. These mean flow profiles are used for stability computations in Section.3.8.

3.2 Stability equations in the strong interaction boundary layer

Consider the boundary layer on a flat plate in hypersonic flow of a perfect gas (see Fig. 1) with speed U_∞^*, temperature T_∞^*, and density ρ_∞^*. Introduce nondimensional coordinates and time as

$$(x,y)=(x^*,y^*)/\delta^*, t=t^*/(\delta^*/U_\infty^*). \tag{1}$$

where δ^* is of the order of the boundary layer thickness. The pressure p^*, temperature, density and the velocity components u^*, v^* are nondimensionalized as

$$\hat{p}=\frac{p^*}{\rho_\infty^* U_\infty^{*2}}, \hat{T}=\frac{T^*}{T_\infty^*}, \hat{\rho}=\frac{\rho^*}{\rho_\infty^*}, (\hat{u},\hat{v})=\frac{(u^*,v^*)}{U_\infty^*}. \tag{2}$$

Besides the fast variable x, a slow variable x_1 corresponding to the longitudinal scale L^* (see Fig. 1) is introduced, where

$$x_1=\delta\cdot x, \delta=\frac{\delta^*}{L^*}. \tag{3}$$

Consider the following hypersonic limit corresponding to the strong interaction between inviscid flow and boundary layer (see for example Bush [11])

$$\delta\to 0, M\to\infty, \delta^2 M^2\to\infty, (\gamma-1)=O(1), \tag{4}$$

where γ is the specific heat ratio. In this case, the shock-layer thickness δ_s is of the order of the boundary layer thickness δ^*.

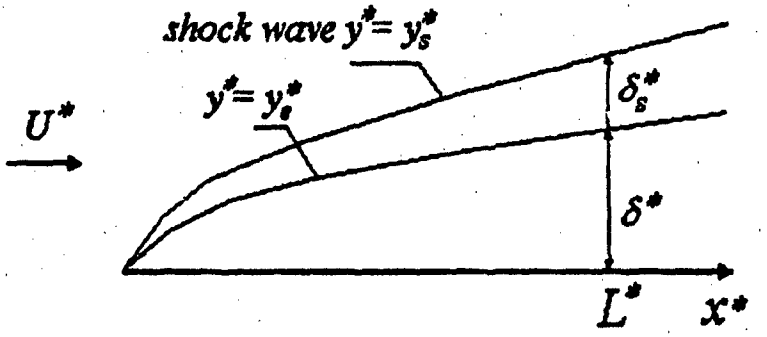

Fig. 1 Hypersonic strong interaction flow over a flat plate.

The mean flow and its unsteady perturbations are represented asymptotically as

$$
\begin{aligned}
&\hat{p}(x,y,t) = \delta^2\left[P_s(x_1) + \varepsilon\cdot p(x,x_1,y,t)\right] + \cdots \\
&\hat{\rho}(x,y,t) = \frac{\gamma}{\gamma-1}\delta^2\left[\rho_s(x_1,y) + \varepsilon\cdot \rho(x,x_1,y,t)\right] + \cdots \\
&\hat{T}(x,y,t) = (\gamma-1)M^2\left[T_s(x_1,y) + \varepsilon\cdot T(x,x_1,y,t)\right] + \cdots \\
&\hat{u}(x,y,t) = U_s(x_1,y) + \varepsilon\cdot u(x,x_1,y,t) + \cdots \\
&\hat{v}(x,y,t) = \delta\cdot V_s(x_1,y) + \varepsilon\cdot v(x,x_1,y,t) + \cdots \\
&\hat{\mu} = \hat{T}^n = \left[(\gamma-1)M^2\right]^n\left[\mu_s(x_1,y) + \varepsilon\cdot\frac{d\mu_s}{dT_s}T(x_1,y,t)\right] + \cdots \\
&\mu_s = T_s^n(x_1,y).
\end{aligned}
\tag{5}
$$

In (5), ε is a small parameter characterizing the disturbance amplitude, $\hat{\mu} = \mu^*/\mu_\infty^*$ is the normalized viscosity and the temperature-viscosity dependence is approximated by the power law with the exponent n. With the exception of the vertical velocity v, these expansions resemble those of Bush [11] for steady flow. Since the disturbance scale is of the order of boundary layer thickness, the pressure perturbation is not constant across the layer and induces the vertical velocity perturbation $v = O(1)$.

Substitution of (5) into Navier-Stokes equations and linearization gives a linear system. In particular, the continuity equation yields

$$
\begin{aligned}
&\frac{\partial\rho}{\partial t} + \rho_s\frac{\partial u}{\partial x} + U_s\frac{\partial\rho}{\partial x} + \rho_s\frac{\partial v}{\partial y} + v\frac{\partial\rho_s}{\partial y} + \\
&+\delta\left(\rho_s\frac{\partial u}{\partial x_1} + U_s\frac{\partial\rho}{\partial x_1} + u\frac{\partial\rho_s}{\partial x_1} + \rho\frac{\partial U_s}{\partial x_1} + V_s\frac{\partial\rho}{\partial y} + \rho\frac{\partial V_s}{\partial y}\right) = 0
\end{aligned}
\tag{6}
$$

From the x-momentum equation

$$\rho_s\left(\frac{\partial u}{\partial t}+U_s\frac{\partial u}{\partial x}+v\frac{\partial U_s}{\partial y}\right)+\frac{\gamma-1}{\gamma}\frac{\partial p}{\partial x}+\delta\left[\rho_s U_s\frac{\partial u}{\partial x_1}+\frac{\gamma-1}{\gamma}\frac{\partial p}{\partial x_1}+\rho_s\left(u\frac{\partial U_s}{\partial x}+V_s\frac{\partial u}{\partial y}\right)+\rho\left(U_s\frac{\partial U_s}{\partial x_1}+V_s\frac{\partial U_s}{\partial y}\right)\right]=\frac{1}{R}\frac{\partial}{\partial y}\left(\mu_s\frac{\partial u}{\partial y}\right)+\frac{1}{R}G_1+O\left(\frac{\delta}{R}\right)+O(\delta^2). \tag{7}$$

The y-momentum equation gives

$$\rho_s\left(\frac{\partial v}{\partial t}+U_s\frac{\partial v}{\partial x}\right)+\frac{\gamma-1}{\gamma}\frac{\partial p}{\partial y}+\delta\left[\rho_s U_s\frac{\partial v}{\partial x_1}+\rho_s\left(V_s\frac{\partial v}{\partial y}+v\frac{\partial V_s}{\partial y}\right)\right]=\frac{1}{R}G_2+O\left(\frac{\delta}{R}\right)+O(\delta^2). \tag{8}$$

From the energy equation

$$\rho_s\left(\frac{\partial T}{\partial t}+U_s\frac{\partial T}{\partial x}+v\frac{\partial T_s}{\partial y}\right)-\frac{\gamma-1}{\gamma}\left(\frac{\partial p}{\partial t}+U_s\frac{\partial p}{\partial x}\right)+\delta\left[\rho_s U_s\frac{\partial T}{\partial x_1}-\frac{\gamma-1}{\gamma}U_s\frac{\partial p}{\partial x_1}+\rho_s\left(u\frac{\partial T_s}{\partial x_1}+V_s\frac{\partial T}{\partial y}\right)+\rho\left(U_s\frac{\partial T_s}{\partial x_1}+V_s\frac{\partial T_s}{\partial y}\right)\right]=\frac{1}{R\cdot \mathrm{Pr}}\frac{\partial}{\partial y}\left(\mu_s\frac{\partial T}{\partial y}\right)+\frac{1}{R}G_3+O\left(\frac{\delta}{R}\right)+O(\delta^2). \tag{9}$$

In (9), the similarity parameter R is

$$R=\frac{\delta^* U_\infty^* \rho_\infty^*}{\mu_\infty^*}\delta^2\left(\frac{\gamma-1}{\gamma}\right)\frac{1}{\left[(\gamma-1)M^2\right]^n}. \tag{10}$$

The quantities G_1, G_2, and G_3 are viscous dissipation terms that can be neglected everywhere in the boundary layer. Viscous terms proportional to the highest y-derivative are included in (7) and (9), since they are dominant in viscous sublayers as will be shown below. Terms proportional to δ describe nonparallel effects associated with downstream boundary layer growth. The small parameter δ can be expressed as (see Bush [11])

$$\delta=\left[\frac{\gamma-1}{\gamma}\cdot\frac{\left[(\gamma-1)M^2\right]^n}{\mathrm{Re}}\right]^{1/4},\ \mathrm{Re}_\infty=\frac{U_\infty^*\rho_\infty^* L^*}{\mu_\infty^*}. \tag{11}$$

From (10) and (11)

$$R = \mathrm{Re}_{\infty} \cdot \delta^3 \frac{\gamma}{\gamma - 1} \frac{1}{\left[(\gamma - 1) M^2\right]^n}. \tag{12}$$

Substitution of (11) into (12) gives $\delta = 1/R$ and the result that the similarity parameter $R \to \infty$ for the strong interaction case.

For stability considerations, the disturbance characteristics are represented in the normal mode form

$$q(x, x_1, y, t) = [q_0(x_1, y) + \delta \cdot q_1(x_1, y) + \ldots] \exp\left[\frac{i}{\delta} \int \alpha(x_1) dx_1 - i\omega t\right] \tag{13}$$

Modes with phase speed $c = \omega/\alpha$ satisfying the condition $\mathrm{Re}(c) < 1$ will be considered. If $c \to 1$, the disturbance is concentrated in the transitional layer located near the boundary layer edge. This case has been studied in [6] - [8]. Substitution of (13) into (6) - (9) gives the following system of stability equations to the first order approximation with respect to δ

$$i(\alpha U_s - \omega)\rho_0 + \rho_s \frac{\partial v_0}{\partial y} + v_0 \frac{\partial \rho_s}{\partial y} = 0 \tag{14}$$

$$\rho_s \left[i(\alpha U_s - \omega) u_0 + v_0 \frac{\partial U_s}{\partial y} \right] + i\alpha \frac{\gamma - 1}{\gamma} p_0 = \frac{1}{R} \frac{\partial}{\partial y} \left(\mu_s \frac{\partial u_0}{\partial y} \right) \tag{15}$$

$$i\rho_s (\alpha U_s - \omega) v_0 + \frac{\gamma - 1}{\gamma} \frac{\partial p_0}{\partial y} = 0 \tag{16}$$

$$\rho_s \left[i(\alpha U_s - \omega) T_0 + v_0 \frac{\partial T_s}{\partial y} \right] - i \frac{\gamma - 1}{\gamma} (\alpha U_s - \omega) p_0 = \frac{1}{R \cdot \mathrm{Pr}} \frac{\partial}{\partial y} \left(\mu_s \frac{\partial T_0}{\partial y} \right). \tag{17}$$

Since the mean-flow pressure is constant across the boundary layer, it is convenient to normalize the pressure to P_s so that the equation of state can be expressed as

$$T_s \rho_s = 1. \tag{18}$$

Using the notations

$$f = u_0, \varphi = \frac{v_0}{\alpha}, \pi = \frac{p_0}{P_s}, \theta = T_0, \tag{19}$$

we get the following system of stability equations in the form convenient for numerical integration

$$\frac{\mu_1}{\alpha R} f'' = \frac{1}{T_1}\left[i(U_1 - c)f + U_1'\varphi\right] + i\frac{\gamma - 1}{\gamma}\pi \tag{20}$$

$$\varphi' + if = i(U_1 - c)\left(\frac{\theta}{T_1} - \pi\right) + \frac{T_1'}{T_1}\varphi \tag{21}$$

$$\pi' = -i\frac{\gamma}{\gamma - 1}\frac{\alpha^2}{T_1}(U_1 - c)\varphi \tag{22}$$

$$\frac{\eta\mu_1}{\Pr \cdot \alpha R}\theta'' = \frac{T_1'}{T_1}\varphi + (\gamma - 1)(\varphi' + if) + i(U_1 - c)\frac{\theta}{T_1}. \tag{23}$$

where prime denotes the y-derivative. This system is a hypersonic analog of the Dunn-Lin system for the supersonic boundary layer. Derivation of (20)-(23) is based on an asymptotic analysis similar to that conducted by Cheng [12], and Alekseev [13] for moderate speeds. The asymptotic structure of disturbances across the boundary layer is schematically shown in Fig. 2 for $0 < \mathrm{Re}(c) < 1$.

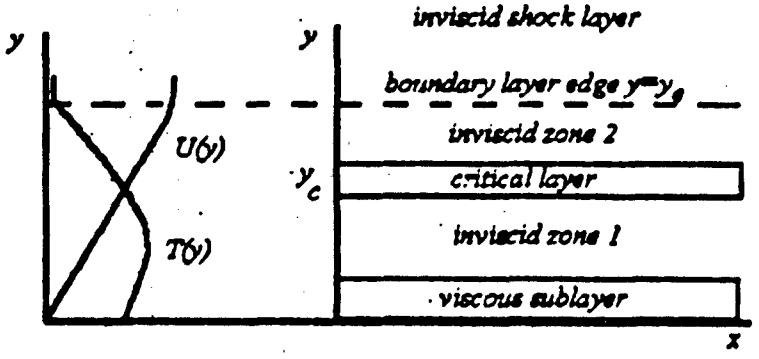

Fig. 2 Asymptotic structure of the disturbance field.

The following observations are relevant:

1. In Zones 1 and 2 with the thickness $O(1)$, viscous terms are negligible, and the system (20)-(23) is reduced to the inviscid stability equations.

2. In a viscous sublayer of thickness $\delta_1 = (\alpha R)^{-1/2}$, viscous terms from (20) and (23) are of the order of inviscid terms. Here, the solution is expanded in a power series of small parameter δ_1.

3. In the critical layer of thickness $\delta_2 = (\alpha R)^{-1/3}$, viscous terms are also of the order of inviscid terms. This layer is located near the critical point $y_c: U(y_c) = c$. Here, the solution is expanded in a power series of δ_2.

4. In the inviscid shock layer located outside the boundary layer, viscous terms are negligible and the system (14)-(17) is reduced to the inviscid stability equations.

Instead of solving stability equations in each sublayer and performing matching between asymptotic solutions, we can solve the system (20)-(23) numerically keeping the viscous terms with the highest y-derivative throughout the entire region of integration. This allows us to obtain a composite solution which is uniformly valid in all decks. A similar approach has been applied by Mack [2], Gaponov and Maslov [14], Tumin and Fedorov [15], and others to stability analysis of supersonic flows. Note that the system (20)-(23) can be directly derived from the Dunn-Lin system by applying the hypersonic limit and using the asymptotics (5).

Summarizing, we conclude that the disturbance structure and stability equations in the hypersonic boundary layer are qualitatively similar to those for supersonic flow. However, the behavior of the disturbance amplitude near the upper boundary layer edge and within the inviscid shock layer is essentially different from the moderate speed case. The mean flow temperature tends to zero at the upper boundary layer edge, which separates the hot flow in the boundary layer from the cool flow in the shock layer. As will be shown below, the large difference between temperatures of these flows strongly affects boundary conditions for the disturbance amplitude.

3.3 Disturbances in the inviscid shock layer

Consider the inviscid flow between the shock wave and the upper boundary layer edge (see Fig. 1). We specify nondimensional variables of inviscid flow as

$$(x_1, y_1) = (x^*, y^*) / L^*, t_1 = t^* / (L^* / U_\infty^*) \tag{24}$$

$$\hat{p} = \frac{p^* - p_\infty^*}{\rho_\infty^* U_\infty^{*2}}, \hat{T} = \frac{T^*}{T_\infty^*}, \hat{\rho} = \frac{\rho^*}{\rho_\infty^*}, (\hat{u}, \hat{v}) = \frac{(u^*, v^*)}{U_\infty^*}. \tag{25}$$

The shock-wave shape* is defined as

$$y_{1s} = \delta \cdot \hat{g}(x_1, t_1), \hat{g} = O(1) \tag{26}$$

* Subscript s is used interchangeably herein to denote shock quantity or (steady) mean flow. This distinction should be obviated by the useage context.

The inviscid flow in the shock layer is described by the system of equations

$$\frac{\partial \hat{\rho}}{\partial t_1}+\frac{\partial \hat{\rho}\hat{u}}{\partial x_1}+\frac{\partial \hat{\rho}\hat{v}}{\partial y_1}=0 \tag{27}$$

$$\hat{\rho}\left(\frac{\partial \hat{u}}{\partial t_1}+\hat{u}\frac{\partial \hat{u}}{\partial x_1}+\hat{v}\frac{\partial \hat{u}}{\partial y_1}\right)+\frac{\partial \hat{p}}{\partial x_1}=0 \tag{28}$$

$$\hat{\rho}\left(\frac{\partial \hat{v}}{\partial t_1}+\hat{u}\frac{\partial \hat{v}}{\partial x_1}+\hat{v}\frac{\partial \hat{v}}{\partial y_1}\right)+\frac{\partial \hat{p}}{\partial y_1}=0 \tag{29}$$

$$\hat{\rho}\left(\frac{\partial}{\partial t_1}+\hat{u}\frac{\partial}{\partial x_1}+\hat{v}\frac{\partial}{\partial y_1}\right)\hat{S}=0 \tag{30}$$

$$\hat{S}=\frac{\hat{p}}{\hat{\rho}^{\gamma}}, \tag{31}$$

where $\hat{S}$ is the entropy function.

The boundary conditions at the shock wave are

$$\hat{u}(x_1,y_{1s},t_1)=1-\frac{2}{\gamma+1}\delta^2(D_1\hat{g})^2 \tag{32}$$

$$\hat{v}(x_1,y_{1s},t_1)=\frac{2}{\gamma+1}\delta D_1\hat{g} \tag{33}$$

$$\hat{p}(x_1,y_{1s},t_1)=\frac{2}{\gamma+1}\delta^2(D_1\hat{g})^2 \tag{34}$$

$$\hat{\rho}(x_1,y_{1s},t_1)=\frac{\gamma+1}{\gamma-1} \tag{35}$$

$$D_1\equiv\frac{\partial}{\partial x_1}+\frac{\partial}{\partial t_1} \tag{36}$$

We assume that the shock wave has the shape

$$\hat{g}=g_0(x_1)+\varepsilon\cdot\delta\cdot g_1(x,t), \tag{37}$$

where $x=x_1/\delta$, and $t=t_1/\delta$ are fast variables of the disturbance flowfield. Using these, the boundary conditions (32)-(35) are written as

$$\hat{u}=1-\frac{2}{\gamma+1}\delta^2[g_{0x_1}{}^2+2\varepsilon g_{0x_1}Dg_1+\ldots] \tag{38}$$

$$\hat{v}=\frac{2}{\gamma+1}\delta[g_{0x_1}+\varepsilon Dg_1+\ldots] \tag{39}$$

$$\hat{p} = \frac{2}{\gamma+1}\delta^2[g_{0x_1}{}^2 + 2\varepsilon g_{0x_1} Dg_1 + \ldots] \tag{40}$$

$$\hat{\rho} = \frac{\gamma+1}{\gamma-1} \tag{41}$$

$$D = \frac{\partial}{\partial x} + \frac{\partial}{\partial t}$$

In addition, we introduce the shock layer variable $y = y_1/\delta$, and the fast variable $y_2 = y_1/\delta^2$. The boundary conditions (38) - (41) and the structure of (27)-(30) dictate the following scaling for the mean flow and disturbance characteristics

$$\hat{u} = 1 + \delta^2[u_s(x_1, y) + \varepsilon u_1(x_1, y, x, y_2, t)] + \cdots \tag{42}$$

$$\hat{v} = \delta[v_s(x_1, y) + \varepsilon v_1(x_1, y, x, y_2, t)] + \cdots \tag{43}$$

$$\hat{p} = \delta^2[p_s(x_1, y) + \varepsilon p_1(x_1, y, x, y_2, t)] + \cdots \tag{44}$$

$$\hat{\rho} = \rho_s(x_1, y) + \varepsilon\rho_1(x_1, y, x, y_2, t) + \cdots \tag{45}$$

Substituting (42)-(45) into (37)-(31) and linearizing gives the following system of equations for the disturbance flowfield

$$D\rho_1 + v_s(x_1, y)\frac{\partial \rho_1}{\partial y_2} + \rho_s(x_1, y)\frac{\partial v_1}{\partial y_2} = 0 \tag{46}$$

$$\rho_s(x_1, y)\left(Du_1 + v_s(x_1, y)\frac{\partial u_1}{\partial y_2}\right) + \frac{\partial p_1}{\partial x} = 0 \tag{47}$$

$$\rho_s(x_1, y)\left(Dv_1 + v_s(x_1, y)\frac{\partial v_1}{\partial y_2}\right) + \frac{\partial p_1}{\partial y_2} = 0 \tag{48}$$

$$DS_1 + v_s(x_1, y)\frac{\partial S_1}{\partial y_2} = 0 \tag{49}$$

$$S_1 = \frac{p_1}{p_s} - \gamma\frac{\rho_1}{\rho_s}. \tag{50}$$

In the first order approximation, the boundary conditions (38) - (41) at $y = g_0(x_1)$ are

$$u_1 = -\frac{4}{\gamma+1} g_{0x_1} Dg_1 \tag{51}$$

$$v_1 = \frac{2}{\gamma+1} Dg_1 \tag{52}$$

$$p_1 = 2g_{0x_1} v_1 \tag{53}$$

$$\rho_1 = 0. \tag{54}$$

These conditions have been shifted to the undisturbed shock using the following expansions for the steady flow profiles

$$F(y_s) = F_s(g_0) + \varepsilon\delta \frac{\partial F_s}{\partial y}(g_0) g_1 ,$$

where F signifies a flow dependent variable.

Since the coefficients appearing in (46)-(49) are functions of slow variables only, we can apply the WKB method. Accordingly, a solution is represented in the form

$$q_1 = [q_{10}(x_1, y) + \delta q_{11}(x_1, y) + \ldots] \cdot \exp\left(\frac{i}{\delta} \int \alpha dx_1 + \lambda dy - i\omega t \right)$$

In the first order approximation with respect to the small parameter δ, the system of equations for pressure and vertical velocity are

$$\frac{1}{\gamma}[i(\alpha - \omega) + i\lambda v_s] \frac{p_{10}}{p_s} + i\lambda v_{10} = 0 \tag{54}$$

$$\frac{1}{T_{ss}}[i(\alpha - \omega) + i\lambda v_s] v_{10} + i\lambda \frac{p_{10}}{p_s} = 0 \tag{55}$$

$$T_{ss} = \frac{p_s}{\rho_s}. \tag{56}$$

Equations (47), and (50) for the entropy function S_1 and longitudinal velocity u_1 can be found separately using solutions of (54) and (55). At some point (x_1, y), the system (54)-(56) has a non-trivial solution if the wave numbers satisfy the dispersion relation

$$\lambda^2 - \frac{1}{\gamma T_{ss}}[(\alpha - \omega) + \lambda v_s]^2 = 0, \tag{57}$$

which gives

$$\lambda_{1,2} = \mp \frac{\alpha - \omega}{\sqrt{\gamma T_{ss}} \pm v_s}.$$

Accordingly, the general solution is

$$p_{10} = p_s \left[C_1 \cdot \exp\left(\frac{i}{\delta} \int_{y_s}^{y} \lambda_1 dy \right) + C_2 \cdot \exp\left(\frac{i}{\delta} \int_{y_s}^{y} \lambda_2 dy \right) \right] \tag{58}$$

$$v_{10} = \left[C_1 \frac{\lambda_1 T_{ss}}{\alpha - \omega + \lambda_1 v_s} \exp\left(\frac{i}{\delta} \int_{y_s}^{y} \lambda_1 dy \right) + C_2 \frac{\lambda_2 T_{ss}}{\alpha - \omega + \lambda_2 v_s} \exp\left(\frac{i}{\delta} \int_{y_s}^{y} \lambda_2 dy \right) \right]$$

where y_e corresponds to the upper boundary layer edge. The constants C_1, and C_2 must be found from the boundary condition (53) and matching with the boundary layer solution.

3.4 Matching

In the inviscid zone 2 of the boundary layer (see Fig. 1), the system of equations (20)-(23) can be reduced to the inviscid equations for the pressure π, and the vertical velocity $v_0 = \alpha\varphi$

$$\varphi' - \frac{U_s'}{U_s - c}\varphi + i\frac{(U_s - c)^2 - (\gamma-1)T_s}{\gamma(U_s - c)}\pi = 0 \tag{59}$$

$$\pi' + i\alpha^2\frac{\gamma(U_s - c)}{(\gamma-1)T_s}\varphi = 0 \tag{60}$$

Near the upper boundary layer edge $U_s(y) \to 1$, and $T_s \to 0$, as $y \to y_e - 0$, the limiting form of (59), and (60) is

$$\varphi' + i\frac{1-c}{\gamma}\pi = 0 \tag{61}$$

$$\pi' + i\alpha^2\frac{\gamma(1-c)}{(\gamma-1)T_s}\varphi = 0 \tag{62}$$

The solution of (61), (62) is represented in the WKB form

$$\pi = A_1 \exp\left(-i\int_{y_e}^{y}\frac{\alpha-\omega}{\sqrt{(\gamma-1)T_s}}dy\right) + A_2\exp\left(i\int_{y_e}^{y}\frac{\alpha-\omega}{\sqrt{(\gamma-1)T_s}}dy\right) \tag{63}$$

$$\varphi = \frac{\sqrt{(\gamma-1)T_s}}{\gamma\alpha}\left[A_1\exp\left(-i\int_{y_e}^{y}\frac{\alpha-\omega}{\sqrt{(\gamma-1)T_s}}dy\right) - A_2\exp\left(i\int_{y_e}^{y}\frac{\alpha-\omega}{\sqrt{(\gamma-1)T_s}}dy\right)\right]$$

where A_1, A_2 are constants. Using the definition

$$\bar{T} \equiv \frac{T_s^*}{T_\infty^*} = (\gamma-1)M^2T_s, \tag{64}$$

we obtain the following explicit forms for the disturbance amplitude, as $y \to y_e - 0$

$$p_0 \to P_s\left[A_1 \exp\left(-i\int_{y_e}^{y}\frac{(\alpha-\omega)M}{\sqrt{\bar{T}}}dy\right)+A_2\exp\left(i\int_{y_e}^{y}\frac{(\alpha-\omega)M}{\sqrt{\bar{T}}}dy\right)\right] \qquad (65)$$

$$v_0 \to \frac{\sqrt{\bar{T}}}{\gamma M}\left[A_1 \exp\left(-i\int_{y_e}^{y}\frac{(\alpha-\omega)M}{\sqrt{\bar{T}}}dy\right)-A_2\exp\left(i\int_{y_e}^{y}\frac{(\alpha-\omega)M}{\sqrt{\bar{T}}}dy\right)\right]. \qquad (66)$$

Now we consider the shock layer solution (58) as $y \to y_e + 0$. Since the mean flow temperature T_{-s} tends to infinity, and the mean-flow vertical velocity $v_s = O(1)$, the asymptotic form of the solution (58) is

$$p_{10} \to p_s(y_e)\left[C_1 \cdot \exp\left(-\frac{i}{\delta}\int_{y_e}^{y}\frac{\alpha-\omega}{\sqrt{\gamma T_{ss}}}dy\right)+C_2\cdot\exp\left(\frac{i}{\delta}\int_{y_e}^{y}\frac{\alpha-\omega}{\sqrt{\gamma T_{ss}}}dy\right)\right] \qquad (67)$$

$$v_{10} \to \sqrt{\frac{T_{ss}}{\gamma}}\left[C_1 \cdot \exp\left(-\frac{i}{\delta}\int_{y_e}^{y}\frac{\alpha-\omega}{\sqrt{\gamma T_{ss}}}dy\right)-C_2\cdot\exp\left(\frac{i}{\delta}\int_{y_e}^{y}\frac{\alpha-\omega}{\sqrt{\gamma T_{ss}}}dy\right)\right]. \qquad (68)$$

Using the scaling (44), (45), and the definition (56), we obtain the relation

$$T_{ss} = \frac{\bar{T}}{\gamma M^2 \delta^2}.$$

Accordingly, the vertical velocity amplitude $\tilde{v}_1 \equiv \delta v_{10}$ and the pressure amplitude p_{10} are respectively

$$p_0 \to p_s(y_e)\left[A_1 \exp\left(-i\int_{y_e}^{y}\frac{(\alpha-\omega)M}{\sqrt{\bar{T}}}dy\right)+A_2\exp\left(i\int_{y_e}^{y}\frac{(\alpha-\omega)M}{\sqrt{\bar{T}}}dy\right)\right] \qquad (69)$$

$$\tilde{v}_1 \to \frac{\sqrt{\bar{T}}}{\gamma M}\left[A_1 \exp\left(-i\int_{y_e}^{y}\frac{(\alpha-\omega)M}{\sqrt{\bar{T}}}dy\right)-A_2\exp\left(i\int_{y_e}^{y}\frac{(\alpha-\omega)M}{\sqrt{\bar{T}}}dy\right)\right] \qquad (70)$$

Comparison of the outer asymptotic limit (65), (66) with the inner limit (69), (70) and accounting for the relation $p_s(y_e) = P_s$ shows that *the pressure and vertical velocity disturbances match at the upper boundary-layer edge, $y = y_e$.*

On comparison of the boundary-layer flow field representations (5) with the corresponding shock-layer flow field expressions (42)-(45) and if the disturbance characteristics are normalized in such a way that the pressure amplitude is $p = O(1)$ in the boundary layer, then:

1. $p = O(1)$ in the shock layer.
2. The temperature amplitude $T = O(1)$ in the boundary layer, and $T = O(\delta^2)$ in the shock layer.
3. The longitudinal velocity amplitude is $u = O(1)$ in the boundary layer, and $u = O(\delta^2)$ in the shock layer.
4. The vertical velocity amplitude is $v = O(1)$ in the boundary layer, and $v = O(\delta)$ in the shock layer.

This statement is schematically illustrated in Fig. 3.

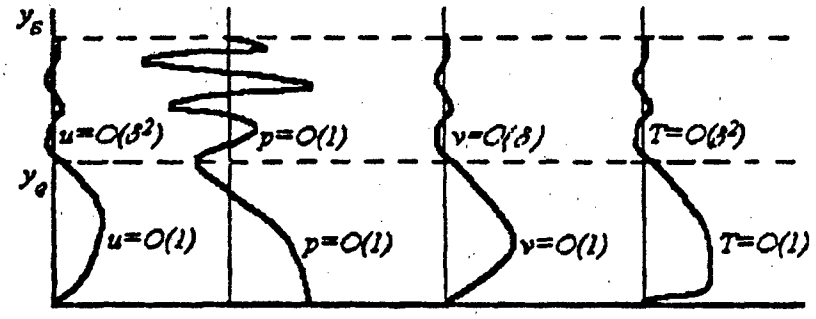

Fig. 3 Orders of magnitude for the amplitude of the velocity, pressure and temperature disturbance, (normalized with respect to ε).

Consequently, , the boundary conditions

$$\begin{aligned} u_0(y_\varepsilon) &\equiv f(y_\varepsilon) = 0 \\ v_0(y_\varepsilon) &\equiv \alpha\varphi(y_\varepsilon) = 0 \\ T_0(y_\varepsilon) &\equiv \theta(y_\varepsilon) = 0 \end{aligned} \tag{71}$$

hold to $O\delta$).

On the wall surface the no-slip conditions are

$$f(0) = \varphi(0) = \theta(0) = 0. \tag{72}$$

Equations (20)-(23) with the boundary conditions (71), and (72) consititute an eigenvalue problem. To $O\delta$), this problem does not depend on the shock-layer flow. According to (71) the upper boundary-layer edge separating the hot viscous flow from the cool shock-

layer flow behaves as a solid wall. In spite of the strong interaction between steady flows the disturbances with the phase speed less than unity only weakly interact with each other. However, the eigenvalue problem **implicitly rather than explicitly** depends on the type of interaction, because the stability equations include the steady flow profiles.

3.5 Weak Interaction case

For weak interaction, the inviscid flow parameters tend to their freestream values as $y \to \infty$. Then the representations of the pressure, density and temperature in the boundary layer are [16]

$$\begin{aligned}
\hat{p}(x,y,t) &= \frac{1}{\gamma M^2}\left[P_s(x_1) + \varepsilon \cdot p(x,x_1,y,t)\right] + \cdots \\
\hat{\rho}(x,y,t) &= \frac{1}{(\gamma-1)M^2}\left[\rho_s(x_1,y) + \varepsilon \cdot \rho(x,x_1,y,t)\right] + \cdots \\
\hat{T}(x,y,t) &= (\gamma-1)M^2\left[T_s(x_1,y) + \varepsilon \cdot T(x,x_1,y,t)\right] + \cdots
\end{aligned} \tag{73}$$

From an analysis similar to the strong interaction case, we find that the stability equations coincide with (20)-(23), if the similarity parameter is defined as

$$R = \frac{\delta^* U_\infty^* \rho_\infty^*}{\mu_\infty^*} \frac{1}{\left[(\gamma-1)M^2\right]^{\frac{n+1}{2}}}. \tag{74}$$

From the expression for the boundary layer displacement thickness [16]

$$\delta^* = \left[(\gamma-1)M^2\right]^{\frac{n+1}{2}} \frac{L^*}{\sqrt{\mathrm{Re}_\infty}}, \tag{75}$$

the explicit form of the small (interaction) parameter is

$$\delta = \frac{\left[(\gamma-1)M^2\right]^{\frac{n+1}{2}}}{\sqrt{\mathrm{Re}_\infty}} \tag{76}$$

From (74)-(76) we obtain the relation $\delta = 1/R$, which is similar to the strong interaction case. To $O(\delta)$, the boundary conditions for the disturbance at the upper boundary layer edge are given by (71). Similar to the strong interaction case, the upper boundary layer edge separates a cool free stream from a hot flow in the boundary layer, and behaves as a

solid wall reflecting the boundary layer disturbance. **The eigenvalue problem (20)-(23) with boundary conditions (71), (72) is valid for the weak interaction case, if we simply replace the mean flow profiles by new ones.** Consequently we can study the boundary-layer stability with respect to disturbances of phase speed $c<1$ for strong, weak, and moderate interaction regimes using the same algorithm.

3.6 Three-dimensional case

The foregoing analysis has been extended to the case of 3-D disturbances in a 3-D hypersonic boundary layer. Here, the disturbance is represented in the normal mode form

$$q(x,y,z,t)=q_0(x_1,y)\cdot\exp\left[\frac{i}{\delta}\int\alpha(x_1)dx_1+i\beta z-i\omega t\right], \tag{77}$$

where z is the lateral (spanwise) coordinate.

For this case, the 3-D system of stability equations is reduced to a 2-D system by the following transformation of the mean-flow and disturbance characteristics

$$k^2=\alpha^2+\beta^2,U_{\infty}=\frac{\alpha U_1+\beta W_1}{k},T_{\infty}=T_1 \tag{78}$$
$$f=\frac{1}{k}(\alpha u_0+\beta w_0),\varphi=\frac{v_0}{k},c=\frac{\omega}{k},$$

where W_1, and w_0 are the mean value and the disturbance amplitude of z-velocity component respectively.

Equations (20)-(23), and the boundary conditions (71), (72) take the form

$$\frac{\mu_{\infty}}{kR}f''=\frac{1}{T_{\infty}}\left[i(U_{\infty}-c)f+U'_{\infty}\varphi\right]+i\frac{\gamma-1}{\gamma}\pi \tag{79}$$

$$\varphi'+if=i(U_{\infty}-c)\left(\frac{\theta}{T_{\infty}}-\pi\right)+\frac{T'_{\infty}}{T_{\infty}}\varphi \tag{80}$$

$$\pi'=-i\frac{\gamma}{\gamma-1}\frac{k^2}{T_{\infty}}(U_{\infty}-c)\varphi \tag{81}$$

$$\frac{\gamma\mu_{\infty}}{\mathrm{Pr}\cdot kR}\theta''=\frac{T'_{\infty}}{T_{\infty}}\varphi+(\gamma-1)(\varphi'+if)+i(U_{\infty}-c)\frac{\theta}{T_{\infty}} \tag{82}$$

$$f(0)=\varphi(0)=\theta(0)=0 \tag{83}$$

$$f(y_e) = \varphi(y_e) = \theta(y_e) = 0 \tag{84}$$

Note that this system may be used to study cross flow instability at hypersonic speeds. In contrast to the full Navier-Stokes stability equations, the system (79)-(82) does not contain second derivatives of the mean-flow profiles. This saves computational time in otherwise time-consuming and intense calculations of the basic flow distributions.

3.7 Interactive steady flow

Strong interaction mean flow profiles for U_s and T_s can be obtained using a self-similar solution of the boundary layer equations (see for example [11], and [17]). We consider the boundary layer on a flat plate with constant surface temperature. For brevity we assume that the exponent of the viscosity-temperature law is $n = 1$. On introduction of the similarity variables

$$\eta = \frac{P_s}{\left(2\int_0^{x_1} P_s dx_1\right)^{1/2}} \int_0^y \frac{dy}{T_s} \tag{85}$$

$$U_s(\eta) = F'(\eta), H_s(\eta) = \frac{1}{2} G(\eta) \tag{86}$$

$$T_s(\eta) = \frac{1}{2}\left(G - F'^2\right), \tag{87}$$

the boundary layer equations become

$$F''' + FF'' + \frac{\gamma - 1}{\gamma}(G - F'^2) = 0 \tag{88}$$

$$\left(\frac{1}{\mathrm{Pr}} G'\right)' + FG' + 2\left(\frac{\mathrm{Pr} - 1}{\mathrm{Pr}} F'F''\right)' = 0 \tag{89}$$

$$F(0) = F'(0) = 0, \; G(0) = G_w \tag{90}$$

$$F'(\infty) = 1, G(\infty) = 1. \tag{91}$$

For strong interaction, the pressure is

$$P_s(x_1) = B_0 x_1^{-1/3}, \tag{92}$$

where the constant B_0 is obtained from the interaction law. With the Tangent-Wedge approximation*, this constant is [17]

$$B_0 = \frac{3}{2}\Delta\sqrt{\frac{(\gamma-1)\cdot(\gamma+1)}{2\gamma}}, \Delta = T_s^{-1/2}(0)\int_0^\infty T_s(\eta)d\eta. \tag{93}$$

The system of equations (88)-(91) was integrated using a fourth order-accurate Runge-Kutta method. Distributions of the velocity $U_s(\eta)$, and temperature $T_s(\eta)$ are shown in Fig. 4. The calculations were performed for an adiabatic wall; the specific heat ratio is $\gamma = 1.4$, and the Prandtl number is $\Pr = 0.72$. Integrating the temperature profile, we obtain from Eq. (93) that $\Delta = 1.463$.

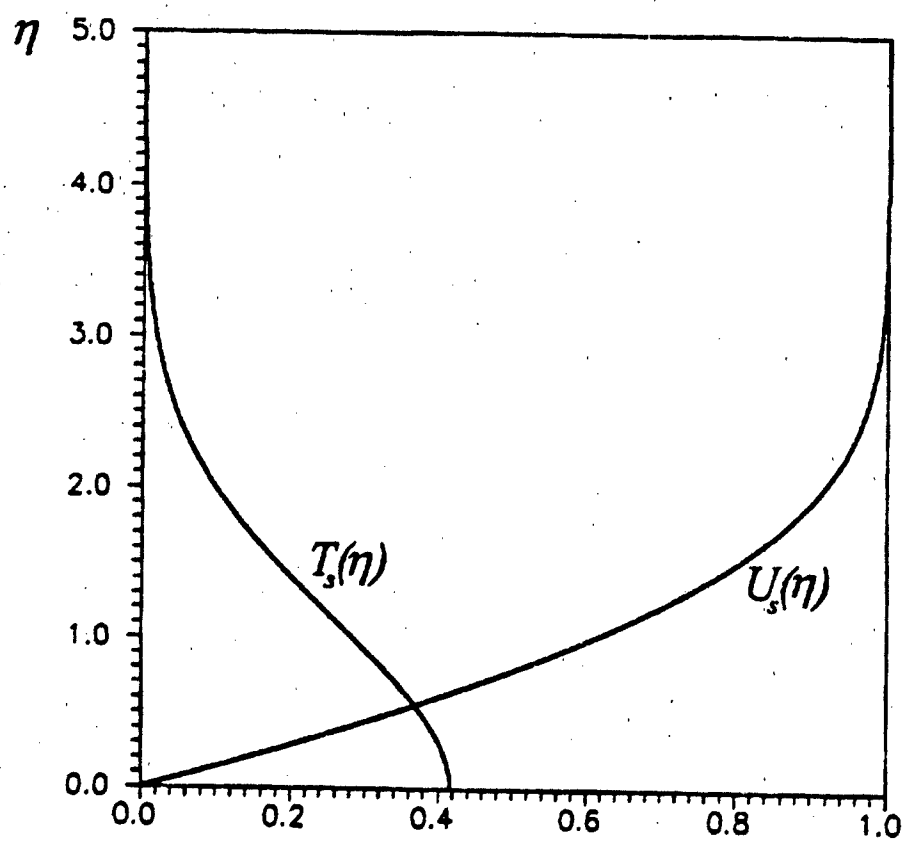

Fig. 4 Self-similar profiles for velocity, $U_s(\eta)$ and temperature, $T_s(\eta)$ in a hypersonic boundary layer on an adiabatic flat plate; $\gamma = 1.4$, $\Pr = 0.72$, $n = 1$.

* More asymptotically consistent values for this constant can be obtained form Hypersonic Small Disturbance Theory. Numerical solutions can give other estimates. However, neither will change the essential stability behaviors discussed here.

3.8 Stability computations and results

To obtain the results to be discussed, the eigenvalue problem (79)-(84) was solved numerically using the strong interaction mean flow profiles (86), (87). The system of stability equations is transformed into the form convenient for integration

$$\frac{d\vec{Z}}{d\eta} = A(\bar{k},\bar{\omega},U_s,T_s,\bar{R})\vec{Z} \qquad (93)$$
$$Z_1(0) = Z_3(0) = Z_5(0) = 0$$
$$Z_1(\infty) = Z_3(\infty) = Z_5(\infty) = 0$$

where $\vec{Z}(\eta) = (f, f', \varphi, \pi, \theta, \theta')^T$ is the eigenvector. According to the definition (85) of η, the similarity parameter, frequency and wavenumber are rescaled as

$$\bar{R} = \Gamma R, \bar{\omega} = \Gamma\omega, \bar{k} = \Gamma k \qquad (94)$$

$$\Gamma = \frac{1}{P_s}\left(2\int_0^{x_1} P_s dx_1\right)^{1/2} = 2B_0^{-1/2}x_1^{3/4}. \qquad (95)$$

Fourth order-accurate Runge-Kutta integration of the boundary problem (93) was performed using an the orthogonalization technique. For the spatial stability problem, the eigenvalue $\bar{k}(\bar{\omega})$ is searched at fixed real frequency $\bar{\omega}$ by the Newton iteration method. Unstable regime corresponds to $\mathrm{Im}(\bar{k}) < 0$.

Calculations were performed for 2-D eigenmodes with $\beta = 0$ and the phase speed $\mathrm{Re}(c) < 1$. The mean flow corresponds to the adiabatic case for specific heat ratio $\gamma = 1.4$, and Prandtl number $\mathrm{Pr} = 0.72$ (see Section 3.7). The exponent of the temperature-viscosity law is $n = 1$.

In Fig. 5, distributions of $\mathrm{Re}(\bar{k})$ are shown as a function of the frequency $\bar{\omega}$ for Reynolds number $\bar{R} = 2795$. It is seen that spectrum contains two families of normal modes denumerated as 1,2,..., and 1',2',.... At the intersection points, $\mathrm{Re}(\bar{k}_m) = \mathrm{Re}(\bar{k}_{m'})$, the phase speeds of two modes coincide implying their synchronization. This pattern is qualititatively similar to those obtained by Fedorov and Gushchin [4], [5] from the inviscid stability analysis of the short-scale disturbances in a shock layer. According to this model, the family 1, 2, ... in Fig. 5 corresponds to the upper waveguide located between the boundary layer edge and the second turning point $y_{t2}: U_s(y_{t2}) = \mathrm{Re}(c) + a(y_{t2})$, where $a(y) = \sqrt{(\gamma-1)T_s(y)}$ is the normalized local sonic speed. The family 1',2',...corresponds to the lower waveguide located between the wall and the first turning point $y_{t1}: U_s(y_{t1}) = \mathrm{Re}(c) - a(y_{t1})$. The disturbance pattern is

schematically shown in Fig. 6 for the short-wave limit. Large number modes behave as acoustic waves with small damping due to viscous dissipation.

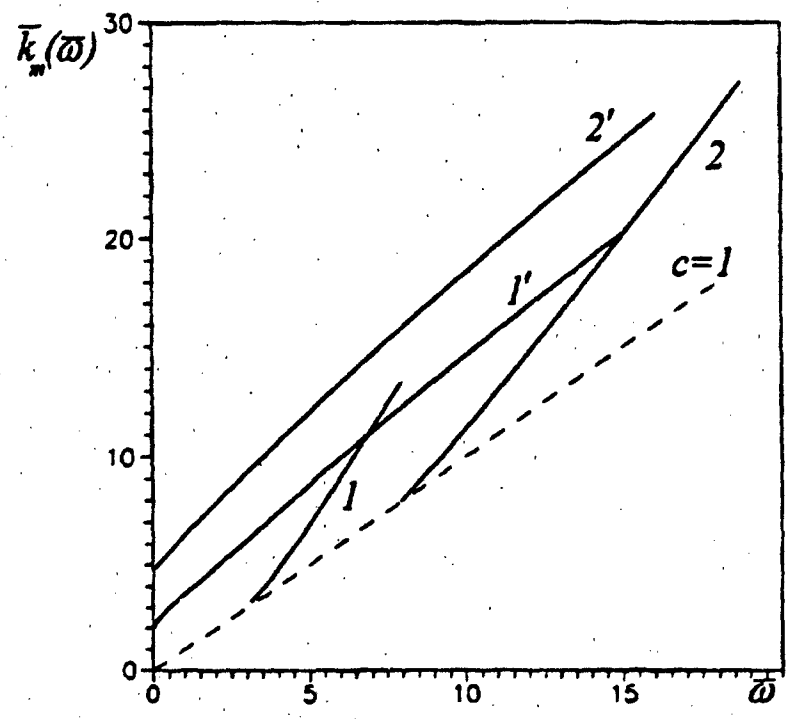

Fig. 5 Distributions $\mathrm{Re}\,\bar{k}_m(\bar{\omega})$ for the lower waveguide modes $m = 1', 2', \ldots$, and for the upper waveguide modes $m = 1,2,\ldots$; $\bar{R} = 2795$.

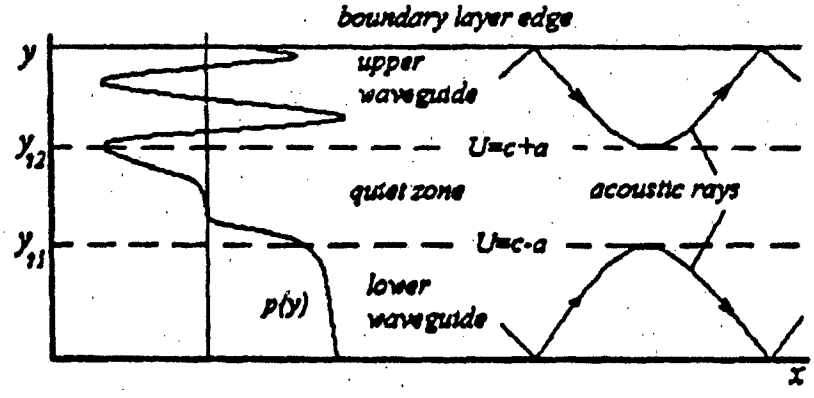

Fig. 6 Schematic pattern of disturbance flowfield in the boundary layer.

Near synchronism points however, the upper waveguide wave interacts with the corresponding lower-waveguide wave through the quiet zone depicted in Fig. 6. In

accordance with asymptotic model [4], [5], this interaction causes a splitting of the dispersion curves $\bar{k}(\bar{\omega})$ that can lead to instability.

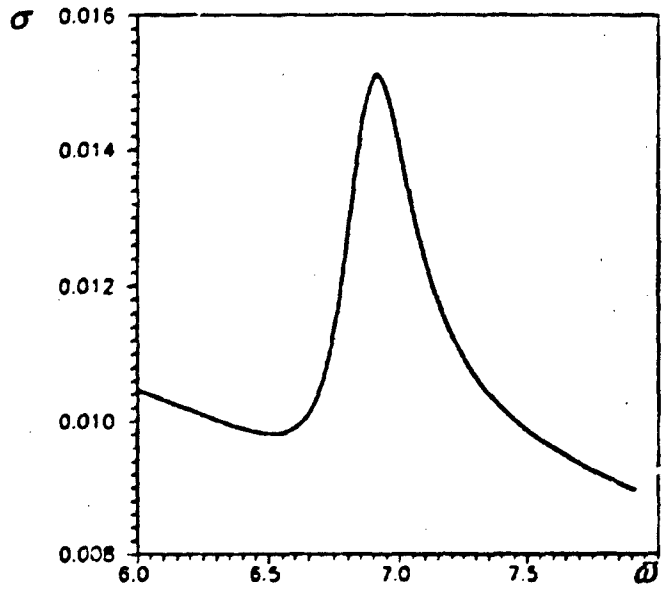

Fig. 7 The growth rate $\sigma = -\mathrm{Im}\,\bar{k}_1(\bar{\omega})$ for the mode 1 in the vicinity of the synchronism point $1-1'$; $\bar{R} = 2795$.

As an example, Fig. 7 shows a spike of the growth rate $\sigma = -\mathrm{Im}\,\bar{k}_1(\bar{\omega})$ near the synchronism point $1-1'$. For this case, the eigenfunction of the unstable mode 1 is shown in Figures 8a-8c. It is seen that the pressure waves are excited in both waveguides and interact with each other through the quiet zone.

The temperature distribution clearly indicates the presence of critical and viscous sublayers (see Fig. 8c). In accordance with qualitative pattern of disturbance structure shown in Fig. 2, viscous sublayers are separated by a relatively thick inviscid zone. In the critical layer, viscous effects cause strong temperature perturbations and very high gradients. The velocity and temperature amplitudes quickly vanish as $\eta \to \infty$, whereas the pressure disturbance is of the order of $O(1)$ at the upper boundary layer edge. This feature looks more graphic and realistic if the physical coordinate y is used instead of the coordinate η which is highly stretched near the boundary layer edge.

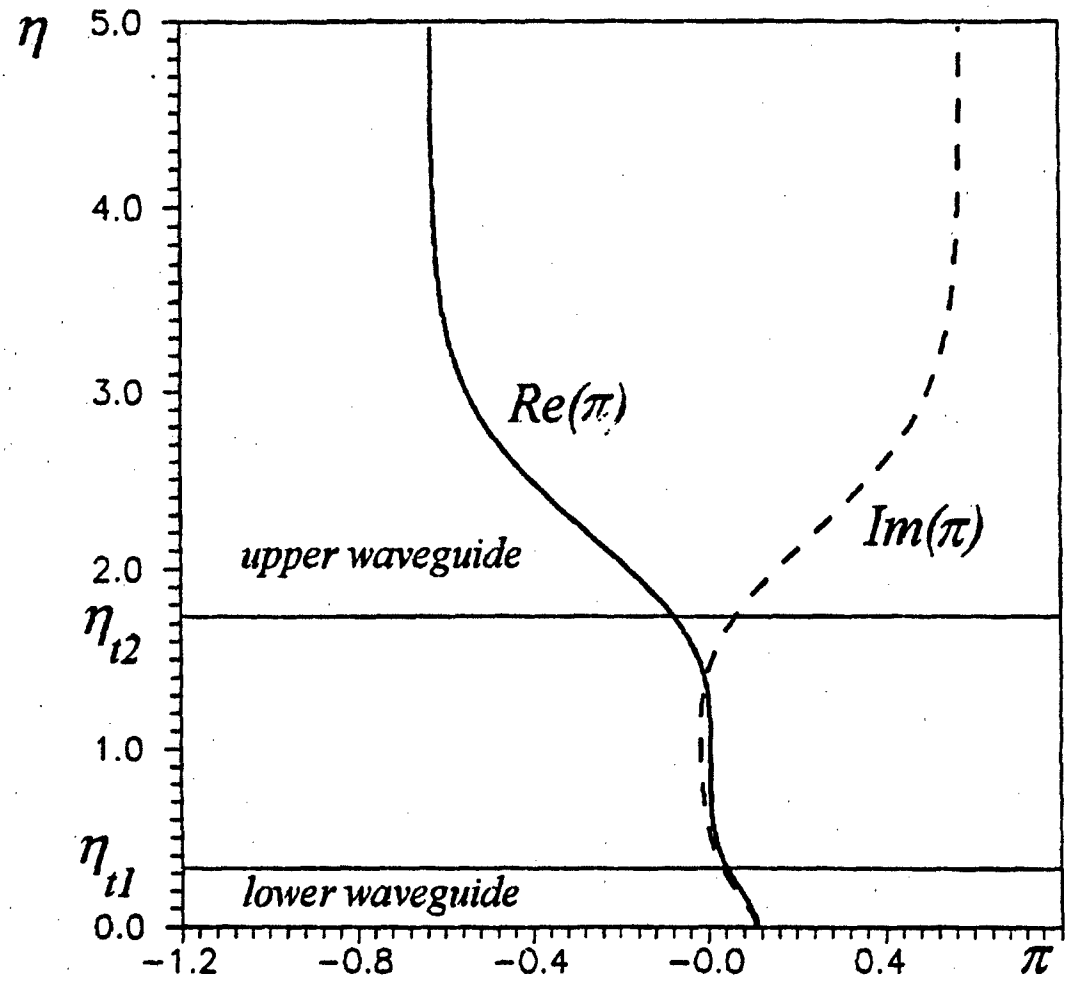

Fig. 8a Pressure amplitude $\pi(\eta)$ of Mode 1 at the synchronism point 1−1′; $\bar{R} = 2795, \bar{\omega} = 6.91, \bar{k} = 11.03 - i \cdot 0.015$.

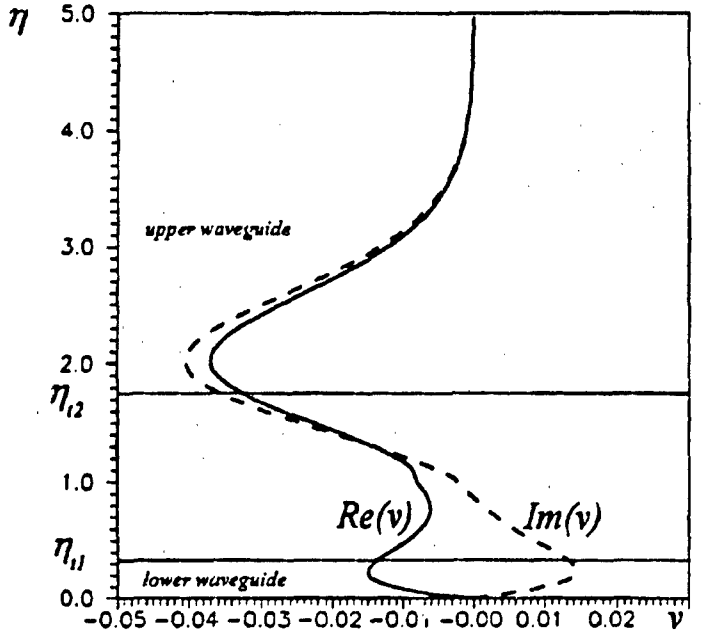

Fig. 8b Continued; the vertical velocity $v(\eta)$.

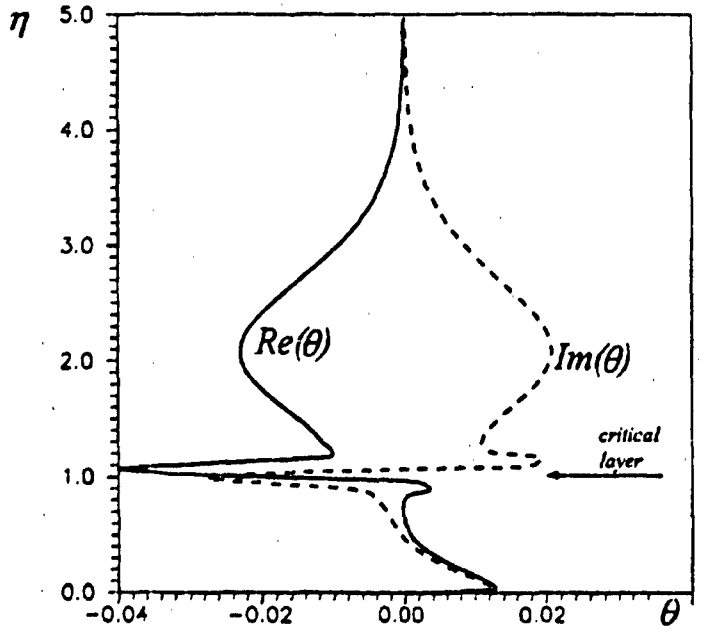

Fig. 8c Continued; the temperature $\theta(\eta)$.

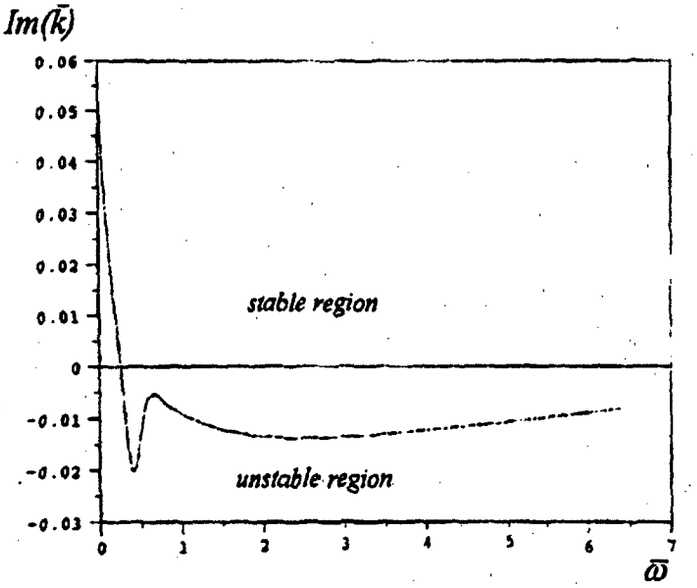

Fig. 9 The Mode-1 increment $\mathrm{Im}\,\bar{k}_1(\bar{\omega})$ as a function of frequency; $\bar{R} = 2795$.

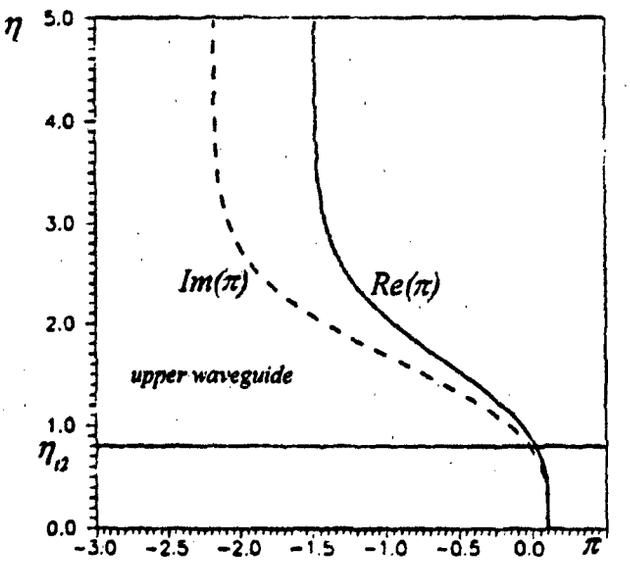

Fig. 10a Eigenfunction of Mode 1 at the frequency $\bar{\omega} = 0.39$, $\bar{R} = 2795$, $\bar{k} = 2.813 - i \cdot 0.02$; the pressure $\pi(\eta)$.

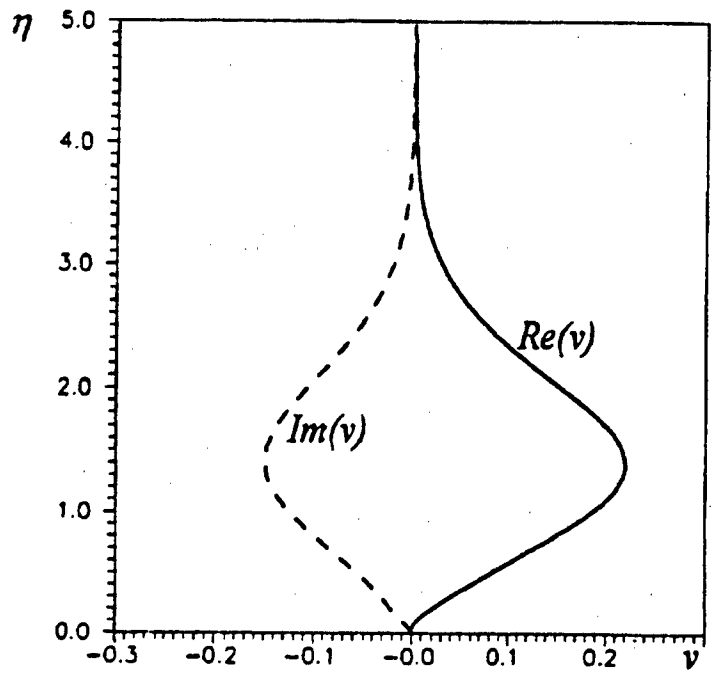

Fig. 10b Continued; the vertical velocity $v(\eta)$.

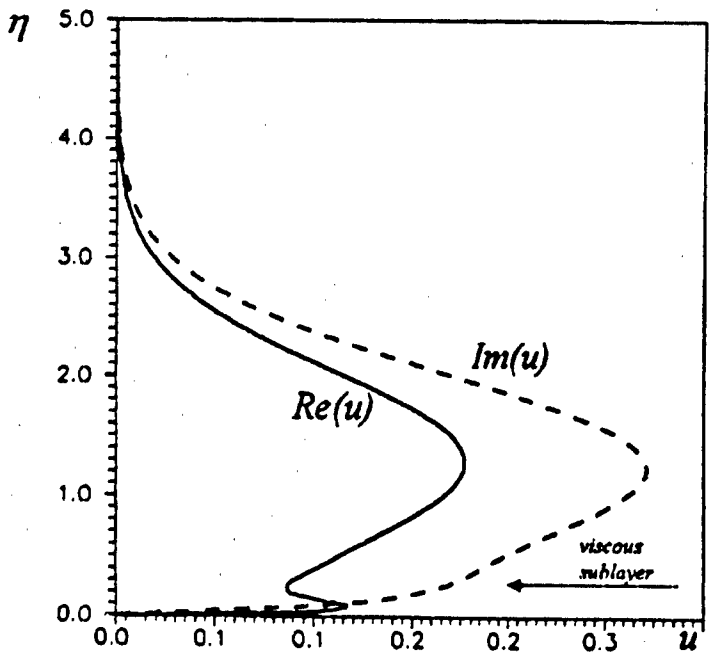

Fig. 10c Continued; the longitudinal velocity $u(\eta)$.

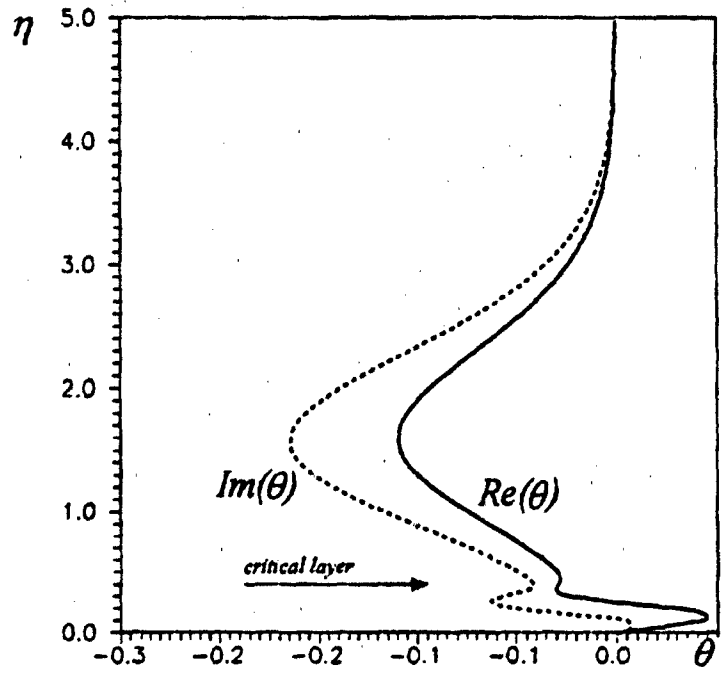

Fig. 10d Continued; the temperature $\theta(\eta)$.

For the modes depicted in Fig. 5, the most unstable is Mode 1. Its increment $\mathrm{Im}\,\bar{k}_1(\bar{\omega})$ is shown in Fig. 9 for the Reynolds number $\bar{R} = 2795$. It is seen that the growth rate achieves its maximum at the frequency $\bar{\omega} = 0.39$. The corresponding eigenfunctions are given in Figures 10a - 10d. For this case, the pressure amplitude is relatively large in the upper waveguide. The lower waveguide does not exist because its upper boundary is $y_{l1} < 0$. Since the phase speed is small, the critical layer is merged with the wall sublayer and blends to one deck as clearly seen in Figures 10c, and 10d. We believe that the Mode-1 instability is due to reflection of the pressure disturbance by the upper boundary layer edge. For this reason, we refer to this mode as a "reflectional instability." Distributions of its wavenumber $\mathrm{Re}\,\bar{k}_1(\bar{R})$ and growth rate $\sigma(\bar{R}) = -\mathrm{Im}\,\bar{k}_1(\bar{R})$ at the frequency $\bar{\omega} = 0.39$ are shown in Figures 11a and 11b respectively. The reflectional instability has a relatively small phase speed $\mathrm{Re}(c) \approx 0.14$, which is typical for acoustic modes. For reference we recall that the vorticity mode located in the transitional layer has the phase speed $\mathrm{Re}(c) \to 1$ [6]. From data shown in Figures 9, and 11b we conclude that the reflectional instability has a relatively high growth rate, of the order of $2 \cdot 10^{-2}$. Such a strong instability may achieve the critical amplification necessary for transition.

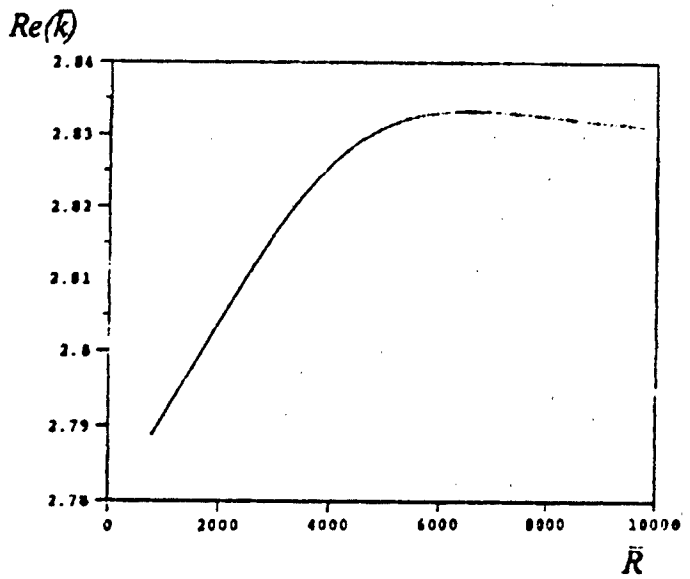

Fig. 11a Reflectional instability wavenumber $\mathrm{Re}\,\bar{k}_i(\bar{R})$ at frequency $\bar{\omega} = 0.39$.

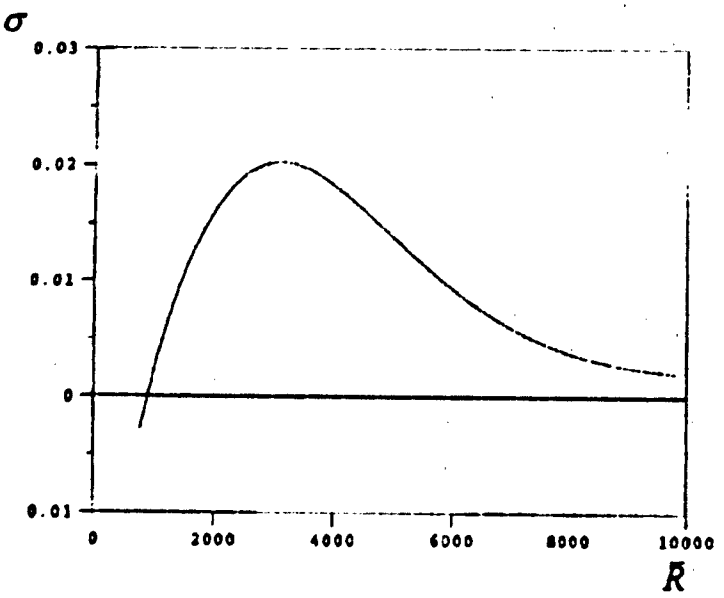

Fig. 11b Reflectional instability growth rate $\sigma(\bar{R}) = -\mathrm{Im}\,\bar{k}_i(\bar{R})$ at frequency $\bar{\omega} = 0.39$.

Since the eigenvalue problem (79) - (84) is isolated from the outer shock layer, we can assume that similar mechanism of the reflectional instability exists in hypersonic boundary layers at the moderate and weak interaction. Analysis of these cases is in progress.

3.9 Discussion

We have investigated the instability of the flat-plate hypersonic boundary layer to the normal modes with wavelength of the order of boundary layer thickness and phase speed less than 1. These modes are associated with acoustic waveguides located in the boundary layer. Asymptotic analysis showed that in the first order approximation with respect to the small parameter δ, the upper boundary layer edge behaves as a solid wall which reflects the boundary-layer disturbance. In spite of strong interaction between the steady shock and boundary layer mean flows, the unsteady disturbances under consideration only weakly interact with each other. From asymptotic analysis for the weak interaction case we have found that the eigenvalue problem has the same form for both weak and strong interaction. This allows us to study the boundary layer stability for the strong, moderate and weak interaction regimes using a single approach. The eigenvalue problem is easily extended to the 3-D case and can be used for analysis of the cross flow instability in three dimensional hypersonic boundary layers.

From our eigenvalue problem solution for the strong interaction case, we conclude that the reflection of disturbance by the upper boundary layer edge leads to instability of the upper-waveguide modes. We refer to this mechanism as the reflectional instability. Similar waveguide mechanisms have been ascribed to the dramatic effect of thinning the shock layer for $\gamma \to 1$ in [9]. There, thinning produces downstream amplification of otherwise long wavelength fluctuations that decay downstream for thicker shock layers.

Calculations have shown that the reflectional-instability mode has a relatively small phase speed $c \approx 0.14$. This is consistent with recent experiments of Maslov and his group. performed on a flat plate in hypersonic wind tunnel at Mach 20 (private communication). They observed slow waves propagating in the strong and moderate interaction region with a phase speed of the order of 0.2, and growing downstream. Since the reflectional-instability mode has a large growth rate, it can compete with other unstable modes such as the vorticity mode. We expect that downstream amplification of this mode can lead to early transition on hypersonic vehicle surfaces. These findings motivate us to study the reflectional instability mechanism further.

We also found that the upper waveguide modes can synchronize with the lower waveguide modes. Near synchronism points, additional growth rate spikes have been found. This instability mechanism is similar to those obtained from qualitative analysis of a simplified flow in a shock layer [4], [5]. In the vicinity of synchronism points the normal mode decomposition is not valid due to the singular nature of the dispersion relation. This situation has been studied by Fedorov and Khokhlov [3] for the case of

moderate Mach numbers. Using their results, we assume that the nonparallel effects* may cause strong exchange between modes near synchronism point.

3.10 References

1. Malik, M.R., Zang, T.A., and Bushnell, D.M., "Boundary Layer Transition in Hypersonic Flows," AIAA Paper No. 90-5232, 1990.

2. Mack, L.M., "Boundary-Layer Stability Theory," *Special Course on Stability and Transition of Laminar Flow*, edited by R. Michel, AGARD Rep. No. 709, pp. 3-1 to 3-81, 1984.

3. Fedorov, A.V., and Khokhlov, A.P., "Excitation and Evolution of Unstable Disturbances in Supersonic Boundary Layer," Proc. of 1993 ASME Fluid Engineering Conf., Washington, DC, June 20 - 24, 1993, *Transitional and Turbulent Compressible Flows*, FED-Vol. 151, pp. 1 - 13, 1993.

4. Gushchin, V.R., and Fedorov, A.V., "Short-Wave Instability in a Perfect-Gas Shock Layer," *Izvestiya Akad. Nauk SSSR, Mekhanika Zhidkosti i gaza*, No. 1, pp. 10 - 14, 1987 (in Russian).

5. Gushchin, V.R., and Fedorov, A.V. "Qualitative features of boundary-layer instability at high speeds of stream," *Mod. Mekh. Neod. Sistem*, ITPM SO AN SSSR, Novosibirsk, 93-116, 1989 (in Russian, English translation in NASA TT 20683, April 1990).

6. Blackaby, N., Cowley, S.J. and Hall, P., "On the Stability of Hypersonic Flow past a Flat Plate," *J. Fluid Mech.*, Vol. 247, pp. 369-416, 1993.

7. Grubin, S.E., and Trigub, V.N., "Asymptotic Stability Theory of a Hypersonic Boundary Layer," *Preprint TsAGI*, No. 38, 1991 (In Russian).

8. Smith, F.T., and Brown, S.N., "The Linear Inviscid Instability of a Blasius Boundary Layer at Large Values of the Mach Number," *J. Fluid Mech.*, Vol. 219, pp. 499-518, 1990.

9. Malmuth, N.D., "Stability of the Inviscid Shock layer in Strong Interaction Flow over a Hypersonic Flat Plate," *In Instabilities and Turbulence in Engineering Flows*, eds. D.E. Ashpis, T.B. Gatski and R. Hirsh. Kluwer Academic Publishers, 1993.

* These have not been emphasized in the hypersonic literature. The significance of these in a different hypersonic context was discussed in [9].

10. Reshotko, E., and Khan, M.M.S., "Stability of the Laminar Boundary Layer on a Blunted Plate in Supersonic Flow," In Eppler and Fasel eds., *Laminar-Turbulent Transition*, Springer -Verlag, 1980.

11. Bush, W.B., "Hypersonic Strong-Interaction Similarity Solutions for Flow past a Flat Plate," *J. Fluid Mech.*, Vol. 25, 51-64, 1966.

12. Cheng, S.-I., On the Stability of Laminar Boundary Layer Flow," Quart. Appl. Math., Vol. 11, No. 3, pp. 346 - 350, 1953.

13. Alekseev, M.A., "On Asymptotic Approximations of the Laminar Boundary Layer Stability at Supersonic Speeds," *Trudy TsAGI*, Vyp. 1420, 1972 (in Russian).

14. Gaponov, S.A., and Maslov, A.A., *Development of Disturbances in Compressible Flows*, Novosibirsk, Nauka, 1980 (in Russian).

15. Tumin, A.M., and Fedorov, A.V., "On the Weakly Nonparallel Effect on Stability Characteristics," Uchen. Zapiski TsAGI, Vol. 13, No. 6, pp. 91 - 96, 1982 (in Russian).

16. Hayes, W.D., and Probstein, R.F., *Hypersonic Flow Theory*, Academic Press, New York, 1959.

17. Neiland, V.Ya., "Propagation of Perturbations Upstream with Interaction between a Hypersonic Flow and a Boundary Layer," *Izv. Akad. Nauk. SSSR, Mekh. Zhid. i Gaza*, No. 4, pp. 40-49, 1970 (in Russian).

4. Low-frequency instability of hypersonic interactive boundary layers on a cooled surface

4.1 Introduction

This chapter reviews research supported by the contract and other funding concerning propagation of unsteady three-dimensional perturbations in hypersonic interactive boundary layers on a cooled surface. Such high speed boundary layers that are subject to the combined effect of the interaction with a shock layer and cooling of the surface are typical of realistic flight conditions and lead to substantial heat transfer and drag. The geometry of a flat plate is considered herein. For this simple shape, the stability of even the steady flow is complicated by a multiplicity of different mechanisms not exhibited at moderate supersonic Mach numbers. Two classical limits naturally evolve at high Mach numbers in this flow. Near the leading edge, a strong interaction regime occurs in which the shock wave is not far from the surface and the viscous boundary layer and inviscid shock layer are strongly coupled. Further downstream, the effect of the shock wave disappears and the boundary layer develops under zero pressure gradient (weak interaction). Strong and weak interactions have been studied extensively (see for example, [1-3]. Transition to turbulence has been observed in the last region only. However, as the Mach number increases, the strong interaction region expands rapidly. This could significantly influence the early stages of transition, since it will affect important receptivity and linear amplification processes.

In the limit of infinitely large Mach number, the temperature distribution has increasing nonuniformity and cannot be described in closed form independent of the Mach number. Additional distinctions are made in[4]. These include the observations that the domain of importance is not semi-infinite as in lower speed regimes, the shock is strong and curved and non parallelism can be more important and typical. Accordingly, the Orr-Sommerfeld approach cannot be applied *a priori*, and a suitable hypersonic limit involving the Mach and Reynolds numbers needs to be applied. Different types of instabilities can be studied using appropriate scalings relevant to the characteristic wave lengths present.

An interesting type of instability is inviscid which is due to a generalized inflection point within a thin transitional layer near the boundary layer upper edge. It was analyzed for the moderate interaction regime in [5] where the transitional layer between the external flow and a shear layer was considered and in [6] for a gas with a Chapman viscosity law and a unit Prandtl number. The main conclusion of these studies is that there is a numerous set of relatively weakly unstable acoustic modes and a most unstable vorticity mode. The acoustic modes were also analyzed in [7] and [8]. The phase speed of all the modes is close to the external flow velocity so that the relative growth is small. The results are in good qualitative and quantitative agreement with the computations for finite Mach numbers in [9]. The more general case of arbitrary Prandtl number and power law viscosity was considered in [10] where the effect of the viscosity on the stability

characteristics was included. Continuation into the strong interaction zone was treated in[11] assuming the Sutherland formula for the viscosity and Prandtl number equal to unity. Weak and strong interaction regimes were considered and it was concluded that although the scaling is quite different, the qualitative features of the vorticity mode instability are the same. The interaction leads to differences in the unperturbed flow profile only and does not change the physical mechanism of the instability. No influence of the shock wave arises because the perturbations are mostly concentrated in the transitional region between the shock and boundary layers. However, as shown in [8] for the non-interactive boundary layer on a wedge such influence may occur in some situations when there is a proper correlation between the wavelength scale and the thickness of the shock layer. Another example of amplification of the small time-harmonic perturbations in the curved shock layer was obtained in [4] by analysis of the initial boundary-value problem in the downstream direction.

Other types of unstable waves are small phase speed viscous modes described within the framework of triple-deck theory in [12] which showed that in supersonic flows, unstable modes of this type are essentially three-dimensional, where the direction of propagation lies outside the Mach cone. They dominate at moderate Mach numbers, but have negligibly small growth rate at hypersonic speeds and inviscid instability prevails. The last conclusion is correct if the temperature of the wall is of the order of the stagnation temperature. The effect of surface cooling at moderate Mach numbers was estimated in [13] in which it was found that it increases the growth rates and compresses the scales of the eigenmodes. For sufficiently strong cooling, the wavelength becomes comparable with the boundary layer thickness and a new *moderate cooling regime* occurs. Surface cooling is typical for hypersonic flight conditions. Its influence on the viscous modes may be significant. Special study of the strong interaction case is particularly warranted.

Analysis of the viscous eigensolutions in the strong interaction boundary layer was initiated in [14] for the steady two-dimensional case. It showed that their streamwise evolution is controlled by a power rather than exponential law in the weak interaction case. According to [15], the exponent in this power law grows to infinity as the specific heat ratio tends to unity. Therein, an analytic formula for the exponent was obtained and it was shown that the disturbance field is governed by the interaction between the viscous region and the main part of the boundary layer, while the upper region plays a passive role. A relationship between this mode and the Lighthill mode in the weak interaction region was postulated. This conjecture was subsequently verified by Brown *et al.* (1975). Another important result is that the exponent exhibits a sharp growth when the surface of the plate is cooled. A similar conclusion was obtained in [17].

This effort focused on three-dimensional unsteady disturbances. From the foregoing, it can be assumed that cooling of the surface will lead to appearance of short wavelength eigensolutions in the unsteady three-dimensional as well as the steady two-dimensional case. Moreover, these perturbations can be effectively confined within the boundary layer. Because the local Mach number within the boundary layer is of the order of unity, a three-dimensional instability similar to that considered in [12] for the moderate Mach numbers

may be anticipated. In Section 2, the proper scaling for the perturbations field is developed. The asymptotic expansions, analysis of the each region and matching leading to the complete formulation, which is a type of the triple-deck problem with a new interaction law, are discussed in Section 3. As a simple framework to exhibit some of the high Mach number physics and relate to the earlier two-dimensional steady effort, the linearized forced transient problem of a harmonically oscillating hump starting its motion at some instant of time is considered in Section 4.

In Section 4, the dispersion relation is analyzed and all eigenmodes with respect to upstream and downstream propagation are classified. In particular, the mode of Neiland - Brown and Stewartson is shown to propagate upstream. As a confirmation of expectations, another three-dimensional mode appears that is unstable in the downstream direction. Its growth rate is not bounded in the short wave limit so that the forced problem is well-posed on the set of functions with compact support in wavenumber space. A limiting process to a wider class of functions demonstrates that the part of the solution containing the fast growing modes is convected downstream. Hence, in the large-time limit the perturbation field consists of the time-harmonic component without an infinitely growing mode. The far-field asymptotic of this component is estimated and the direction of the maximal amplification versus frequency is determined.

Other possible mechanisms of instability and correspondence with experimental observations in [18] and [19] are discussed in Section 5.

4.2 Formulation

We consider three-dimensional short-scale unsteady perturbations in a hypersonic flow past a semi-infinite flat plate developing at a distance L from the plate leading edge in a region where strong interaction regime occurs. The Cartesian coordinates (x,y,z) and corresponding velocities (u,w,v) are chosen in streamwise, vertical and spanwise directions, respectively. Freestream pressure, density, temperature and viscosity are denoted as p_∞, ρ_∞, T_∞, μ_∞ and the external flow velocity as U_∞.

The specific heat ratio γ and a Prandtl number σ are assumed to be constant, and the dependence of the viscosity on the temperature is taken in a power law form

$$\mu / \mu_\infty = (T / T_\infty)^\omega \qquad (2.1)$$

The mean flow is basically controlled by interaction between the boundary and shock layers and allows self-similarity. Its profile shown schematically in Fig. 1 includes three characteristic regions: viscous high-temperature boundary layer, inviscid shock layer and transitional layer appearing due to singularity in temperature behavior near upper edge of the boundary layer [2]. As the plate temperature decreases, the boundary layer solution becomes singular at the wall because the viscosity vanishes there, and according to [13,17], an additional fourth buffer layer occurs near the surface where heat and

momentum fluxes are constant while the temperature is of the order of the wall temperature and changes rapidly together with the velocity.

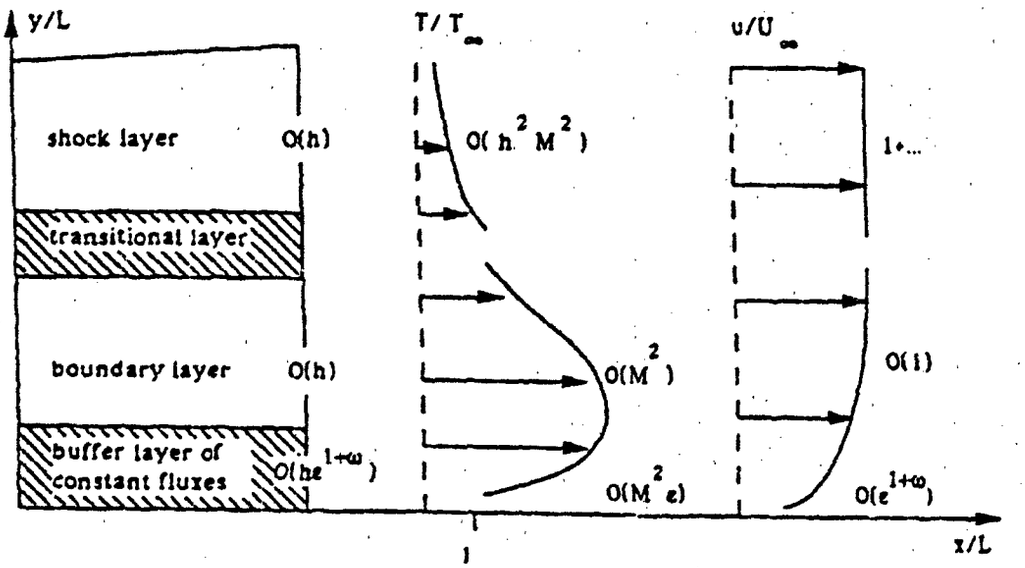

Fig.1 Qualitative distribution of mean flow temperatures and velocity across boundary layer.

For convenience, the following two small parameters characterizing mean flow are introduced

$$h = Re^{-1/4} M^{\omega/2}, \varepsilon = T_w / (M^2 T_\infty) , \tag{2.2}$$

where M is the Mach number, and Re is the Reynolds number. Both of these parameters are based on freestream conditions and the distance L. The quantity T_w is the wall temperature. For the strong interaction approximation to be applicable, the parameter h which is the relative thickness of the boundary layer must meet the additional constraint

$$hM \to \infty.$$

4.2.1 Preliminary considerations and scales

In this unsteady framework and consistent with the foregoing discussion, the characteristic length of the disturbances are assumed to be small in comparison with the global scale L, and their structure in the y-direction consists of multiple layers. There are at least two different regions: the main part of the boundary layer and a thin viscous wall sublayer. In what follows, the characteristic length and time of the perturbation are respectively denoted as Dx and Dt ;velocity and pressure variations as Du and Dp all

values referring to the viscous sublayer and to the main part of the boundary layer by subscripts v and b, respectively. For order-of-magnitude estimations it is assumed that:

(a) the pressure variation across the boundary layer is negligibly small.

(b) streamwise and spanwise scalings are the same.

(c) the viscous sublayer lies at the bottom of the buffer layer so that the undisturbed flow in that region has a linear shear velocity profile whose slope can be evaluated by comparison of the momentum flux on the surface with that of the boundary layer, so that

$$\mu(T_v)u_v / y_v \sim \mu(T_b)U_b / y_b, T_v \sim T_w$$

(d) Within this sublayer, the viscous forces are in balance with the inertia and pressure gradient terms so that

$$\rho_v \mu_v \Delta u_v / \Delta x \sim \Delta p / \Delta x \sim \mu_v \Delta u_v / y_v^2 .$$

(e) in the main part of the boundary layer the perturbation field is mainly inviscid so that only inertia and pressure gradient terms must be kept in balance. This implies

$$\rho_b u_b \Delta u_b / \Delta x \sim \Delta p / \Delta x ,$$

(f) interaction occurs basically between the main part of the boundary layer and the viscous sublayer and perturbations of the displacement thickness have the same order in these layers

$$y_v \Delta u_v / u_v \sim y_b \Delta u_b / u_b .$$

(This follows [15] for the steady case.)

(g) flow in the viscous sublayer is unsteady and nonlinear with respect to the time and amplitude scaling of the disturbance

$$\Delta x / \Delta t \sim u_v, \Delta p \sim \rho_v u_v^2$$

For completeness, these estimations must be supplemented by the order of the mean boundary layer values

$$y_b \sim Lh, u_b \sim U_\infty, p_b \sim p_\infty h^2 M^2, T_b \sim T_\infty M^2 ,$$

as well as the equation of state

$$p / (\rho T) = \text{Const.}$$

These relations lead to a unique scaling for the perturbation field in the viscous sublayer and the main part of the boundary layer. To provide matching between these regions, an intermediate layer of the constant momentum and heat fluxes is considered. Its thickness y_{fl} may be evaluated by comparison of the heat flux near the surface and with that of the boundary layer. Thus,

$$\mu(T_w)T_w / y_{fl} \sim \mu(T_b)T_b / y_b.$$

Also for matching, a fourth upper layer located at the bottom of the shock layer is introduced. In that region, pressure variations in the vertical direction are assumed to be essential. Neglecting viscous forces, the thickness of this layer, Dy is given by the condition that the local slope of the characteristics has the same order as the relative thickness of the region,

$$\Delta y / \Delta x \sim 1 / M_{loc},$$

where the local Mach number, M_{loc} is connected with the local temperature T_{loc} within this layer

$$M_{loc} \sim M(T_{loc} / T_\infty)^{-1/2},$$

which, in turn, may be explicitly written following the asymptotic formulas (3.02), (3.13) in [2] reexpressed in terms of physical variables as

$$T_{loc} \sim T_\infty M^2 h^2 (\Delta y / Lh).$$

This completes the estimates. As shown in [15] for the upper layer, [17] and [13] for the buffer layer, both layers play a secondary role in the interaction but are necessary for rational formulation of the problem.

Coupling of all of the above estimations gives us the appropriate scaling, which may be written in terms of the small parameters h and e in the form

$$x = L(1 + \varepsilon^{2+4\omega} x_1), \qquad (2.3)$$

$$z = L\varepsilon^{2+4\omega} z_1,$$

$$t = (L / U_\infty)\varepsilon^{1+3\omega} t_1,$$

$$y = Lh(\varepsilon^{1+2\omega} y_1,\ \varepsilon^{1+\omega} y_2,\ y_3, y_{30} + \varepsilon^{2(1+2\omega)(3\gamma-2)/(3\gamma-1)} y_4).$$

The perturbation field is schematically shown in Fig. 2. It is decomposed into four characteristic regions: the lower viscous region $y_1 = O(1)$, the buffer layer $y_2 = O(1)$, the mean part of the boundary layer $y_3 = O(1)$, and the upper layer $y_4 = O(1)$ located at the bottom of the shock layer above the boundary layer upper edge $y_3 = y_{30}$. Assumption (a) that the pressure variation across the boundary layer is negligible will be correct if the following restriction on the small parameters is valid:

$$h\varepsilon^{-2-4\omega} \to 0, \tag{2.4}$$

i.e., the streamwise scale is greater than the thickness of the boundary layer. With such a restriction, the upper deck will always be thicker than the transitional layer at any realistic (σ, γ, ω).

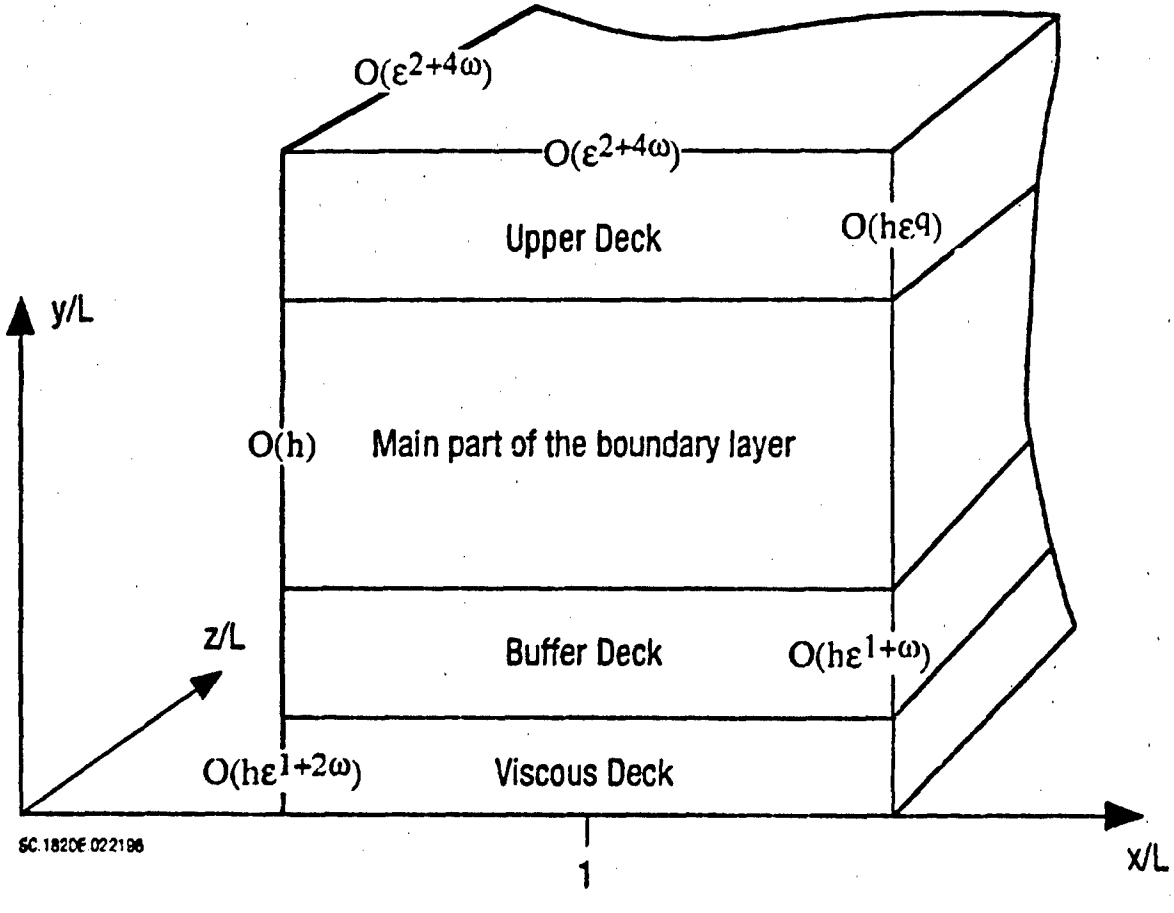

Fig. 2 Asymptotic structure of the perturbation field, $q = 2(1+2\omega)(3\gamma-2)(3\gamma-1)$.

4.3 Asymptotic approach.

From condition (g), a typical amplitude of the perturbation within each layer can be formulated. For these, the independent variables for the n^{th} region are $\{x_1, z_1, t_1, y_n\}$, respectively, with $n = 1,\ldots,4$. These will be studied in the next subsections.

4.3.1 The viscous sublayer $y_1 = O(1)$

The solution in this layer is represented in the form

$$p = p_\infty h^2 M^2 (p_{10} + \varepsilon^{1+2\omega} p_{11} + \ldots) \tag{3.1}$$

$$u = U_\infty \varepsilon^{1+\omega} u_{11} + \ldots$$

$$w = U_\infty \varepsilon^{1+\omega} w_{11} + \ldots$$

$$v = U_\infty h \varepsilon^{-\omega} v_{11} + \ldots$$

$$T = T_\infty M^2 (\varepsilon T_{01} + \ldots)$$

$$\rho = \rho_\infty h^2 (\varepsilon^{-1} \rho_{10} + \ldots)$$

In the absence of perturbations, the solution is a uniform shear flow

$$T_{01} = 1,\ p_{10} = \rho_{10} = p_0,\ u_{11} = C_1 y_1,\ w_{11} = 0, \tag{3.2}$$

where the undisturbed pressure p_0 and shear stress C_1 are determined by matching with the remainder of the mean flow. Substituting the expansions in the equations and retaining like orders gives

$$p_0(\partial u_{11} / \partial t_1 + u_{11}\partial u_{11} / \partial x_1 + v_{11}\partial u_{11} / \partial y_1 + w_{11}\partial u_{11} / \partial z_1 + \gamma^{-1}\partial p_{11} / \partial x_1 = \partial^2 u_{11} / \partial y_1^2 \tag{3.3a}$$

$$p_0(\partial w_{11} / \partial t_1 + u_{11}\partial w_{11} / \partial x_1 + v_{11}\partial w_{11} / \partial y_1 + w_{11}\partial w_{11} / \partial z_1 + \gamma^{-1}\partial p_{11} / \partial z_1 = \partial^2 w_{11} / \partial y_1^2 \tag{3.3b}$$

$$p_{11} = p_{11}(x_1, z_1, t_1) \tag{3.3c}$$

$$\partial u_{11} / \partial x_1 + \partial w_{11} / \partial z_1 + \partial v_{11} / \partial x_1 = 0 \tag{3.3d}$$

The boundary conditions on the surface are the no-slip conditions

$$u_{11} = v_{11} = w_{11} = 0 \text{ at } y_1 = 0. \tag{3.3e}$$

At the outer edge of the layer, the asymptotic behavior of the solution is

$$u_{11} = C_1 y_1 + A(x_1, z_1, t_1) + \dots,$$

$$w_{11} = -(\gamma p_0 C_1 y_1)^{-1} \int (\partial p_{11} / \partial z_1) dx_1 + \dots,$$

$$w_{11} = -(\gamma p_0 C_1 y_1)^{-1} \int (\partial p_{11} / \partial z_1) dx_1 + \dots \quad \text{as } y_1 \to \infty \tag{3.3f}$$

To complete the problem (3.3) a relation between the pressure perturbations $p_{11}(x_1, z_1, t_1)$ and the displacement thickness $-A(x_1, z_1, t_1)$ must be applied. This relation (interaction law) will be obtained after analysis of the other decks.

4.3.2 The buffer region $y_2 = O(1)$

Although this layer is still thin in comparison with the boundary layer, variations of the mean flow temperature and density within it are not small. Requirement of continuity of the pressure and the appearance of the asymptotics (3.3f) rewritten in terms the variable y2 implies the following expansions in the buffer region

$$p = p_\infty h^2 M^2 (p_{20} + \varepsilon^{1+2\omega} p_{21} + \dots) \tag{3.4}$$

$$u = U_\infty (\varepsilon u_{20}(y_2) + \varepsilon^{1+\omega} u_{21} + \dots)$$

$$w = U_\infty \varepsilon^{1+2\omega} w_{21} + \dots$$

$$T = T_\infty M^2 (\varepsilon T_{20}(y_2) + \varepsilon^{1+\omega} T_{21} + \dots)$$

$$\rho = \rho_\infty h^2 \varepsilon^{-1} \rho_{20}(y_2)$$

The orders of the temperature and density disturbances in the above expansions are estimated from the energy and state equations. Substituting these expansions gives the problem for the mean flow and unsteady perturbations. The mean flow is characterized by constant fluxes of heat and momentum, *i.e.*

$$d((T_{20})^\omega du_{20} / dy_2) / dy_2 = 0 \tag{3.5}$$

$$d((T_{20})^\omega dT_{20} / dy_2) / dy_2 = 0$$

$$\rho_{20} T_{20} = p_{20} = \text{Const.}$$

The boundary conditions are

$$T_{20} = 1, u_{20} = 0 \text{ at } y_2 = 0. \tag{3.6}$$

This system leads to the solution

$$T_{20} = (1 + C_2(1+\omega) y_2 \tag{3.7}$$

$$u_{20} = (C_1 / C_2)(T_{20} - 1)$$

$$p_{20} = p_0$$

$$\rho_{20} = p_0 / T_{20}.$$

The pressure p_0, wall shear stress C_1 and heat flux C_2 cannot be specified until the global mean flow solution is obtained. The next approximation gives us the perturbation field equations

$$u_{20} \partial u_{21} / \partial x_1 + v_{21} du_{20} / dy_2 = 0 \tag{3.8a}$$

$$\rho_{20} u_{20} \partial w_{21} / \partial x_1 + \gamma^{-1} \partial p_{21} / \partial z_1 = 0 \tag{3.8b}$$

$$\partial p_{21} / \partial y_2 = 0 \tag{3.8c}$$

$$u_{20} \partial T_{21} / \partial x_1 + v_{21} dT_{20} / dy_2 = 0 \tag{3.8d}$$

$$\rho_{20} \partial u_{21} / \partial x_1 + u_{20} \partial \rho_{21} / \partial x_1 + \partial(\rho_{20} v_{21}) / \partial y_2 = 0. \tag{3.8e}$$

$$\rho_{21} / \rho_{20} + T_{21} / T_{20} = 0 \tag{3.8f}$$

This is a system of linear inviscid equations with the absence of the pressure gradient in the x-momentum and energy equations. Note also that this deck and all decks above are quasi-steady in contrast to the viscous sublayer as for other speed regimes. Formally, the problem (3.8) is second-order with respect to the vertical variable y_2 (eqs. (3.8c),(3.8e)). To obtain a unique solution it is therefore sufficient to specify continuity of the pressure and matching of the y-component of the velocity with asymptotic (3.3f) at the outer edge of the viscous sublayer. By direct substitution, it can be verified that a solution of the system (3.8) meeting these conditions is

$$p_{21} = p_{11}(x_1, z_1, t_1) \tag{3.9}$$

$$u_{21} = A(x_1, z_1, t_1)C_1^{-1} du_{20} / dy_2$$

$$w_{21} = -T_{20}(gp_0 u_{20})^{-1} \int (\partial p_{11} / \partial z_1)\, dx_1$$

$$v_{21} = -u_{20} C_1 \partial A / \partial x_1$$

$$T_{21} = AC_1^{-1} dT_{20} / dy_1$$

$$\rho_{21} = -AC_1^{-1}(\rho_{20} / T_{20}).$$

4.3.3 Main part of the boundary layer $y_3 = O(1)$)

Asymptotic expansions within this region may be obtained by analysis of the limiting form of the buffer-layer solution (3.9) for large y_2 in terms of the variable y_3, or by direct estimation from the equations of motion, assuming that the pressure perturbation is of the same order as before. This gives

$$p = p_\infty h^2 M^2 (p_{30} + \varepsilon^{1+2\omega} p_{31} + \ldots) \qquad (3.10)$$

$$u = U_\infty (u_{30}(y_3) + \varepsilon^{1+2\omega} u_{31} + \ldots)$$

$$w = U_\infty \varepsilon^{1+2\omega} w_{31} + \ldots$$

$$v = U_\infty h(\varepsilon^{-1-2\omega} v_{31} + \ldots + v_{30}(y_3) + \ldots)$$

$$T = T_\infty M^2 (T_{30}(y_3) + \varepsilon^{1+2\omega} T_{31} + \ldots)$$

$$\rho = \rho_\infty h^2 \rho_{30}(y_3),$$

where the out-of-order term v_{30} included in the expansions for the vertical velocity is not involved in the leading-order problem for the disturbances but is necessary for a consistent description of the mean flow. The unperturbed boundary layer flow profile is locally uniform (no dependence on the short scale streamwise variable x_1) and obeys the system of ordinary differential equations that result from the usual three quarter power similarity (see for example [20]). A complete formulation also includes the problem for the inviscid shock layer. This complete system was investigated in detail in [2], and in von Mises variables in [3]. A brief analysis of the problem in terms of the physical independent variables is given in the Appendix. Here, we note only that the undisturbed pressure is constant and the temperature and density distributions are connected by the state equation

$$p_{30} = p_0, \rho_{30} T_{30} = p_0 \tag{3.11}$$

The leading-order problem for the perturbations has the form

$$\rho_{30}(u_{30}\partial u_{31} / \partial x_1 + v_{31} du_{30} / dy_3 + \gamma^{-1}\partial p_{31} / \partial x_1 = 0 \tag{3.12a}$$

$$\rho_{30} u_{30}\partial w_{31} / \partial x_1 + \gamma^{-1}\partial p_{31} / \partial z_1 = 0 \tag{3.12b}$$

$$\partial p_{31} / \partial y_3 = 0 \tag{3.12c}$$

$$\rho_{30}(u_{30}\partial T_{31} / \partial x_1 + v_{31} dT_{30} / dy_3 - (\gamma - 1)\gamma^{-1} u_{30}\partial p_{31} / \partial x_1 = 0 \tag{3.12d}$$

$$\rho_{31} / \rho_{30} + T_{31} / T_{30} = p_{31} / p_0. \tag{3.12e}$$

Like the problem (3.8) for the buffer layer, this gives rise to an inviscid linear system of second order with respect to the vertical variable, but with non trivial pressure gradient forces. Due to the inviscid nature of the problem, it is sufficient to apply conditions of continuity of the pressure

$$p_{11}(x_1, z_1, t_1), \tag{3.13}$$

and matching the vertical velocity component with the buffer region solution. It is shown in what follows that the upper region is also mainly inviscid and the same continuity conditions should be applied for its matching with the main part of the boundary layer. Therefore, the analysis can be limited to solution for the two variables p_{31}, v_{31} only. Successively excluding all other variables by expressing them in terms of p_{31}, v_{31}, and their derivatives gives accordingly

$$p_0\rho_{30}u_{30}\partial^2 v_{31} / \partial y_3\partial x_1 - p_0\rho_{30}(du_{30} / dy_3)\partial v_{31} / \partial x_1 +$$

$$\gamma^{-1}\rho_{30}u_{30}^2\partial^2 p_{11} / \partial x_1^2 - \gamma^{-1} p_0\left(\partial^2 p_{11} / \partial x_1^2 + \partial^2 p_{11} / \partial z_1^2\right) = 0 \tag{3.14}$$

The solution of Eq. (3.14) matched with the buffer layer is

$$\partial v_{31} / \partial x_1 = u_{30}(-C_1^{-1}\partial^2 A / \partial x_{1^2} + (\gamma p_0)^{-1}\int\{-\partial^2 p_{11} / \partial x_{1^2} + T_{30}u_{30}^{-2}\Delta p_{11}\}dy_3) \tag{3.15}$$

where the operator Δ is the two-dimensional Laplacian, *i.e.*

$$\Delta p_{11} \equiv \partial^2 p_{11} / \partial x_1^2 + \partial^2 p_{11} / \partial z_1^2. \tag{3.16}$$

The integrand in the right-hand side of the expression (3.15) has a singularity at $y_3 = 0$ which may be evaluated from asymptotics (A.4) as $O(y_3^{-1+\omega})$. Since it is a weak singularity for positive ω, the integral exists and the solution is regular at any $y_3 > 0$.

4.3.4 The upper region $y_4 = O(1)$

The undisturbed flow in this layer is an asymptotic "tail" of the shock layer solution considered by many authors (see, for example, [2,3]. These analyses show that the leading-order pressure and velocity are constant in this layer while the temperature and density have a power law singularity at the lower boundary ($y_4 \to 0^+$). Assuming the pressure perturbation to be of the same order as that within the boundary layer, the amplitudes of the other perturbation components can be estimated. This leads to solution expansions in the form

$$p = p_\infty h^2 M^2 (p_{40} + \varepsilon^{1+2\omega} p_{41} + \ldots) \tag{3.17}$$

$$u = U_\infty (1 + \ldots)$$

$$v = U_\infty h (v_{40} + \varepsilon^{3(1+2\omega)(\gamma-1)/(3\gamma-1)} v_{41} + \ldots)$$

$$T = T_\infty h^2 M^2 \varepsilon^{-4(1+2\omega)/(3\gamma-1)} (T_{40}(y_2) + \varepsilon^{1+2\omega} T_{41} + \ldots)$$

$$\rho = \rho_\infty \varepsilon^{4(1+2\omega)/(3\gamma-1)} (\rho_{40}(y_2) + \varepsilon^{1+2\omega} \rho_{41} + \ldots)$$

The above expansions do not include perturbations of the stream- and spanwise velocity components since, like the mean flow problem, the leading-order equations for the perturbations decouples and these velocities are not involved in the problem for $\{p, \rho, T, v\}$.

The mean flow distribution may be obtained in an explicit form from results of the previously mentioned authors, giving after some manipulation of the dependent and independent variables

$$p_{40} = p_0 \tag{3.18}$$

$$v_{40} = (3/4) y_{30}$$

$$T_{40} = B (y_4)^{-2/(3\gamma-2)}$$

$$\rho_{40} = p_0 B^{-1} (y_4)^{2/(3\gamma-2)}$$

Here, the constant B is expressed in terms of the the boundary layer pressure p_0 and the location of the shock layer y_{31} as

$$B = \{3^8 2^{-9}(\gamma+1)^{-3(\gamma+1)}(\gamma-1)^{3\gamma}(3\gamma-2)^{-2}\gamma^5 y_{31}^8\}^{1/(3\gamma-2)}.$$

In the next approximation, the equations for the perturbations take the form

$$\rho_{40}\partial v_{41}/\partial x_1 + \gamma^{-1}\partial p_{41}/\partial y_4 = 0 \tag{3.19a}$$

$$\rho_{40}(\partial T_{41}/\partial x_1 + v_{41}dT_{40}/dy_4) - (\gamma-1)\gamma^{-1}\partial p_{41}/\partial x_1 = 0 \tag{3.19b}$$

$$\partial\rho_{41}/\partial x_1 + \partial(\rho_{40}v_{41})/\partial y_4 = 0 \tag{3.19c}$$

$$\rho_{41}/\rho_{40} + T_{41}/T_{40} = p_{41}/p_0 \tag{3.19d}$$

This system is reduced to a second-order equation for the pressure with boundary conditions of continuity of the pressure at the lower boundary and a radiation condition at the upper one. This leads to a standard hyperbolic problem in a nonuniform medium

$$\partial^2 p_{41}/\partial x_{1^2} - \partial\{T_{40}\partial p_{41}/\partial y_4\}/\partial y_4 = 0 \tag{3.20a}$$

$$p_{41} = p_{11} \quad \text{at} \quad y_4 = 0 \tag{3.20b}$$

$$\text{radiation: } \{\partial/\partial x_1 + \sqrt{T_{40}}\partial/\partial y_4\}p_{41} \to 0 \text{ as } y_4 \to +\infty. \tag{3.20c}$$

A formal solution of this problem may be obtained by application of the Fourier transformation with respect to x_1, solution of the resulting ordinary differential equation, and inversion. If the pressure on the lower boundary is decays sufficiently rapidly in the upstream direction, the solution exists and its explicit form is

$$p_{41} = \int_{-\infty}^{\infty}\{G(x_1-\xi, y_4)\{\partial p_{11}(\xi, z_1, t_1)/\partial\xi\}d\xi. \tag{3.21}$$

The kernel function G has the integral representation

$$G(\xi, y_4) = H(\xi - Y)\{1 - \pi^{-1}\Gamma(1-q)\sin(2\pi q)\cdot$$

$$\int_0^{\infty}(kY/2)^q I_q(kY)e^{-k\xi}dk/k, \tag{3.22}$$

where

$$B^{1/2}(1+r/2)^{-1}y_4^{1+r/2},\ r = 2/(3\gamma-2),\ q = (r+1)/(r+2)$$

Here, $H(x)$ is the Heaviside function and $I_q(x)$ is the modified Bessel function. Solutions for the other components may be expressed similarly. The expression for the velocity at the lower boundary is

$$v_{41} = -D\int_{-\infty}^{x_1} (\partial p_{11}(\xi, z_1, t_1)/\partial\xi)(x_1 - \xi)^{1-2q} d\xi \ , \tag{3.23}$$

where the factor D is

$$D = (\gamma\pi p_0)^{-1} B^{1-q}(r+2)^{1-q}\Gamma(1-q)\Gamma(2q-1)\Gamma^{-1}(q)\sin(2\pi q) .$$

At the outer edge of this region, the nearly uniform medium approximation becomes applicable. Accordingly, disturbances will propagate along characteristics. The disturbances will enter the main part of the shock layer along positive-slope first family characteristics and propagate up to the shock wave. They then reflect as characteristics of the opposite family toward the boundary layer. From an estimate of a typical slope of the characteristics within the shock layer it can be concluded that the reflection zone lies downstream of a distance of the order of L. Assuming the upstream influence through the boundary layer is weak, the reflection effect can therefore be neglected.

Another comment concerns matching with the solution in the main part of the boundary layer. To provide this matching Bush in [2] has demonstrated that a thin transitional layer needs to be interspersed between the boundary and shock layers for the case $\gamma \neq 1$ where the singularity of the mean flow is being smoothed out. Without special analysis, it is evident that the viscous forces are still negligible in this region (for the perturbations only) and leading-order equations for the vertical component of the velocity and pressure are very simple, since both variables are constant in the vertical direction. This behavior may be established by direct order-of-magnitude estimations and also follows from the fact that the pressure and vertical velocity are finite at both edges of the transition region while its thickness is much less than the thicknesses of the boundary and upper layers. In other words, the transitional layer is passive with respect to type of the perturbations considered.

On the other hand, the typical amplitude of the vertical velocity in the boundary layer is much greater than within the upper deck. Therefore, the necessary matching condition is that the boundary layer velocity is zero at the upper edge, *i.e.*

$$v_{31} = 0 \text{ at } y_3 = y_{30}. \tag{3.24}$$

This means that the boundary layer disturbances are almost fully reflected by the shock layer. This result is actually the same as that obtained in [15] for rapidly varying steady

perturbations. Applying the requirement (3.24) to the formula (3.15) a relation between the pressure and displacement thickness

$$-\partial^2 A / \partial x_1^2 + C_1(\gamma p_0)\int_0^{y_m} \{\partial^2 p_{11} / \partial x_1^2 + T u_{30}^{-2} \Delta p_{11}\} dy_3 = 0 \qquad (3.25)$$

is obtained. Equation (3.25) completes the problem (3.3) for the viscous sublayer. This gives a new kind of triple-deck problem with a different interaction law than previously considered. In the two-dimensional case, the last term in (3.25) degenerates, and the formula is reduced to a more simple form

$$A + \text{const}\ p_{11} = 0$$

which was analyzed in[16] and [21].

4.3.5 Final formulation.

The problem (3.3) with the interaction law (3.25) is now considered. To reduce it to an invariant form, an additional transformation of the dependent and independent variables

$$(x_1, z_1) = p_0 C_1^{-3} y_{30}^{-3}(X, Z);\ (u_{11}, w_{11}) = C_1^{-1} y_{30}^{-1}(U, W)$$

$$(x_1, z_1) = p_0 C_1^{-2} y_1^{-1} Y;\ v_{11} = p_0^{-1} C_1^2 y_{30} V$$

$$t_1 = p_0 C_1^{-4} y_{30}^{-2} T;\ p_{11} = \gamma p_0 (C_1 y_{30})^{-2} P, \qquad (3.26)$$

is applied. A new parameter θ depending on the properties of the gas via parameters (σ, γ, ω)

$$\cos^2\theta = (y_{30})^{-1}\int_0^{y_m} T_{30} u_{30}^{-2} dy_3 \qquad (3.27)$$

is also introduced. Numerical values for all factors used in this scaling are given for air and helium in Table 2 of the Appendix . The right-hand side of the last expression is the average value of the inverse square of the local Mach number across the boundary layer and is less than unity for both these gases (probably for most others as well). After substitution of the rescaled variables into (3.3), (3.25), the governing system of equations takes the form

$$U_T + UU_X + VU_Y + WU_Z + P_X = U_{YY} \qquad (3.28a)$$

$$W_T + UW_X + VW_Y + WW_Z + P_Z = W_{YY} \qquad (3.28b)$$

$$U_X + V_Y + W_Z = 0, \qquad (3.28c)$$

and the boundary conditions are

$$U = V = W = 0 \text{ at } Y = 0 \tag{3.29a}$$

$$U = Y + A(X,Z,T) + \ldots, W \to 0 \text{ as } Y \to \infty \tag{3.29b}$$

$$A_{XX} + \sin^2\theta P_{XX} - \cos^2\theta P_{ZZ} = 0. \tag{3.29c}$$

Here, subscripts denote corresponding partial derivatives and the function A is renormalized in the same way as the streamwise velocity. That formulation does not include any effects of forced disturbances coming from the surface or external flow. For a perturbed surface, such generalization can be made by simply changing the boundary condition (3.29a), to

$$U = W = 0, V = F_T \text{ at } Y = F(X,Z,T), \tag{3.29a'}$$

where the function F describes the scaled shape of the surface. Reformulation for the case of external flow disturbances demands a special study of their transformation within the shock layer and is outside the scope of this chapter. Instead of the homogeneous wall conditions (3.29a) the modified version (3.29a') will be applied in what follows. In keeping with the primary thrust of this study, a linear stability analysis of the resulting problem will be made.

4.4 Linearization and solution

In the linear approximation, the solution is expanded in a power series of a small parameter (a) characterizing the amplitude of the perturbation so that

$$U = Y + au + \ldots; W = aw + \ldots; V = av + \ldots; P = ap + \ldots; F = af + \ldots \tag{4.1}$$

Here and below, small letters denote only scaled values and do not correspond to primary dimensional variables as in Sections 2,3. Substitution of this representation into (3.28),(3.29) gives

$$u_T + Yu_X + v + p_X = u_{YY} \tag{4.2a}$$

$$w_T + Yw_X + p_Z = w_{YY} \tag{4.2b}$$

$$u_X + v_Y + w_Z = 0 \tag{4.2c}$$

$$u = -f, w = 0, v = f_T \text{ at } Y = 0 \tag{4.2d}$$

$$u_{XX} + \sin^2\theta p_{XX} - \cos^2\theta p_{ZZ} = 0, w \to 0 \text{ at } Y \to \infty \tag{4.2e}$$

For the solution of this problem to be unique, an initial condition at some instant of time must be specified. This condition is assumed to be

$$u = v = w = p = f = 0 \text{ at } T < 0, \tag{4.3}$$

implying that surface variations are switched on at $T = 0$. These variations are assumed to be bounded continuous functions vanishing in the X- and Z- directions

$$f(X,Z,T) \in C, f \to 0 \text{ as } X^2 + Z^2 \to \infty. \tag{4.4}$$

From the restriction (4.4) it is plausible that the solution is also bounded at any finite instant of time* and the double Fourier transformation with respect to the streamwise and spanwise variables can be applied. Based on the standard assumption that the temporal growth is not faster than the exponential one, the Laplace transformation with respect to the time can be applied. These transformations written symbolically as

$$L(T \to -i\omega)F(Z \to i\beta, X \to i\alpha)\{u,w,v,p,f\}, (\alpha,\beta) \in (-\infty,+\infty), (-i\omega) > 0 \tag{4.5}$$

reduce the problem (4.2),(4.3) to a system of ordinary differential equations (the Laplace transform variable was rotated in the complex plane for a more obvious analogy with the canonical triple-deck formulation to connect with previous work). The solution procedure has been used by many authors (for the three-dimensional unsteady case see for example, [12,22]. Differences with the present formulation relate only to the form of the interaction law used. For this reason details of all intermediate steps including the inversions back to the physical space will not be presented. Only the integral representation for pressure is given which is

$$p = (2\pi)^{-2} \int_{-\infty}^{+\infty} \exp\{i\alpha X + i\beta Z\} d\alpha\, d\beta \int_C \exp\{-i\omega T\} D^{-1}(\alpha,\beta,\omega) f(\alpha,\beta,\omega) d\omega \tag{4.6}$$

where the function $f(\alpha,\beta,\omega)$ is the shape of the surface under the transformations (4.5). For the problem considered here, the dispersion function D expressed in terms of the Airy function, Ai is

$$D(\alpha,\beta,\omega) = (i\alpha)^{1/3}[1 + (\beta/\alpha)^2]\{Ai(-z_0)\}^{-1} \int_{-z_0}^{\infty} Ai(z)dz + \sin^2\theta - (\beta/\alpha)^2 \cos^2\theta \tag{4.7}$$

$$z_0 = i\omega/(i\alpha)^{2/3}; -\pi < \arg(i\alpha) < \pi, (i\alpha)^{1/3} > 0 \text{ for } i\alpha > 0.$$

* Of course, it does not exclude the possibile existence of unbounded (unstable) solutions in the large-time limit.

The contour C in (4.6) passes from left to right half planes of the complex ω-plane above all singularities of the integrand (due to causality principle), and both its ends are directed into the lower halfplane to provide convergence of the inversion integral for p. Since the integrand is a function of the wavenumber (α,β), the contour C also depends on the wavenumber.

Properties of the solution are determined by zeroth of the dispersion relation (4.7) which correspond to eigenmodes of our problem.

4.4.1 Analysis of the eigenmodes

Since the square of the spanwise wavenumber β occurs in the dispersion relation only the case $\beta \geq 0$ need be considered. Results of numerical analysis of the dispersion relation for θ=61.67_ corresponding to air (see the Appendix) are presented in Fig. 3. The simplest picture is observed in the two-dimensional case ($\beta = 0$). There is a denumerable set of eigenwavenumbers α with real positive frequencies, one of which lies in the left lower quadrant of the complex α-plane, and others move from the zero at $\omega = 0$ into the right upper quadrant. In the steady case, the first root may be written analytically as

$$i\alpha = \{-3A'(0)\sin^2\theta\}^3. \tag{4.8}$$

Accounting for the scalings (2.3), (3.26), this value agrees in the Newtonian limit discussed in [23] (noting that according to (3.27) $\sin\theta \to 1$ as $\gamma \to 1$) with the exponent in [16] their power law for disturbance propagation is converted to the approximate exponential form

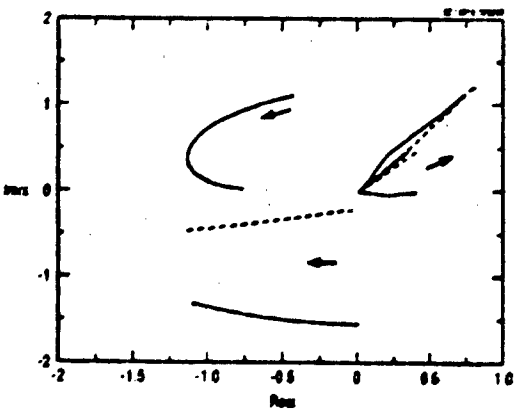

Fig. 3 Movement of the roots in complex plane as frequency goes from zero to infinity. (Solid, three-dimensional case at $\beta = 1$; dashed, plane modes at $\beta = 0$). Arrows indicate increasing frequency.

$$(x/L)^n \approx \exp(n\Delta x/L) \text{ as } n \to \infty,\ n\Delta x/L = O(1) \tag{4.9}$$

This implies that the two-dimensional steady state version of the asymptotic regime considered here describes the Neiland - Brown and Stewartson eigensolution.

In the three-dimensional case, all these modes also exist and exhibit the same qualitative behavior, but in addition, two more eigenwaves appear. One of these is located in the left upper quadrant and, like all previous ones, does not intersect the real axis. Another one starts from the zero in the right upper quadrant, but after some critical value of the frequency, intersects the real axis. The large-frequency limits of these modes are respectively

$$\alpha^{(1)} = -\beta\cot\theta + i0; \alpha^{(2)} = \beta\cot\theta - i0 \text{ as } \omega \to \infty. \tag{4.10}$$

The imaginary part of the second three-dimensional mode versus the frequency is shown in Fig. 4 at different positive spanwise wavenumbers β. As β is increased, the depth of the minimum also increases, *i.e.*

$$\min_{\omega>0}\{\mathrm{Im}(\alpha)\} \to -\infty \text{ as } \beta \to +\infty, \tag{4.11a}$$

or, similarly for the real wavenumbers and complex frequency

$$\max_{\alpha>0}\{\mathrm{Im}(\omega)\} \to +\infty \text{ as } \beta \to +\infty. \tag{4.11b}$$

Equations (4.11a) and (4.11b) imply that the contour C in the integral (4.6) actually depends only on the spanwise wavenumber β, and hence the order of integration with respect to frequency and streamwise wavenumber can be changed. Accordingly, Briggs' [24] criterion can be used to specify the direction of propagation of each eigenmode. According to this criterion, the streamwise wavenumber of the upstream (downstream) propagating eigenmode should belong to the lower (upper) halfplane for a sufficiently large imaginary part of the frequency. Specially conducted computations show that the root lying entirely in the lower half plane at real frequencies correspond to the upstream propagating wave, and all other modes propagate downstream with one of them being unstable. In particular, the stationary mode of Neiland-Brown and Stewartson propagates in the upstream direction.

Another important consequence of (4.11) is that the growth rate of the unstable eigenmode goes to infinity as the wavelength decreases. In fact, realistic physical systems do not contain infinitely fast growing modes, and the present situation is a result of simplifications made in the asymptotic limit considered. Thus, the possibility of well-posing of the forced problem requires additional investigation.

4.4.2. *Analysis of the initial boundary-value problem*

In typical formulations of the forced problem, the large time behavior of the boundary surface is assumed to be harmonic. This implies that the function $f(\alpha,\beta,\omega)$ is analytic

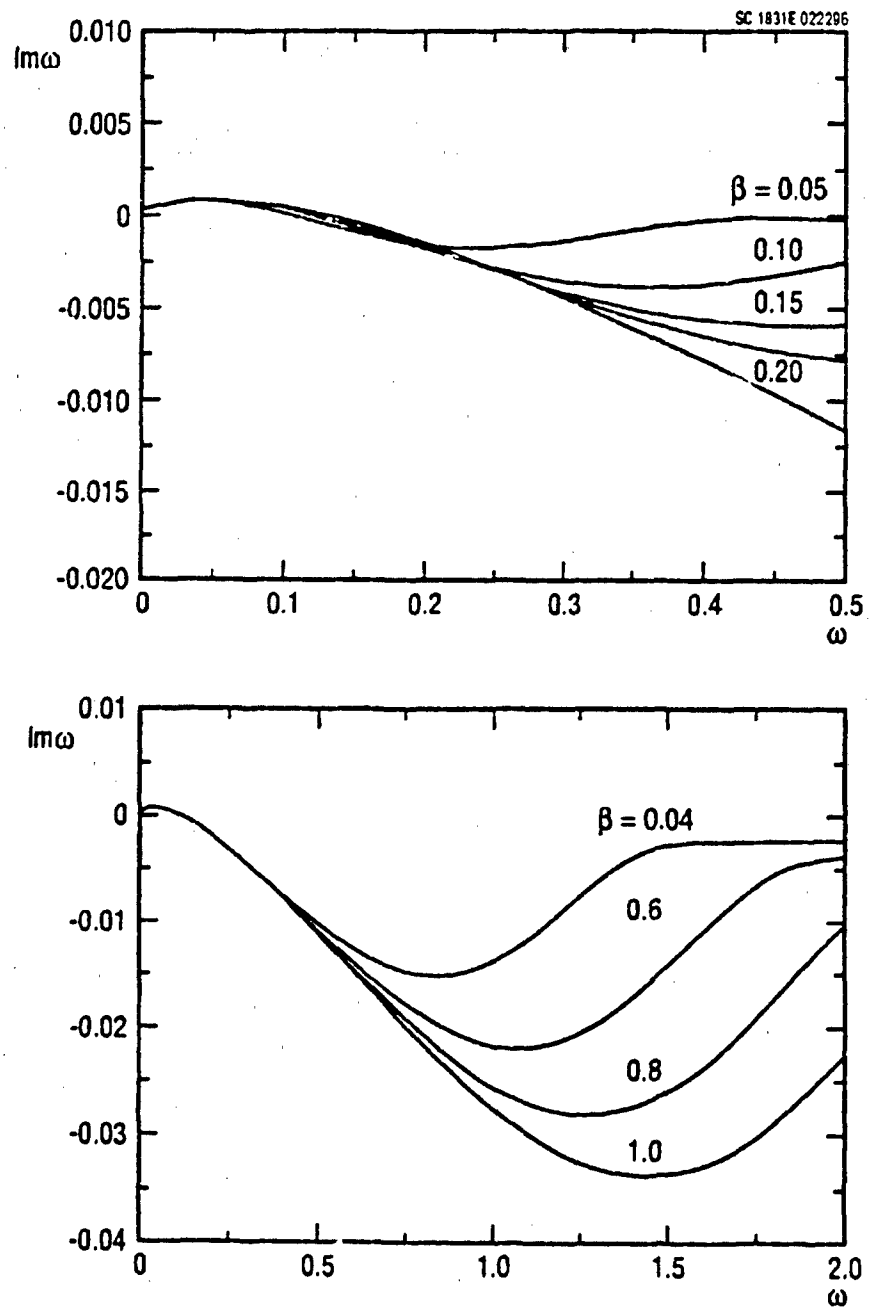

Fig 4 Imα vs. ω for unstable mode at (a) $\beta = .05, .1, .15, .20 + \infty$, (b) $\beta = .4, .6, .8, 1.$

with a simple pole at some real frequency $\omega = \omega_0 > 0$. To provide the existence of the solution of the forced problem which is equivalent to convergence of the integral (4.6), the class of the surface shape functions is restricted by imposing limitations on their decay in wavenumber space. Properties of the solution for this set are investigated in what follows. Implications of relaxing these limitations are then considered. For simplicity, the special case of shape functions of compact support in the b-direction

$$f_n(\alpha,\beta,\omega) = \begin{cases} f(\alpha,\beta,\omega) \text{ for } |\beta| < \beta_n \\ 0 \text{ for } |\beta| > \beta_n; \beta_n \to +\infty \text{ as } n \to \infty. \end{cases} \tag{4.12}$$

is studied. Within this class of functions, the infinitely fast growing waves are excluded and the solution does exist. The region far downstream from the source of the perturbations where the unstable eigenmode dominates is now considered. Accordingly, only the contribution of the unstable eigenmode is important. For convenience, the order of integration is reversed with respect to α and ω, and the integrals with respect to each variable are considered successively. The first integral may be estimated as

$$\int_{-\infty}^{\infty} e^{i\alpha x} f(\alpha,\beta,\omega) D^{-1}(\alpha,\beta,\omega) d\alpha \approx 2\pi i \exp(i\alpha_1 X) f(\alpha_1,\beta,\omega) \{D_\alpha(\alpha_1,\beta,\omega)\}^{-1} \tag{4.13}$$

Here $\alpha_1 = \alpha_1(\beta,\omega)$ is the root of the dispersion relation corresponding to the unstable mode. The next integral with respect to the frequency contains contributions of the shape function pole at $\omega = \omega_0$ and the branch points $\partial D / \partial \alpha = 0$. Dividing it into the time-harmonic contribution written in an explicit form and a remainder term I_r, gives

$$\int_C \exp(-i\omega T + i\alpha_1 X) f(\alpha_1,\beta,\omega) \{D_\alpha(\alpha_1,\beta,\omega)\}^{-1} d\omega \approx -2\pi i \exp(-i\omega_0 T + i\alpha_{10} X) \operatorname{res}[f(\alpha_{10},\beta,\omega_0)] \{D_\alpha(\alpha_{10},\beta,\omega_0)\}^{-1} + I_r, \tag{4.14}$$

where $\alpha_{10} = \alpha_1(\beta,\omega_0)$. The first term of the representation (4.14) includes only the modes with bounded growth rates so that its behavior is regular as $\beta \to \infty$. The second term contains the modes growing infinitely fast as $\beta \to \infty$.

At finite X and T, I_r in (4.14) can be estimated approximately by the method of steepest descent assuming the spanwise wavenumber b is large. In that limit the eigenvalue is expanded into the descending power series in β

$$\omega = \beta\Omega; \alpha_1 = \beta A_0(\Omega) + \beta^{1/2} A_1 + \ldots, \tag{4.15}$$

where the coefficients A_k are described by the implicit equations obtained after substitution of the expansion (4.15) into the dispersion relation (4.7)

$$(1+A_0{}^2)A_0+\Omega(\sin^2\theta A_0{}^2-\cos^2\theta)=0, \tag{4.16a}$$

$$A_1\{(A_0^2-1)/\Omega+2\cos^2\theta/A_0\}-A_0^2(-i\Omega)^{-5/2}(A_0^2+1)=0. \tag{4.16b}$$

There are three branches of (4.16a). The branch of interest here is confined within the finite region (*cf.* (4.10))

$$-\cot\theta<A_0<\cot\theta, |A_1|<\infty \text{ in } -\infty<\Omega<\infty. \tag{4.17}$$

The location of the saddle point in the ω-plane is determined from

$$d(\alpha_1 X-\omega T)/d\omega=0.$$

This gives

$$\omega_r=\beta\Omega_0+\beta^{1/2}\Omega_1+\ldots, \tag{4.18}$$

where the expansion terms are obtained from conditions

$$dA_0/d\Omega=T/X, \Omega_1=-dA_1/d\Omega\{d^2A_0/d\Omega^2\}^{-1}, \tag{4.19}$$

with all derivatives taken at $\Omega=\Omega_0$. Elementary analysis of the conditions (4.19) with (4.16) shows that the saddle point exists at $T/X<\cos^2\theta$, and its contribution is exponentially large, *i.e.*,

$$I_r=O(\exp[C\beta^{1/2}]), \text{ as } \beta\to\infty; X>T/\cos^2\theta, C>0. \tag{4.20}$$

In the region $X<T/\cos^2\theta$, the saddle point contribution is absent at large b and the remainder part I_r of the integral defined by (4.14) should be evaluated at finite values of β. For X and T large, I_r is evaluated from the contribution of the branch points $(\partial D/\partial\alpha=0)$ which are closest to the real axes in α- and ω-planes. If position of these points is denoted as

$$\alpha_{br}(\beta), \omega_{br}(\beta)$$

the value of I_r is roughly expressed by

$$I_r=O\{\exp[\mathrm{Im}(\omega_{br}(\beta)T-\alpha_{br}(\beta)X]\}. \tag{4.21}$$

This contribution represents a vorticity spot appearing when the oscillator starts its motion. This effect was considered in detail in [25] for two-dimensional subsonic boundary layers and in [22] for the three-dimensional case. All branches occur in the

lower half of the α- and ω-planes and do not intersect the real axis, so that the vorticity spot is convected downstream with finite velocity. The present case differs mainly because some of the branch points approach zero from below as $\beta \to 0$. However, they do not intersect the real axes so that

$$\mathrm{Im}\,\omega_{br} \le 0, \mathrm{Im}\,\alpha_{br} \le 0, \mathrm{Im}\,\omega_{br} / \mathrm{Im}\,\alpha_{br} \ge c_{min} > 0 \qquad (4.22)$$

Behavior of α_{br}, ω_{br} and $\mathrm{Im}\,\omega_{br} / \mathrm{Im}\,\alpha_{br}$ versus β for the first branching point of this kind is shown in Fig. 5. Relations (4.22) imply that I_r represents disturbances moving downstream with the finite velocity. On a ray $X/T = c < 1/\cos^2\theta$, (Case(i)) the disturbances are growing not faster than exponentially and are bounded at any β, while for $X/T > 1/\cos^2\theta$, (Case (ii)), they are unbounded as $\beta \to \infty$ in agreement with the formula (4.20).

The last integration in (4.6) with respect to the spanwise wavenumber gives a finite limit as $\beta_n \to \infty$ in Case(i) and generally has no limit in Case(ii)*. Therefore, the asymptotic regime considered is applicable for the region $X/T < 1/\cos^2\theta$ only. The perturbation field further downstream requires a special analysis of the high frequency eigenmodes.

For increasing time, the vorticity spot displays far downstream and the perturbations field consists of time-harmonic oscillations only. Thus

$$p \approx \int_{-\infty}^{\infty} \exp[i\beta Z + i\alpha_{10} X - i\omega_0 T]\, \mathrm{res}\,[f(\alpha_{10}, \beta, \omega_0)]\{D_\alpha(\alpha_{10}, \beta, \omega_0)\}^{-1} d\beta$$
$$X \to +\infty, X/T < c_{min} \qquad (4.23)$$

The distribution of the imaginary part of α_{10} versus β is shown in Fig. 6 for different frequencies. When the frequency is small, there is a minimum of $\mathrm{Im}\,\alpha_{10}$ at finite β. If the frequency exceeds some critical value ω^* (≈ 0.30 for air, ≈ 0.78 for helium), the minimum disappears and $\mathrm{Im}\,\alpha_{10}$ tends monotonically to its lower boundary as $\beta \to \infty$. Accordingly, the solution behavior is different for both cases.

Estimating the integral (4.23) by the method of steepest descent on a ray $Z = X\tan\varphi$, the position of the saddle point is determined by a condition

$$d(\alpha_{10} + \beta\tan\varphi)/d\beta = 0, \qquad (4.24a)$$

which is equivalent to Values of $\alpha_\varphi, \beta_\varphi$ corresponding to the saddle point can be calculated from (4.24b), and the growth rate σ can be determined along the ray considered to be

* Even if the shape function is rapidly decaying in β -direction so that the integral exists as $\beta_n \to \infty$, the temporal growth of the solution is faster than exponential and the application of the Laplace transformation is not correct

$$\sigma = -\mathrm{Im}[\alpha_\varphi + \beta_\varphi \tan\varphi]. \qquad (4.25)$$

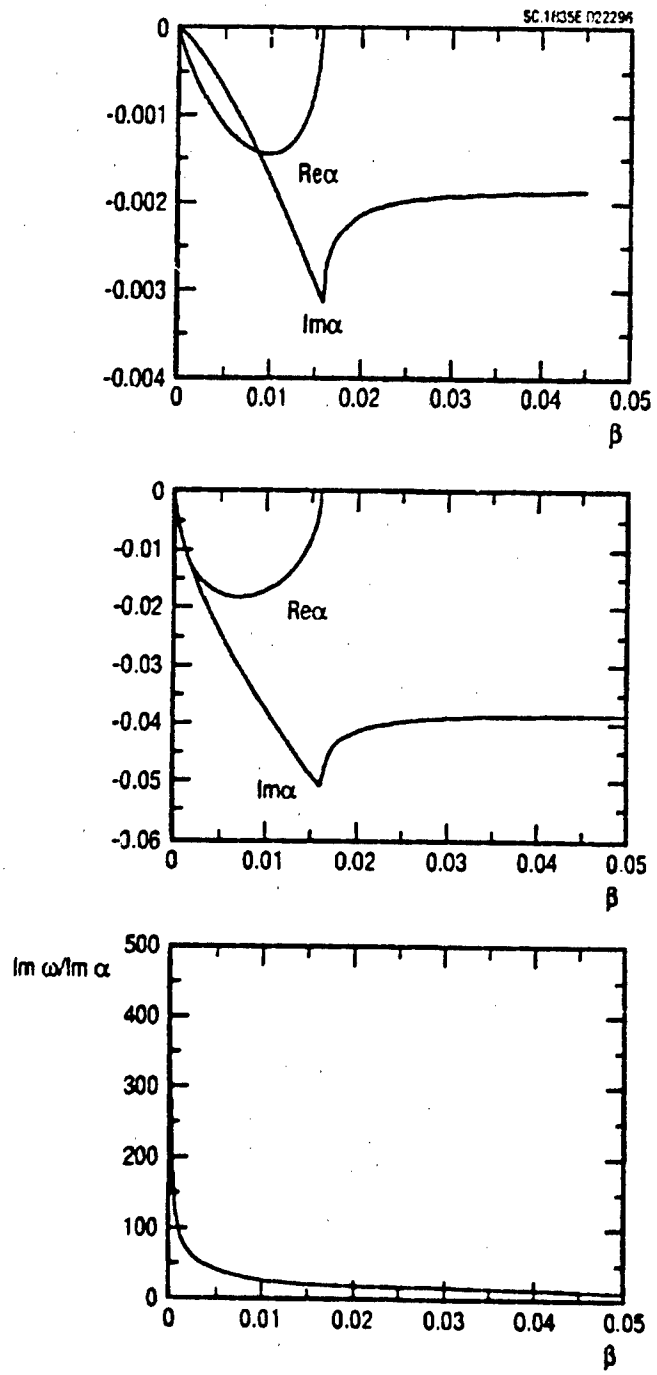

Fig. 5. Location of the first branch point (a) Re α and Im α vs. β, (b) Re ω and Imω vs. β, (c) Imω/Reω vs. β.

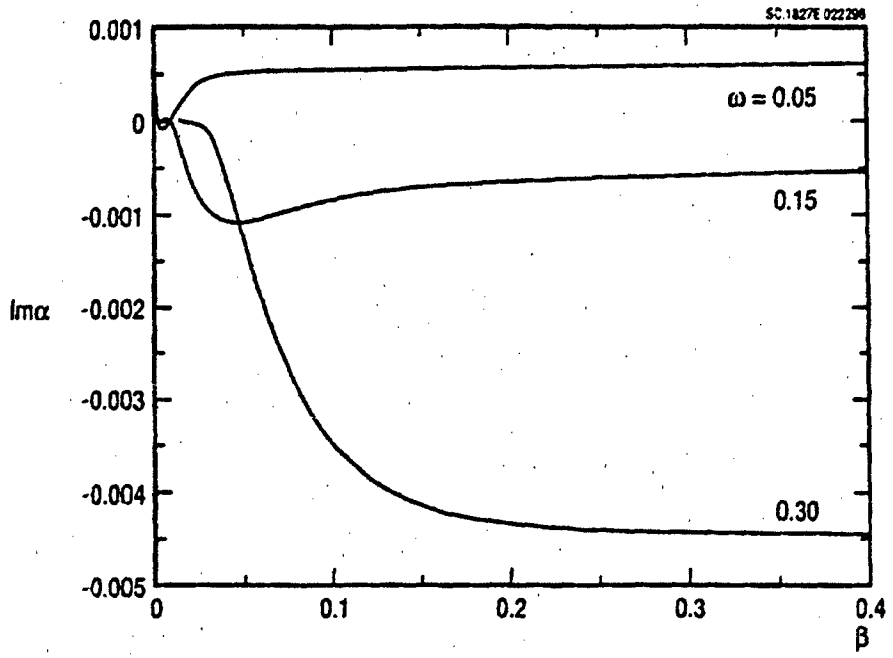

Fig.6 Imα vs. β for unstable mode at different frequencies ; ω=.05, .15, .30.

$$d\alpha_{10} / d\beta + \tan\varphi = 0. \qquad (4.24b)$$

If there is an angle φ_m of maximum amplification, the relation

$$d\sigma / d\varphi = \mathrm{Im}\{d\beta_\varphi / d\varphi[d\alpha_{10} / d\beta + \tan\varphi] + \beta_\varphi / \cos^2\varphi\} = 0 \text{ at } \varphi = \varphi_m. \qquad (4.26)$$

holds. Combination of (4.26) with (4.24b) leads to the conclusion that on the ray of maximum amplification the saddle point coincides with minimum of the function $\mathrm{Im}\,\alpha_{10}(\beta)$ at real β. Results of calculations of the angle φ_m and the corresponding growth rates are given in Fig. 7. For frequencies below the critical value ω^*, this angle is different from zero so that the far field disturbance distribution consists of two Gaussian humps in the spanwise direction at $Z = \pm X\tan\varphi_m$ with typical width $O(\sqrt{X})$. Their maximum amplitude is

$$p \approx [\pi / \alpha_{10}''(\beta_\varphi)X]^{1/2} \exp[i\alpha_\varphi X + i\beta_\varphi Z - i\omega_0 T] \times$$

$$\mathrm{res}\{f(\alpha_\varphi, \beta_\varphi, \omega_0)\} / \{D_\alpha(\alpha_\varphi, \beta_\varphi, \omega_0)\},\ \varphi = \varphi_m \qquad (4.27)$$

The case $\omega_0 > \omega^*$ cannot be considered in the same way as previously, and requires a special analysis. For this case, the main contribution in the integral (4.23) is given by the most unstable modes now concentrated at the large β. The approximate form of the eigenvalue in this region is

$$\alpha_{10} = a_0(\omega_0) + \beta^{-2}a_1 + \ldots \tag{4.28}$$

where the terms of the expansion are obtained from

$$D_0(a_0) \equiv (ia_0)^{1/3}\{\mathrm{Ai}'(-z_0)\}^{-1}\int_{-z_0}^{+\infty}\mathrm{Ai}(z)dz - \cos^2\theta,\ z_0 = i\omega_0/(ia_0)^{2/3}$$
$$a_1 = -a_{0^2}/D_0'(a_0). \tag{4.29}$$

Dependence a_0 on the frequency is shown in Fig. 4a as the limiting curve as $\beta \to \infty$. At the low frequencies (the neutral frequency for air ω_n=0.116, for helium ω_n=0.303), such limiting modes are stable, while at high frequencies the growth rate is unbounded. Due to the absence of the minimum in the distribution $\mathrm{Im}\,\alpha_{10}(\beta)$ the unequality

$$\mathrm{Im}\,a_1 > 0$$

holds. For this condition, the contribution of the region $\mathrm{Im}\,a_1 > 0$. in the integral (4.23) is exponentially small, and the approximate representation (4.28) can be used in the whole region of integration. Taking for simplicity the residual of the shape function equal to one (δ-function shape oscillator in the physical space), the solution can be written in the form

$$p \approx \exp[ia_0X - i\omega_0T]J(Z,X)/\{D_0(a_0)/a_0^2\}'$$

$$J(Z,X) = \int_{-\infty}^{+\infty}\exp[i\beta Z + ia_1\beta^{-2}X]d\beta/\beta^2. \tag{4.30}$$

Here

$D = (\beta/a_0)^2 D_0 + \ldots$ as $\beta \to \infty$. The value of J at Z=0 is finite

$$J = (-\pi/ia_1X)^{1/2},$$

and as $Z\sqrt{X} \to \infty$ it decays exponentially for $\mathrm{Im}\,a_1 > 0$. Thus

$$J \approx (\pi/6a_1X)^{1/2}\exp[3iZ^{3/2}X^{3/4}(a_1/4)^{1/3}].$$

Therefore, at supercritical frequencies $\omega > \omega^*$, the perturbation is concentrated in a thin region near the x-axis with a typical width $O\left(1/\sqrt{X}\right)$. A qualitative picture of the field of perturbations is shown in Fig. 8.4.5

4.5 Discussion and conclusions

The foregoing has shown that the strong interaction hypersonic boundary layer subject to surface cooling of the surface is unstable with respect to low phase speed (low frequency)

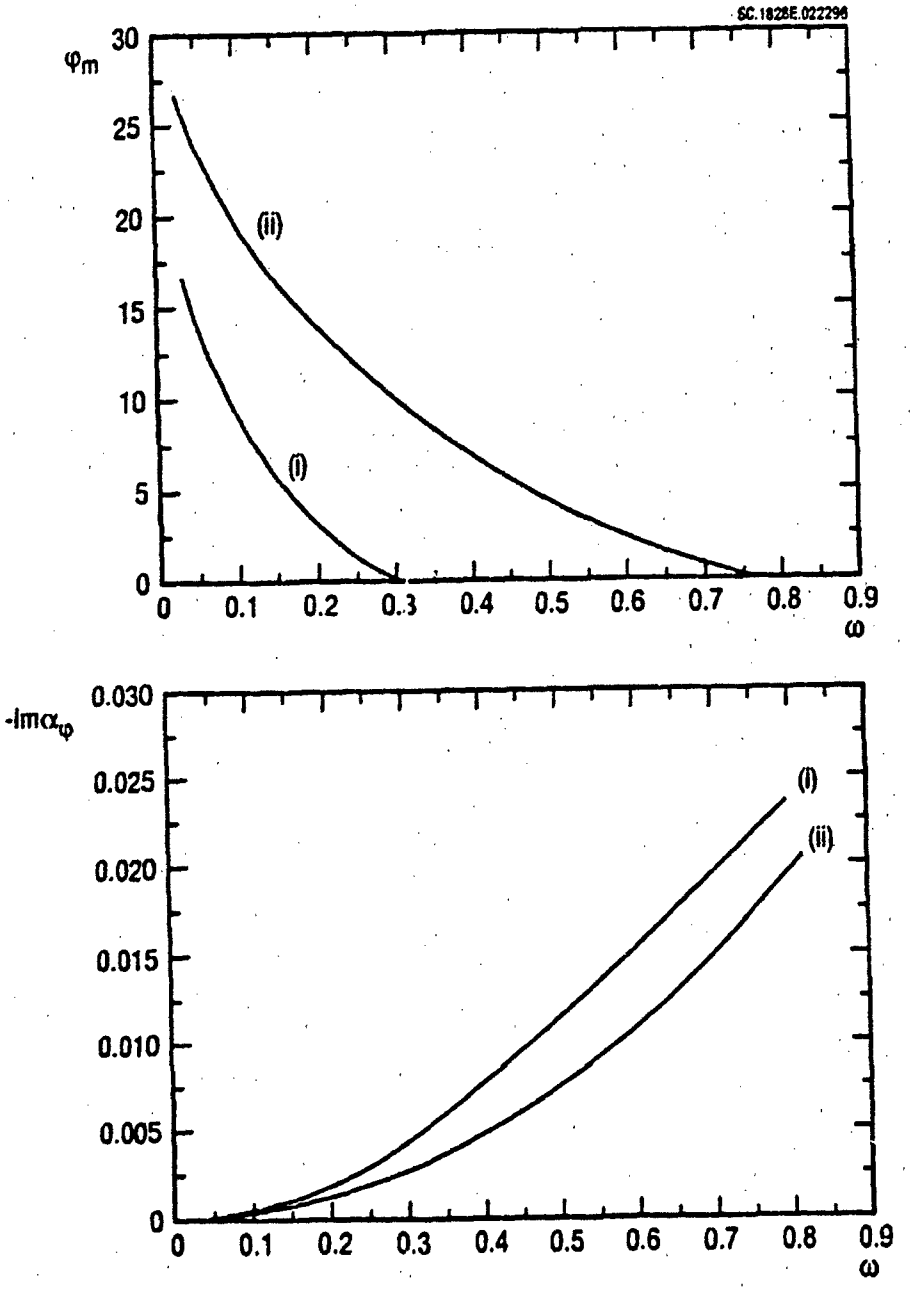

Fig. 7 Characteristics of the far downstream field from vibrator. (a) Angle of ray of maximum amplification φ_m^* vs. frequency of vibrator. (b) Growth rate on the ray of the maximum amplification versus frequency. (i):Air,(ii):Helium.

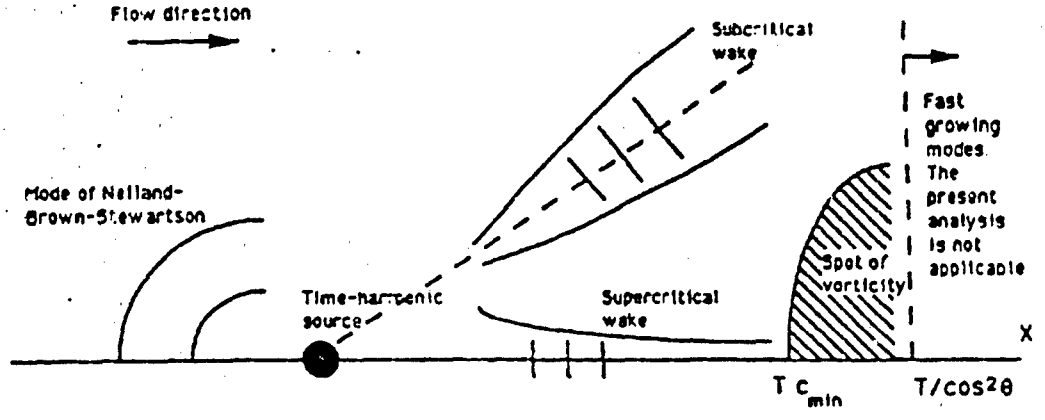

Fig. 8 Schematic picture of perturbation field induced by time-harmonic source on a surface.

viscous eigenwaves. This does necessarily preclude other types of instabilities. On the contrary, in addition to inviscid inflectional instability of the transitional layer considered before in [11], another inflectional instability should occur, because for sufficiently strong cooling a generalized inflection point appears within the boundary layer. (This can easily be concluded from analysis of the mean flow asymptotics near the wall). Results of computations for air presented in Fig. 9b (see the Appendix) indicate that such a point is located approximately in the middle of the boundary layer. Moreover, as follows from the analysis of [2], even for the hot wall and realistic gas parameters (σ, γ, ω) the mean flow velocity tends to the freestream value from above, and an additional inflection point exists near the upper edge of the boundary layer. Our computations (see the note in the end of the Appendix) show that this point is extremely close to the boundary layer edge and must be obscured by the transitional layer for realistic Mach numbers.

In any case, these inflectional instabilities have a typical frequency not less than the ratio of the freestream velocity to the thickness of the boundary layer in the strong interaction region. Typical frequencies associated with transition to turbulence are based on the boundary layer thickness far downstream and are much smaller than these inflectional instability frequencies. Therefore, the viscous instability considered may have more practical interest even if its growth rate is smaller than the inviscid one. This conjecture is supported by the experimental study by Holden [18,26] of the hypersonic boundary layer

on the cooled cone at zero angle of attack. He observed the occurrence of highly visible waves in the region where the ratio of thickness of the shock and boundary layers was

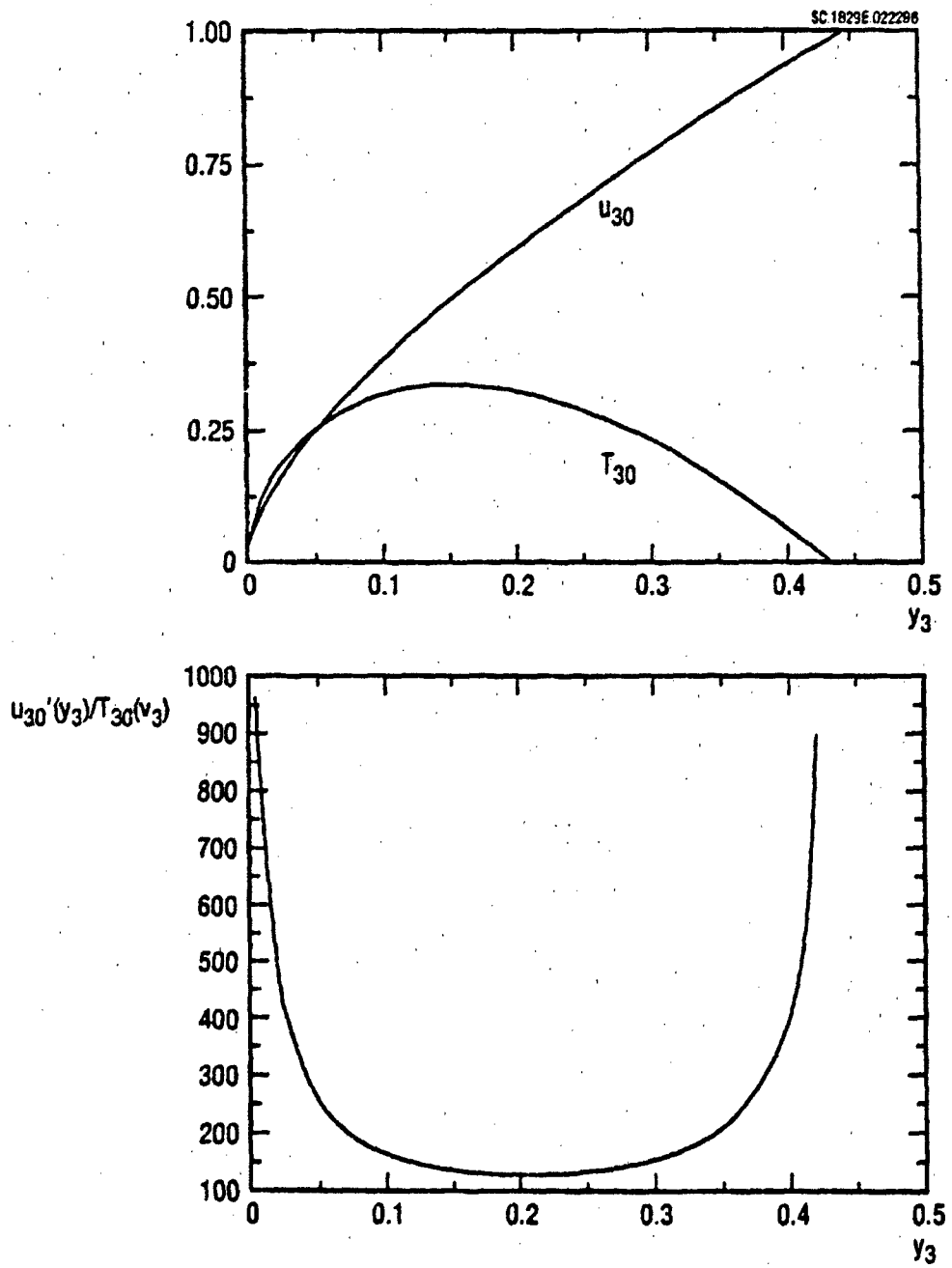

Fig. 9 (a) Mean flow distribution for velocity and temperature.(i) $u_{30}(y_3)$; (ii) $T_{30}(y_3)\cdot 10$ (b) Distribution of $u'_{30}(y_3)/T_{30}(y_3)$ within boundary layer. Minimum corresponds to generalized inflection point.

≈ 10 (under strong interaction it is ≈ 1.7 for flat plate in air). These waves were three-dimensional, had a continuously growing phase speed from 0.5 at the start of observations up to 0.85 at the end of transition. The effect of three-dimensionality is believed to be related to the type of instability considered here.

Another interesting observation was made in [19] in the study of hypersonic transition induced by a solitary roughness. Therein, it was found that if the distance between the nose and the roughness is less than some critical value, the wake behind the roughness has a thread-like form, and bursting into developed transition occurred far downstream. Our analysis shows that if the frequency of the source is less than some critical value, the far downstream perturbation field is like a swallow tail. For the high-frequency case, it narrows, with the width of the tail being inversely proportional to the square root of the distance from the source. The downstream growth rate increases with frequency (*cf.* results of calculations in Fig. 7 and qualitative picture in Fig. 8). Therefore the high frequency disturbances must dominate. Accordingly, the wake behind a point source with a broad spectrum of frequencies must concentrate near the central axis of the source, in agreement with the previously mentioned experimental result.

The physical mechanism of instability obtained is close to that analyzed in [12] for moderate supersonic speeds. In this case, instability occurs for the waves directed outside the free-stream Mach cone which are therefore effectively subsonic and qualitatively obey the same mechanism as Tollmien-Schlichting waves in incompressible boundary layers. For the case considered here, the disturbances are confined by the boundary layer and do not penetrate outside it, so that the interaction is realized between the viscous sublayer and the main part of the boundary layer. Hence, the role of the freestream Mach number is replaced by some effective Mach number averaged across the boundary layer. Since the local boundary layer Mach number is of the order of one the Mach cone angle takes on finite values different from $\pi/2$ and *independent* of the free-stream Mach number.

The important difference from the moderate supersonic regime is the presence of the infinitely fast growing modes in the short-wave limit. Therefore, the forced problem is well-posed on the class of shape functions of compact support in Fourier space. For a time-harmonic source switching on at some instant of time, the fast growing modes contribute to a vorticity spot which originates at the start of the oscillations and is convected downstream with finite velocity. Continuation to a wider class of the shape functions can be made in the region of physical space passed by the high-frequency vorticity spot and containing the time harmonic component only. The high-frequency part of the vorticity spot cannot be described within the present framework but needs consideration in another asymptotic regime.

4.6 References

1. Stewartson, K, . *The theory of laminar boundary layers in compressible flow*, Oxford, London, 1964.

2. Bush, W.B. "Hypersonic strong-interaction similarity solutions for flow past a flat plate," *J. Fluid Mech.* **25** 51-64, 1966.

3. Cheng, H.K., Lee, R.S. "On the outer-edge problem of a hypersonic boundary layer," *J. Fluid Mech.* **38** 161-179, 1969.

4. Malmuth, N.D. "Stability of the inviscid shock layer in strong interaction flow over a hypersonic flat plate,". In *Instabilities and Turbulence in Engineering Flows*, eds. D.E. Ashpis, T.B. Gatski and R. Hirsh. Kluwer Academic Publishers, 1993.

5. Balsa, T.F., Goldstein, M.E. "On the instabilities of supersonic mixing layers: a high Mach number asymptotic theory," *J. Fluid Mech.* **214** 585-611,1990.

6. Smith, F.T., Brown, S.N. "The linear inviscid instability of a Blasius boundary layer at large values of the Mach number," *J. Fluid Mech.* **219** 499-518, 1990.

7. Guschin, V.R., Fedorov, A.V. "Qualitative features of boundary-layer instability at high speeds of stream," *Mod. Mekh. Neod. Sistem*, ITPM SO AN SSSR, Novosibirsk, 93-116, 1989.

8. Cowley, S.J., Hall, P. "On the instability of hypersonic flow past a wedge," *J. Fluid Mech.* **214** 17-42, 1990.

9. Mack, L.M. *Boundary layer linear stability theory*. Jet. Prop. Lab. Doc. 900-277, Rev. A, Pasadena, 1969.

10. Grubin, S.E., Trigub, V.N. "Asymptotic stability theory of a hypersonic boundary layer," *Preprint TsAGI* **38** (In Russian.), 1991.

11. Blackaby, N., Cowley, S.J. and Hall, P. "On the instability of hypersonic flow past a flat plate," *J. Fluid Mech.* **247** 369-416, 1993.

12. Smith, F.T. "On the first-mode instability in subsonic, supersonic and hypersonic boundary layers," *J. Fluid Mech.* **198** 127-153, 1989.

13. Seddougui, S.O., Bowles, R.I. and Smith, F.T. "Surface-cooling effects on compressible boundary-layer instability," *Euro. J. Mech. B* **10** 117-145, 1991.

14. Neiland, V.Ya. "Upstream propagation of disturbances in hypersonic boundary layer interactions," *Izv. Akad. Nauk. SSSR, Mekh. Zhid. i Gaza* 4 40-49, 1970.

15. Brown, S.N. and Stewartson, K. "A non-uniqueness of the hypersonic boundary layer," *Q. J. Mech. Appl. Maths.* **28** 75-90, 1975.

16. Brown, S.N., Stewartson, K. and Williams, P.G. "Hypersonic self-induced separation," *Phys. Fluids* **18** 633-639, 1975.

17. Brown.S.N., Cheng, H.K. and Lee, C.J. "Inviscid-viscous interaction on triple deck scales in a hypersonic flow with strong wall cooling," *J. Fluid Mech.* **220** 309-337, 1990.

18. Holden, M.S. Studies of boundary layer transition and surface roughness effects in hypersonic flow. Calspan Report No *6430-A-5*, 1983.

19. Skuratov, S.A., Fedorov, A.V. "Supersonic boundary layer transition induced by small roughness on the attachment line of a yawed cylinder," *Izv. Akad. Nauk SSSR, Mekh. Zhid. i Gaza* **6** 28-35, 1991.

20. Hayes, W.D. and Probstein, R.F. *Hypersonic Flow Theory*, Academic Press, New York, 1959.

21. Gajjar, J., Smith, F.T. "On hypersonic self-induced separation, hydraulic jumps and boundary layers with algebraic growth," *Mathematica* **30** 77-93, 1983.

22. Ryzhov, O.S., Savenkov, I.V. "Asymptotic theory of a wave packet in a boundary layer on a plate," *J. Appl. Math. Mech.* **51** 644-651, 1987.

23. Cole, J.D. "Newtonian flow theory for slender bodies," *J. Aero. Sciences* **24** 448-455, 1957.

24. Briggs, R.J. *Electron Stream Interaction with Plasmas*. MIT Press, 1964.

25. Ryzhov, O.S., Terent'ev, E.D. 1986 On the transition mode characterizing the triggering of a vibrator in the subsonic boundary layer on a plate. *J. Appl. Math. Mech.* **50** 753-762.

26. Holden, M.S. 1985 Experimental studies of the effects of asymmetric transition on the aerothermal characteristics of hypersonic blunted slender cones. AIAA Paper No. *85-0325*.

4.7 Appendix. Undisturbed boundary layer.

In terms of the physical variables the system of equations controlling the mean boundary layer flow is

$$\Psi = \rho_{30}(3y_3 u_{30} - 4v_{30}) \tag{A.1}$$

$$\Psi' = \rho_{30}u_{30} - (\Psi/4)u'_{30} - p_0/2\gamma = ((T_{30})^{\omega}u'_{30})'$$

$$-(\Psi/4)T_{30} + p_0 u_{30}(\gamma-1)/2\gamma = (\gamma-1)T_{30}^{\omega}(u'_{30})^2 + \sigma^{-1}(T_{30}^{\omega}T'_{30})'$$

$$\rho_{30}T_{30} = p_0.$$

Here, Ψ is a stream function introduced for more convenient numerical integration, and prime denotes differentiation with respect to y_3. Boundary conditions are

$$\Psi = u_{30} = T_{30} = 0 \qquad \text{at } y_3 = 0 \tag{A.2}$$

$$\Psi \to \infty,\ v_{30} = 3y_{30}/4, u_{30} = 1,\ T_{30} = 0 \text{ at } y_3 \to y_{30}^{-0},$$

with the location of the upper boundary y_{30} determined simultaneously with the solution. The pressure p_0 is not a prescribed value but is determined only after coupling the problem (A.1),(A.2) with the problem for the inviscid shock layer. This layer is confined between the upper edge of the boundary layer y_{30} and the position of the shock wave $y_{31} > y_{30}$. Due to self-similarity, its profile is also described by a system of ordinary differential equations which are the reduced classical ones of hypersonic small perturbation theory, and may be treated as a locally uniform. Boundary conditions behind the shock wave are the Rankine-Hugoniot relations and the main-order matching conditions with the boundary layer which are continuity of the pressure and vertical velocity.

For complete formulation of the boundary layer problem the detailed structure of the shock layer flow is not necessary. Only an additional relation between the pressure and the vertical velocity at the upper edge (the global interaction law) is sufficient for obtaining a unique boundary layer solution. For evaluation of the mean flow in the Region 4 lying at the bottom of the shock layer, the location of the shock wave is required. Numerical data appropriate for these both purposes were obtained in [15]for mono- and diatomic gases. Their scaling formulae (2.1) and solution representation (2.9),(2.10) gives

$$p_0\{v_{30}(y_{30})\}^{-2} = (1/2)\gamma(\gamma+1)P_0(0)\{V_0(0)\}^{-2}, \tag{A.3}$$

$$y_{31} / y_{30} = (1/2)(\gamma + 1)\{V_0(0)\}^{-1},$$

where $P_0(0), V_0(0)$ are their scaled pressure and vertical velocity components at the bottom of the shock layer. Substitution of their numerical values gives the results in Table 1. For comparison the analytical result for Newtonian approximation ($\gamma \to 1$) is also shown.

Table 1

molecular structure	γ	$p_0\{v_{30}(y_{30})\}^{-2}$	y_{31} / y_{30}
one-atom	5/3	3.098	2.086
two-atom	7/5	1.990	1.691
	1+0	2/3	1

Noticeable differences in the global interaction law for the different values of the specific heats ratio appear because our primary scaling does not involve this parameter.

For integration of the problem (A.1), the boundary conditions (A.2) must be replaced by their asymptotic counterparts. Conditions at the wall follow from matching with the solution (3.7) within the buffer layer

$$T_{30} = (C_2(1+\omega)y_3 \qquad (A.4)$$

$$u_{30} = (C_1 / C_2)(C_2(1+\omega)y_3$$

Asymptotics near the upper edge were obtained [2] using stream function as the independent variable. In physical variables, they take the form

$$T_{30} = \mathrm{Const}_0(y_{30} - y_3)^{2/(1-\omega)} \qquad (A.5)$$

$$u_{30} = 1 + \mathrm{Const}_1(y_{30} - y_3)^{2/(1+\omega)},$$

where

$$\mathrm{Const}_0 = \{p_0\sigma(1+\omega)(1-\omega)^{-1}[1+(\gamma-1)(1-\omega)\gamma^{-1}]/4\}^{1/(1+\omega)} \qquad (A.6)$$

$$\mathrm{Const}_1 = (1-\omega)\{\gamma + (\gamma-1)(1-\omega)\}^{-1}\{1-\sigma(\gamma-1)(1-\omega)/\gamma\}^{-1}\mathrm{Const}_0.$$

Calculations were conducted by the Runge-Kutta method with variable step of integration for two sets of the gas parameters σ,γ,ω corresponding to helium and air. Numerical values characterizing the mean flow profile are presented in Table 2

Table 2

Gas	σ	γ	ω	C_1	C_2	p_0	y_{30}	y_{31}	$\theta°$
He	2/3	5/3	.647	.4294	.1334	.4538	.5103	1.064	52.94
Air	.72	7/5	3/4	.3895	.1328	.2151	.4384	.7413	61.67

Actually, these data are not far from the ones obtained in [3] for the Chapman viscosity law and Prandtl number equal to unity. The velocity and temperature distributions for air are presented in Fig. 9a, and distribution of the value $u'_{30}(y_3)/T_{30}(y_3)$ characterizing the location of the generalized inflection point is plotted in Fig. 9b. Behavior near the

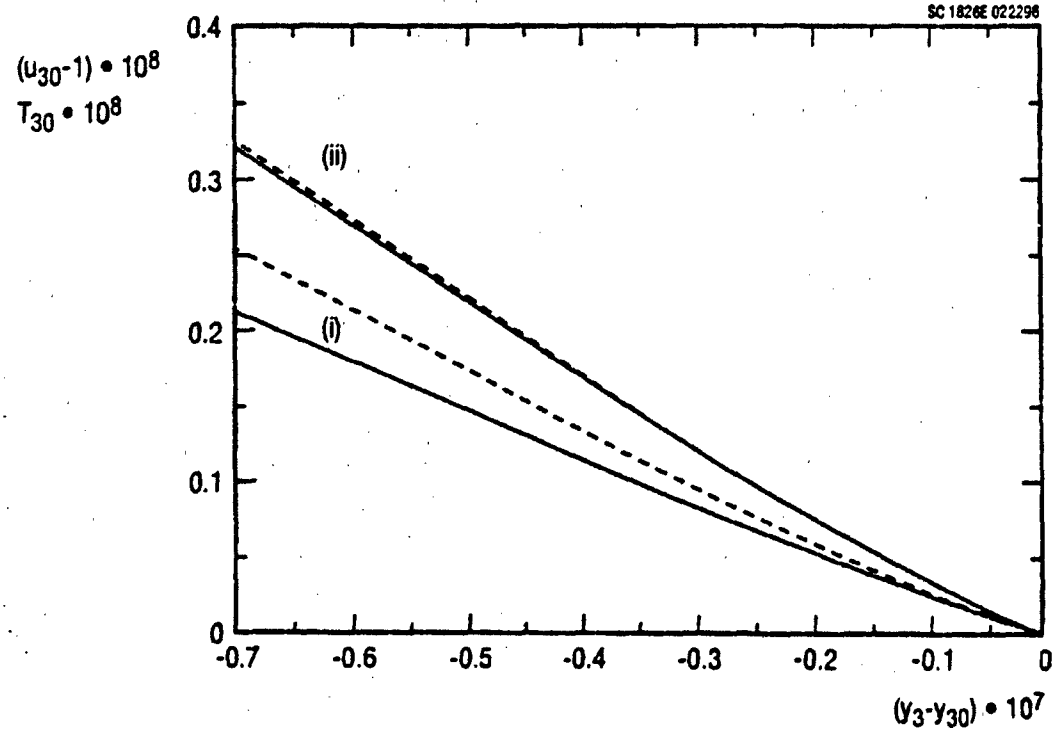

Fig. 10 Comparison of calculations of mean flow velocity and temperature with asymptotics near boundary layer edge. (solid: calculation;dashed: asymptotics). (i): $((u_{30}-1)\cdot 10^8$;(ii) $T_{30}\cdot 10^8$ vs. $(y_3-y_{30})\cdot 10^7$.

boundary layer edge and comparison with the asymptotics (A.5) are shown in Fig.10 in an enlarged scale. Note that in agreement with the [2] the velocity approaches unity from above (Const$_1$>0) so that there is a local maximum of the latter within the boundary layer. Its position is extremely close to the upper edge

$$u_{30} - 1 \approx 1.07 \cdot 10^{-7} \text{ at } y_{30} - y_3 \approx 6.96 \cdot 10^{-6}$$

and is not resolved on the large-scale figure. The mean flow for helium exhibits the same qualitative behavior.

5. Unsteady Newtonian thin shock layers and hypersonic flow stability

5.1 Introduction

Although the stability of high speed flows has received much attention in the recent literature, major complicating aspects have not been treated in a unified way. These features include the combined effects of the finite shock displacement on the boundary layer, the nonparallelism of the flow and the vorticity introduced by the shock curvature. The relevant structure of the shock and boundary layers has been treated in [1]-[9]. In [6] and [7], the aforementioned stability issues were discussed within the Hypersonic Small Disturbance approximation for the inviscid deck strongly interacting with the hypersonic boundary layer. Equations of motion for the mean and fluctuating small amplitude flows were analyzed. Because of nonparallelism in this framework, the spatial part of the waves cannot be treated by the usual Fourier decomposition and an initial value rather than eigenproblem for spatial stability is obtained. The initial value problem leads to partial rather than ordinary differential equations that require a numerical marching method for their solution. Results indicate that the specific heat ratio γ plays a major role in the stability of flow since it controls the reflection of waves from the shock and the radiation of energy in the shock layer whose thickness scales with $\gamma - 1$.

Early experiments such as those described in [2] showed that for a practically interesting class of flows, the shock layer becomes very thin compared to the boundary layer near the nose of hypersonic flat plates. This feature and the desire to further understand the shock and boundary layer structure encourages the use of the Newtonian approximation $\gamma \to 1$. The connection with flow stability motivates the study of this approximation in an unsteady context. In this chapter, limit process expansions will be discussed relevant to unsteady viscous interactions as a prelude to the analysis of hypersonic stability and transition. The application of these limits is an unsteady extension of the steady state analysis of [3]. Although the focus here is the treatment of viscous interaction, boundary layer stability, receptivity and transition, the results derived are useful in inviscid hypersonic unsteady aerodynamic methodology and load prediction as well.

5.2 Analysis

Figure 1 schematically indicates strong interaction flow near the leading edge of a hypersonic body. The viscous boundary layer which is usually thin, occupies an appreciable fraction of the distance between the shock and body that will be considered without undue loss of generality a flat plate in what follows. Accordingly $F(\bar{x},\bar{t}) = 0$, in the notation of Fig. 1. The results in this chapter will be expressed in terms of the boundary layer thickness function $\Delta(\bar{x},\bar{t}) = 0$, which in the interpretation mentioned in the Introduction could be the body shape in an inviscid context.

The unsteady form of the Hypersonic Small Disturbance Theory (HSDT) equations [9] are applicable and are obtained as in [7] from limit process expansions of hatted variables defined as quantities normalized by their freestream counterparts, with ρ, T, u, v, μ the density, temperature, horizontal, vertical components of the velocity vector, and viscosity respectively. If the freestream density, pressure and velocity are denoted as U, p_∞ and ρ_∞ respectively, then a pressure coefficient used in these expansions is defined as $\tilde{p} = (p - p_\infty)/\rho_\infty U^2$.

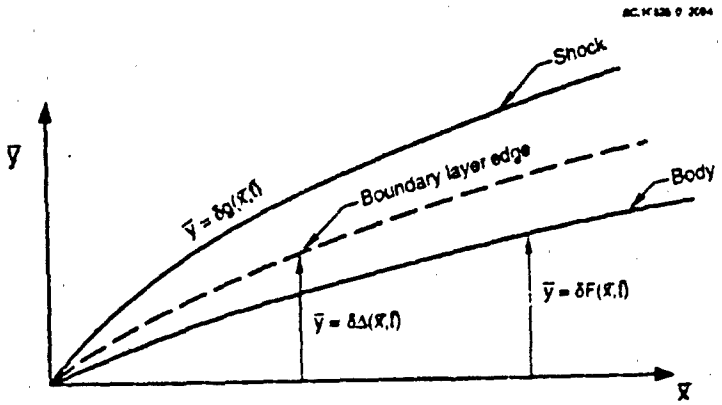

Fig. 1 Schematic of hypersonic strong interaction flow.

With these definitions and the coordinate system in Fig. 1 as well the normalization of the Cartesian dimensional coordinates $\bar{x}$ and $\bar{y}$ to the unit reference length L and the reference time scale L/U for the time $\bar{t}$, unbarred dimensionless normalized counterparts of these independent variables are defined. If M_∞ and R_∞ are respectively the freestream Mach and Reynolds numbers, and δ is a characteristic flow deflection angle, then the expansions are

$$\hat{\rho}(x, y, t; M_\infty, R_\infty, \gamma) = \sigma(x, y, t; H, \gamma) + \cdots \tag{1.1}$$

$$\hat{T} = T + \cdots \tag{1.2}$$

$$\tilde{p} = \delta^2 p + \cdots \tag{1.3}$$

$$\hat{u} = 1 + \cdots \tag{1.4}$$

$$\hat{\mu} = \mu + \cdots, \tag{1.5}$$

where $y = \bar{y}/(L\delta)$. These expansions are valid in the HSDT limit

$$x, y, t, H \equiv \frac{1}{M^2\delta^2} \text{ are fixed as } \delta \to 0,$$

where H is the hypersonic similarity parameter.

In [7] and elsewhere, *e.g.* [1], [8] it was shown that $\delta = \varepsilon^{1/6}$ where $\varepsilon \equiv Re^{-1} \to 0$ for strong interaction flows.

Substituting (1.1) - (1.6) into the Navier Stokes equations and shock conditions gives the following HSDT unsteady equations and boundary conditions:

$$\left(\frac{\partial}{\partial t}+\frac{\partial}{\partial x}\right)\sigma+\frac{\partial \sigma v}{\partial y}=0 \tag{1.8}$$

$$\left(\frac{\partial}{\partial t}+\frac{\partial}{\partial x}+v\frac{\partial}{\partial y}\right)v=-\frac{1}{\sigma}\frac{\partial p}{\partial y} \tag{1.9}$$

$$\left(\frac{\partial}{\partial t}+\frac{\partial}{\partial x}+v\frac{\partial}{\partial y}\right)\left(\frac{p+H/\gamma}{\sigma^{\gamma}}\right)=0. \tag{1.10}$$

In what follows, the boundary layer will regarded as an effective body, since in the strong interaction regime, the density of the flow approaches zero as the edge of the boundary layer is approached[8], [1], and [4] so that the latter is streamline in steady flow. In unsteady flow, it is plausible that it is a streakline. From Fig. 1, denoting the ordinate of this surface as $\bar{y} = \delta\Delta(\bar{x},\bar{t})$ then following [3] for steady flow, the body coordinates introduced for later use in the Newtonian limit are

$$y^* = y-\Delta(x,t) \tag{1.11}$$

$$v^* = v-v_e \tag{1.12}$$

$$v_e \equiv v(x,\Delta) = \Delta_x+\Delta_t \tag{1.13}$$

$$t^* = t \tag{1.14}$$

$$x^* = x \tag{1.15}$$

$$0 \le y^* \le G = g-\Delta. \tag{1.16}$$

The quantity v_e represents the vertical velocity component at the boundary layer edge. Equation (1.12) is derived from the property of this surface that it is a streakline. Representing this line in the implicit form $B(\bar{x},\bar{y},\bar{t}) = 0$, where

$$B = y-\Delta(x,t) = 0, \tag{1.17}$$

the streakline property can be expressed as

$$B_t+\vec{q}\cdot\nabla B = 0, \tag{1.18}$$

where $\vec{q}$ denotes the flow velocity vector. Substitution for $\vec{q}$ (1.4) and (1.5) into (1.18) gives (1.12).

Defining the convective operators as

$$D \equiv \frac{\partial}{\partial t^*} + \frac{\partial}{\partial x^*} \tag{1.19}$$

$$E \equiv \frac{\partial}{\partial t^*} + \frac{\partial}{\partial x^*} + v\frac{\partial}{\partial y^*} = \frac{\partial}{\partial t} + \frac{\partial}{\partial x} + v\frac{\partial}{\partial y}, \tag{1.20}$$

the HSDT equations written in these coordinates are

$$D\sigma + \left(\sigma v^*\right)_{y^*} = 0 \tag{1.21}$$

$$Ev^* + D^2\Delta = \sigma^{-1}p_{y^*}. \tag{1.22}$$

$$E\left(\frac{p + H/\gamma}{\sigma^\gamma}\right) = 0. \tag{1.23}$$

If subscript S denotes evaluation on the shock, the shock conditions in these coordinates are

$$v_S^* = \frac{2}{\gamma+1}\left[D(G+\Delta) - \frac{H}{D(G+\Delta)}\right] - D\Delta \tag{1.24}$$

$$p_S = \frac{2}{\gamma+1}\left[D(G+\Delta)^2 - H\right] \tag{1.25}$$

$$\sigma_S = \frac{\left[D(G+\Delta)\right]^2}{\frac{2}{\gamma+1} + \frac{\gamma-1}{\gamma+1}\left[D(G+\Delta)\right]^2}. \tag{1.26}$$

Recognizing that the shock layer is $O(\gamma - 1)$ as $\gamma \to 1$, and $H \to \infty$, even in the unsteady case, the following Newtonian limit process and expansions are used:

$$N \equiv \frac{H}{\lambda}, t^*, x^*, \tilde{y} \equiv \frac{y^*}{\lambda} \text{ are fixed as } \lambda \equiv \frac{\gamma-1}{\gamma+1} \to 0 \tag{1.27}$$

$$p(x^*, y^*, t^*) = \tilde{p}(x^*, \tilde{y}, t^*) + \cdots \tag{1.28}$$

$$\sigma = \frac{1}{\lambda}\tilde{\sigma} + \cdots \tag{1.29}$$

$$v = \lambda\tilde{v} + \cdots \tag{1.30}$$

$$g(x^*, y^*) = \Delta(x^*, t^*) + \lambda\tilde{g}(x^*, t^*) + \cdots, \tag{1.31}$$

where N is the Newtonian similarity parameter.

Substitution of (1.28) - (1.31) into (1.21) - (1.23) and (1.24) - (1.25) as well as retaining like orders gives the following unsteady Newtonian equations and shock conditions:

$$\tilde{E}\tilde{\sigma} + \tilde{\sigma}\tilde{v}_{\tilde{y}} = 0 \tag{1.32}$$

$$\tilde{E} \equiv D + \tilde{v}\frac{\partial}{\partial \tilde{y}} \tag{1.33}$$

$$D^2\Delta + \frac{1}{\tilde{\sigma}}\tilde{p}_{\tilde{y}} = 0 \tag{1.34}$$

$$\tilde{E}\left(\frac{\tilde{p}}{\tilde{\sigma}}\right) = 0. \tag{1.35}$$

On the shock,

$$\tilde{v}_s \equiv \tilde{v}(x, g(x,t), t) = D\tilde{g} - \frac{N}{D\Delta} - D\Delta \tag{1.36}$$

$$\tilde{p}_s = (D\Delta)^2 \tag{1.37}$$

$$\tilde{\sigma}_s = \frac{(D\Delta)^2}{N + (D\Delta)^2}. \tag{1.38}$$

Eq. (1.12) implies the tangency relation

$$\tilde{v}(x^*, 0, t^*) = 0. \tag{1.39}$$

The initial boundary value problem comprised by (1.32)-(1.35), (1.36)-(1.38) and (1.39) can be simplified by an unsteady extension of the Von Mises transformation. Introducing an unsteady stream function ψ

$$\psi_{\tilde{y}} = \tilde{\sigma}, \quad -D\psi = \tilde{\sigma}\tilde{v}, \tag{1.40}$$

an unsteady extension of the Von Mises mapping is considered in which

$$(x^*, \tilde{y}, t^*) \rightarrow (\xi, \eta, \psi). \tag{1.41}$$

with characteristic coordinates defined as

$$\xi = \frac{x^* + t^*}{2}, \quad \eta = \frac{x^* - t^*}{2}, \tag{1.42}$$

the differential operators map as follows:

$$D = \frac{\partial}{\partial \xi}, \frac{\partial}{\partial \bar{y}} = \bar{\sigma} \frac{\partial}{\partial \psi}. \tag{1.43}$$

In characteristic coordinates, the convective operator $\tilde{E}$ is expressed as

$$\tilde{E} = \frac{\partial}{\partial \xi} - \bar{\sigma} \bar{v} \frac{\partial}{\partial \bar{y}}. \tag{1.44}$$

For $\xi = 0$,

$$\tilde{E} = \frac{\partial}{\partial \xi}. \tag{1.45}$$

In this coordinate system, the Newtonian shock layer equations and shock conditions become

$$\left(\frac{1}{\bar{\sigma}}\right)_{\xi} = \bar{v}_{\psi} \tag{1.46}$$

$$\bar{v}_{\epsilon_{\psi}} + \bar{p}_{\psi} = 0 \tag{1.47}$$

$$\bar{v}_{\epsilon} = \Delta_{\xi} \tag{1.48}$$

$$\frac{\bar{p}}{\bar{\sigma}} = K(x^* - t^*, \psi) \tag{1.49}$$

$$\bar{v}_s = D\bar{g} - \frac{N}{\bar{v}_{\epsilon}} - \bar{v}_{\epsilon} \tag{1.50}$$

$$\bar{p}_s = \bar{v}_{\epsilon}^2 \tag{1.51}$$

$$\bar{\sigma}_s = \frac{\bar{v}_{\epsilon}^2}{N + \bar{v}_{\epsilon}^2}. \tag{1.52}$$

The solution integral given by (1.49) can be interpreted as plane entropy waves convecting downstream at the freestream speed. If the initial state is

$$K(x^*, 0, \psi) = f(x^*, \psi), \tag{1.53}$$

then at any time t^*,

$$K(x^*, t^*, \psi) = f(x^* - t^*, \psi). \tag{1.54}$$

To match the shock and boundary layers, an "interaction law" relating the pressure and normal velocity at the boundary layer edge is required. This matching was studied by Lees [5], Stewartson [8], Bush [1], as well as Lee and Cheng [4] for steady flow. The unsteady case has apparently not been analyzed. The interaction law can be obtained from integration with respect to ψ of (1.47) which gives

$$\tilde{p} = -\tilde{v}_{e_\xi}\psi + \tilde{p}_e , \tag{1.55}$$

where $\tilde{p}_e = \tilde{p}(x^*,t^*,0)$ is the pressure at the boundary layer edge. The quantity ψ_s can be obtained from the second member of (1.43) specialized to the shock value of the stream function ψ_s, and the shock relations (1.50) - (1.52). An integration with the assumption that the shock intersects the boundary layer and body at the nose gives

$$\psi_s = \Delta \tag{1.56}$$

Evaluating (1.55) on the shock gives an unsteady extension of the Newton-Busemann pressure formula. This interaction law is

$$\tilde{p}_e = (D\Delta)^2 + \Delta D^2\Delta . \tag{1.57}$$

Evaluation of K at the shock gives

$$\frac{\tilde{p}_s}{\tilde{\sigma}_s} = N + (D\Delta)^2 = K(x^* - t^*, \psi_s) . \tag{1.58}$$

which with (1.56) gives a pair of relations which parametrically defines the spatial entropy distribution at each time instant along the various instantaneous streamlines. The mapping $y \rightarrow \psi$ is obtained from the first member of (1.43), as well as (1.53), (1.55), and an integration as

$$\tilde{y} = \int_0^{\psi} \frac{K(x^* - t^*, \psi')}{\tilde{p}_e - \psi' D^2\Delta} d\psi' \equiv I(t^*, x^*, \psi) . \tag{1.59}$$

Evaluating (1.59) at ψ_s gives the shock shape

$$\tilde{g}(x^*,t^*) = I(x^*,t^*,\Delta) . \tag{1.60}$$

The density is obtained from the entropy integral (1.53) and (1.55) as

$$\tilde{\sigma} = \frac{\tilde{p}}{K(x^* - t^*, \psi)} . \tag{1.61}$$

Writing $K(x^* - t^*, \psi) \equiv Q(\eta, \psi)$, the vertical velocity is derived from (1.55), the boundary condition (1.39), and integration of (1.46). This gives

$$\tilde{v} = \int_0^{\psi} \frac{\partial}{\partial \xi} \left[\frac{Q(\eta, \psi')}{\tilde{p}_e - \tilde{v}_{e_\xi}\psi'} \right] d\psi' . \tag{1.62}$$

From the aforementioned attachment of the shock to the body leading edge property implied for continuum flow, evaluation of K at the nose $x = 0$ and the shock relations (1.50)-(1.52) give the density on the boundary layer edge to be

$$\tilde{\sigma} = \frac{\Delta D^2 + (D\Delta)^2}{N + (D\Delta)^2_{x=0}}. \tag{1.63}$$

5.3 Computations and results

The mapping $\tilde{y} \to \psi$ given by (1.59), can be expressed in explicit form convenient for numerical calculations. Introducing independent variables $x = x^*$ and $s = x^* - t^*$ gives

$$d\psi(s = \text{const.}) = \frac{\partial \psi_s}{\partial x} dx + \frac{\partial \psi_s}{\partial t^*} dt^* = D\Delta(x, x - s)dx. \tag{2.1}$$

Substituting (2.1) into (1.59) and accounting for (1.55) and (1.58), gives

$$\tilde{y} = \int_0^x \frac{\left[\Delta_1^2(x_1, t + x_1 - x) + N\right]\Delta_1(x_1, t + x_1 - x)}{\Delta_1^2(x,t) - \left[\Delta_1(x_1, t + x_1 - x) - \Delta(x,t)\right]\Delta_2(x,t)} dx_1 \tag{2.2}$$

$$\psi = \Delta(x_1, x_1 + t - x) \tag{2.3}$$

$$\Delta_1(x,t) \equiv D\Delta(x,t), \Delta_2(x,t) = D^2(x,t). \tag{2.4}$$

The flow temperature T, pressure p, and density σ at the point $(x, \tilde{y})$ and the time t are

$$\tilde{T} = \Delta_1^2(x_1, x_1 + t - x) + N \tag{2.5}$$

$$\tilde{p} = \tilde{p}_e(x,t) - \Delta_2(x,t)\psi \tag{2.6}$$

$$\tilde{\sigma} = \tilde{p}/\tilde{T}. \tag{2.7}$$

The shock deviation is evaluated by the integral (2.2) at the upper limit of integration x. Equations (2.2) and (2.3) indicate that the stream function ψ and the temperature T at the point $(x, \tilde{y})$ correspond to those just behind the shock at the cross section x_1 where $y = \tilde{g}(x_1, t)$.

If the boundary layer edge $\Delta(x,t)$ is known function, an unsteady flow field within shock layer can be easily calculated using Eqs. (2.2) and (2.5). As an example, consider the case when the boundary layer thickness δ_b is much less the body thickness. Then

$$\Delta(x,t) = F(x,t) + O(\theta), \theta = \delta_b/\delta \to 0. \tag{2.8}$$

Unsteady perturbations produced by the body surface in the zeroth-order approximation with respect to the small parameter θ, will be considered. Features of the flow field will be discussed for the body shape examples

$$\Delta = x + Axe^{-(x-x_0)^2}\cos(\omega t) \tag{2.9}$$

$$\Delta = x + A\frac{x}{x+x_0}\sin(\alpha x - \omega t)\,. \tag{2.10}$$

Shape (2.9) describes a wedge of a half-angle δ with a 2-D hump placed at a distance x_0 from the leading edge and oscillating with frequency ω and amplitude A. Shape (2.10) describes a wedge with a superposed traveling wave modulation starting near the point x_0 and propagating downstream with phase velocity $c = \omega/\alpha$; the wave amplitude achieves the constant value A as $x \to \infty$.

Figures 2a and 2b illustrate a flow field past the steady hump specified by Eq. (2.9) at x_0=1 with amplitude A=.15, for the Newtonian parameter N=0. For clarity in the plots, the temperature profile $\tilde{T}(\bar{y})$ at cross sections $x_k = (5/12)k, (k = 1,2,\ldots)$ are plotted with constant shift in the abscissae origins $\Delta\tilde{T}$ =0.5 corresponding to the different k. Figure 2a shows that the hump causes local shock perturbation damping in upstream and downstream directions. From Fig. 2b, it can be deduced that the curved portion of the shock induces a non-uniform temperature distribution across the shock layer which can be interpreted as an entropy wake convecting downstream along streamlines. If viscous dissipation is weak, the entropy wake is preserved in the far downstream flow field, although the shock and pressure perturbations are infinitesimal.

Similar data are shown in Figures 3a and 3b for the hump oscillating with the frequency ω=5 and the amplitude A=.02. The shock perturbation shape is close to that for the steady case having an instantaneous body surface of the same shape (*cf.* solid curves in Fig. 2a and Fig. 3a). Such a quasi-steady behavior is due to the infinitely large speed of pressure disturbance propagation across the shock layer according to Eq. (1.34). However, the temperature and density disturbances induced by the curved shock convect downstream at freestream speed (see Eqs. (1.32) and (1.34)). Because of the time lag and interference between entropy perturbations, the temperature profiles are quite different from those for the steady case (compare Fig. 2b and Fig. 3b). They oscillate across the shock layer, with decreasing wavelength as frequency increases.

In both steady and unsteady cases the temperature profiles have inflection points, that can generate an inviscid instability of the entropy wake for disturbances with short wavelength and high frequency, (see [10]). It is assumed that a steady or unsteady hump placed on the forebody of a hypersonic vehicle may be used as a boundary layer trip for the shock layer flow captured by the inlet. The inflectional entropy layer may amplify short-scale disturbances due to inherent instability mechanisms. Such amplification can be enhanced by interaction of disturbances with inlet shocks, (see [11], and [12]). Ultimately, this process may lead to formation of turbulent wakes. A similar effect might be caused by blowing/suction through the portion of the forebody surface. **It is conjectured that such instabilities and tripping mechanism described above can be useful for initiation or enhancement of hypersonic scramjet combustion processes.** Figures 4a and 4b illustrate flow field perturbations caused by the vibration wave of

Shape (2.10) for $\omega = 10, \alpha = 5$, $A = .01$ and $x_0 = 1$. It is evident that the shock deviation grows downstream and ultimately becomes a spike, consistent with the nonlinear nature of the disturbance evolution. Additionally, the temperature profiles are qualitatively similar to those over an unsteady hump (*cf.* Fig. 2b and Fig. 3b).

As shown in Fig. 5a, the amplitude of the shock vibration wave becomes infinite at a finite distance from the starting point x_0. The wall pressure is equal to zero (see Fig. 5b) at this location. Since this is a nonuniformity, the present asymptotic model is inadequate to describe the flow field near it. However, it is clear that the singular region is identified as a function of vibration wave characteristics. The vanishing wall pressure vanishing here can cause an inviscid separation from the body surface of the thin shock layer. This process resembles shock separation from the upper edge of hypersonic boundary layer on a flat plate at zero angle of attack (see [13] signifying that even small vibration waves propagating along the body surface can initiate a global reconstruction of the flow field.

5.4 Summary and conclusions

In this phase of the research, Newtonian thin shock layer theory was extended to unsteady flow. In earlier work for steady strong interaction flow, the boundary layer thickness $\Delta \sim x^{3/4}$ based on the similarity of the initial boundary value problem and integration of the boundary layer continuity equation. An integrodifferential equation for Δ arises that admits a similarity solution with the $x^{3/4}$ scaling. The literature assumes either a Tangent-Wedge or Newtonian impact theory interaction law for the pressure in these solutions. **From the present work, it appears that the proper asymptotically consistent procedure is to include the centrifugal term in this law (second term in the right hand side of the steady state version of (1.57)).**

Computations performed in a framework of the unsteady Newtonian thin shock layer theory reveals the following features of inviscid flow field:

- A local steady/unsteady hump induces steady/unsteady entropy perturbations propagating downstream with freestream velocity. It generates inflection points in the instantaneous shock layer profiles. According to inviscid stability theory, these profiles should be unstable with respect to short wavelength disturbances. Downstream amplification of inviscid instability may cause formation of turbulent wakes within a shock layer. It is plausible that such a tripping mechanism can be exploited in forebody-inlet design to initiate or enhance combustion process.

- Surface vibration waves of finite amplitude cause strong shock perturbations that grow downstream. These ultimately form spikes due to nonlinear effects. The infinite spike occurs at a finite distance from the initial vibration point. This singularity could lead to separation of a thin shock layer from the body surface and global reconstruction of the flow field within the shock layer.

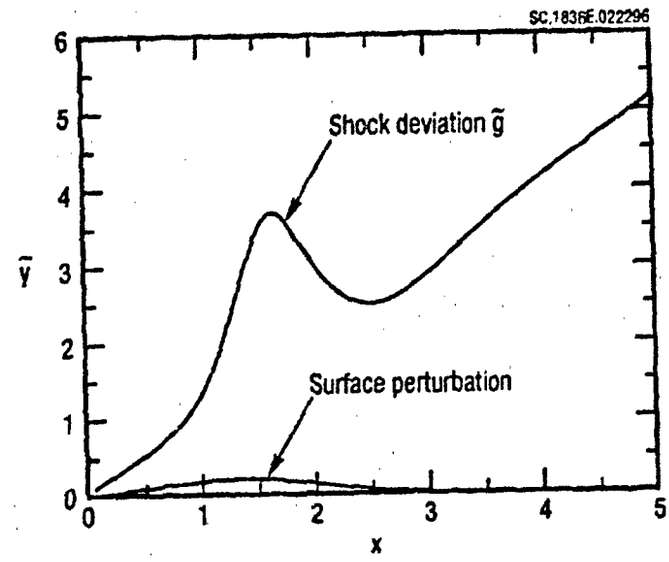

Fig. 2a. Shock deviations caused by steady bump, $A = .15$, $x_0 = 1, \omega = 0$, $N = 0$.

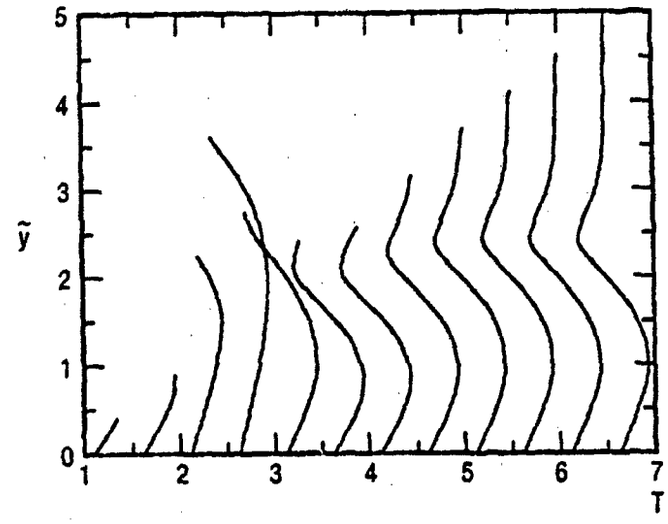

Fig. 2b Temperature deviations caused by steady bump, $A = .15$, $x_0 = 1, \omega = 0$, $N = 0$.

AD-A104 [illegible]

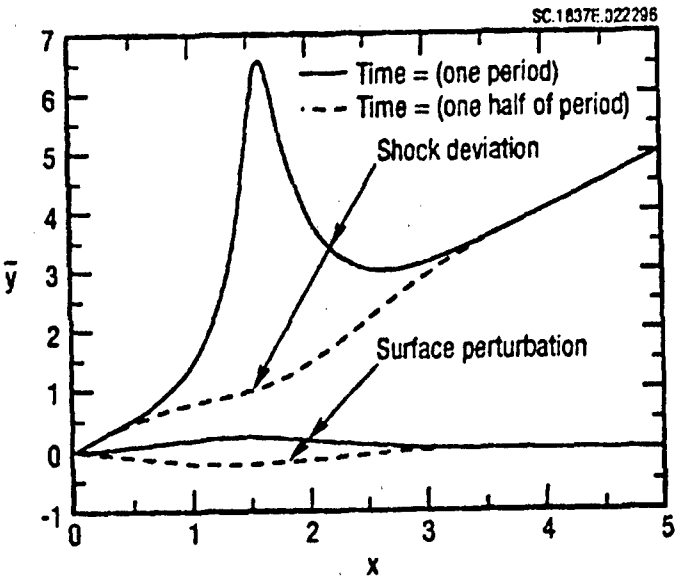

Fig. 3a. Shock deviations caused by unsteady bump, $A = .02$, $x_0 = 1, \omega = 5$, $N = 0$.

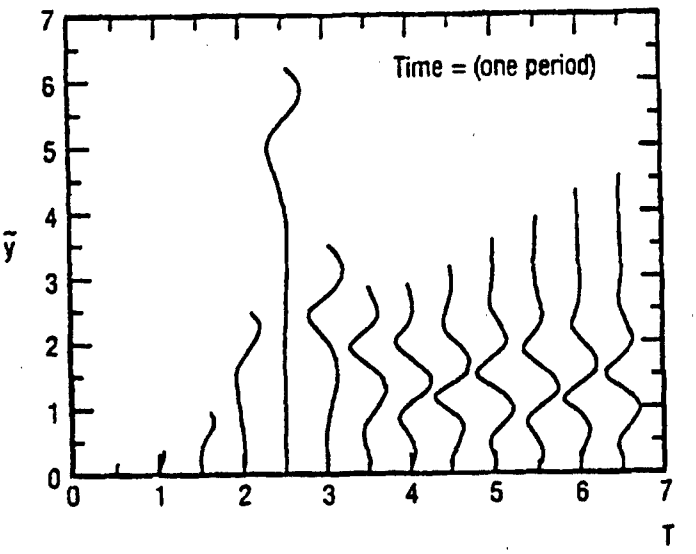

Fig. 3b Temperature deviations caused by unsteady bump, $A = .02$, $x_0 = 1, \omega = 5$, $N = 0$.

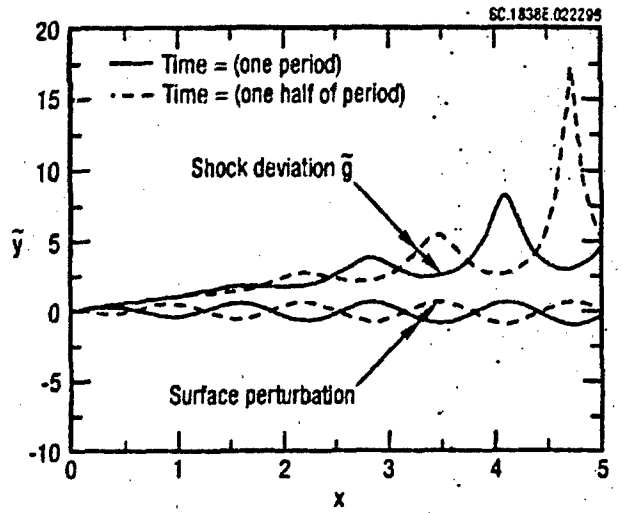

Fig. 4a. Shock deviations caused by traveling vibration wave, $A = .01$, $x_0 = 1, \omega = 10$, $N = 0, \alpha = 5$.

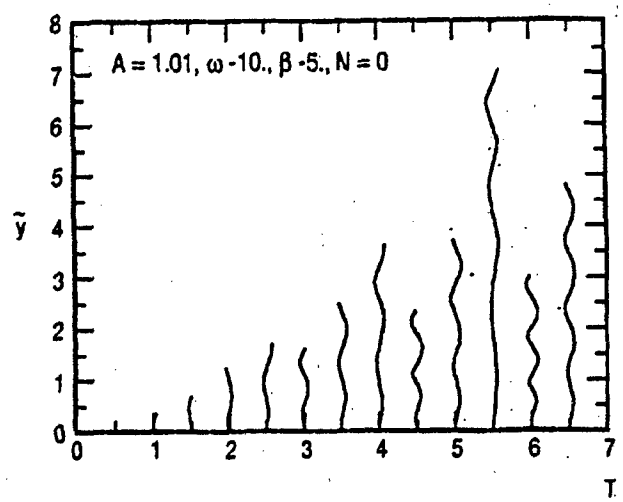

Fig. 4b. Temperature deviations caused by traveling vibration wave, $A = .01$, $x_0 = 1, \omega = 10$, $N = 0, \alpha = 5$.

AD-A216 403

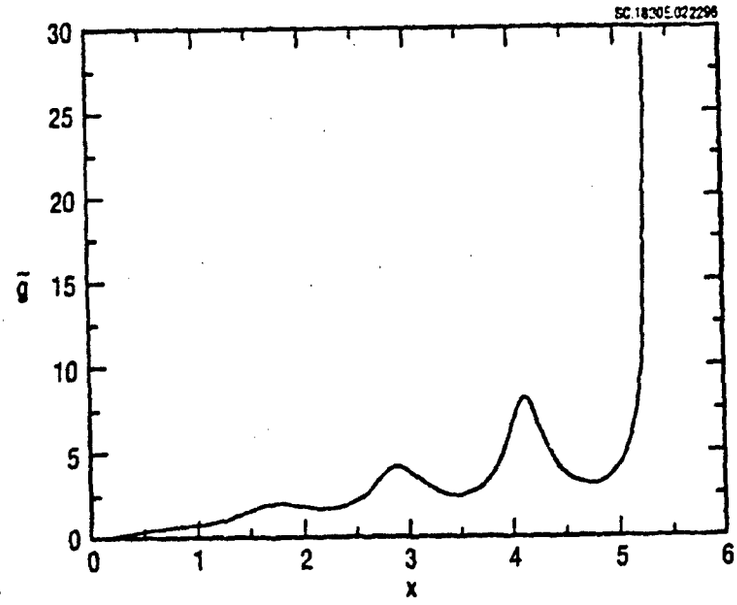

Fig. 5a. Shock deviations caused by traveling vibration wave, $A = .01, x_0 = .2, \omega = 5, N = 0, \alpha = 5.$

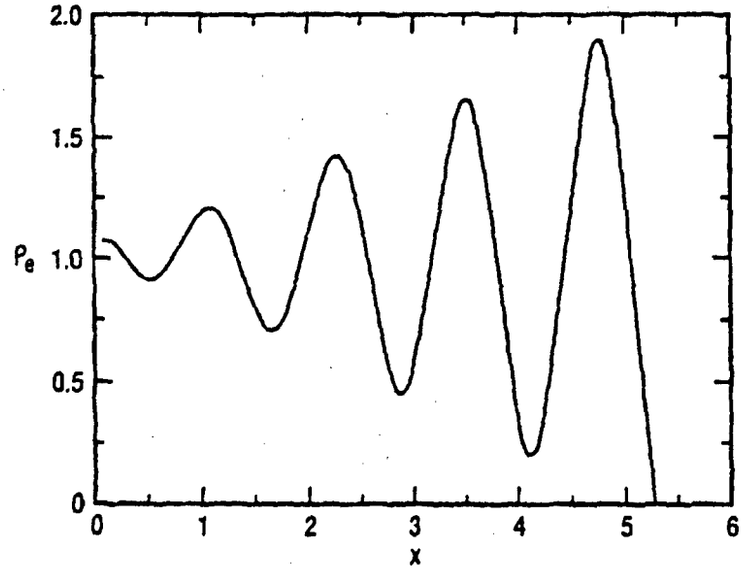

Fig. 5b. Temperature deviations caused by traveling vibration wave, $A = .01, x_0 = .2, \omega = 5, N = 0, \alpha = 5.$

5.5 References

1. Bush, W.B., "Hypersonic Strong Interaction Similarity Solutions for Flow Over a Flat Plate," *J. Fluid Mech.* **25** 1 , pp. 51 - 64, 1966.

2. Cheng, H.K., Hall, J.G., Golian, T.C., and Hertzberg, A., "Boundary Layer Displacement and Leading Edge Bluntness Effects in High-Temperature Hypersonic Flow," *J. Aerospace Sciences*, **28**, pp. 353 - 410, 1961.

3. Cole, J.D., "Newtonian Flow Over Slender Bodies," *J. Aero Sciences*, pp. 448 - 455 June, 1957.

4. Lee, R. and Cheng, H.K., "On the Outer Edge Problem of a Hypersonic Boundary Layer," *J. Fluid Mech* **38** 1, pp. 161 - 179, 1969.

5. Lees, L., "On the Boundary Layer Equations of Hypersonic Flow and Their Approximate Solutions," *J. Aero. Sciences* pp. 143 - 145 1953.

6. Malmuth, N.D., "Inviscid Instability of Hypersonic Strong Interaction Flow Over a Flat Plate," *Instability, Transition and Turbulence*, M.Y. Hussaini, A. Kumar, and C.L. Street, eds., Springer-Verlag, pp. 107 - 126, 1992.

7. Malmuth, N.D., "Stability of the Inviscid Shock Layer in Strong Interacion Flow Over a Hypersonic Flat Plate," in *Instabilities and Turbulence in Engineering Flows*, D.E. Ashpis, T.B. Gatski, and R. Hirsh, eds., Kluwer, pp. 189 - 224. 1993.

8. Stewartson, K., *The Theory of Laminar Boundary Layers in Compressible Flow*, Oxford, London, 1964.

9. Van Dyke, M.D., "A Study of Hypersonic Small Disturbance Theory," NACA TN 3173, May,1954.

10. Mack, L.M., "Boundary Layer Linear Stability Theory," AGARD Rep. No. 709, pp. 3/1 - 3/81,1984.

11. Anyiwo, J.C., and Bushnell, D.M.,"Turbulence Amplification in Shock Wave/Boundary Layer Interaction," *AIAA Journal* **20**, p. 893, 1982.

12. Meadows, K.R., Kumar, A., and Hussaini, M.Y., "A Computational Study on the Interaction Between a Vortex and a Shock Wave," *AIAA Journal* **29** p. 174, 1991.

13. Hayes, W.D., and Probstein, R.F., *Hypersonic Flow Theory*, Academic Press, N.Y, 1959.

6. Similarity Methods for Hypersonic Transition Prediction

6.1 Introduction

Prediction of laminar-turbulent transition in hypersonic boundary layers is of critical importance for aircraft and missile design [1]. Although considerable effort has been invested in developing theoretical and computational methods to predict high Mach number transition, a strong need still exists for approaches suitable for rapid response design application. To fill this need, empirical criteria based on wind tunnel and flight experiments are currently the main workhorses in engineering practice. Much of the difficulty in constructing a rapid design oriented method is due to the unique features of the hypersonic stability and transition problem that include strong non parallelism and shock effects. In spite of the success of e^N methods such as [2] below Mach 12, these aspects are significant at higher Mach numbers.

In this chapter, similarity methods will be used to indicate a potentially new useful procedure for preliminary design and fast tradeoff studies. These methods have the potential of dealing with some of these difficulties. The theoretical basis for the similarity method will be given and an application to hypersonic cones provided. Finally, possibilities for generalization of the method to more arbitrary shapes will be discussed.

Since the problem of disturbance evolution contains the large Mach and Reynolds number parameters, it is natural to use asymptotic methods in predictive models. Asymptotic theories of the vorticity mode as well as cross flow instability and Görtler vortices as well as [3] are recent examples. Solutions from this class of asymptotic models are limited in their applicability because of the restrictive asymptotic limit processes used. Other asymptotic approximations provide more general applicability but are also more difficult to solve. Even without solution however, such theories give important similarity groups, if appropriate normalizations and nondimensionalizations are used that reflect the salient phenomenological scales. These groups provide the basis for constructing similarity laws that not only can be useful for design of economical experiments, but prediction as well.

Such a procedure will be used in this paper to investigate similitude of boundary layer stability over nearly sharp, zero-incidence hypersonic cones. A similarity rule accounting for viscous and compressibility effects is derived without solving the initial boundary value problem. Predictions from the rule are compared with linear stability computations as well as (Reentry F) flight data obtained on slender cones [4]. It will be seen that this rule gives an extremely cost-effective and rapid extrapolation method of code or experimentally derived data to other conditions.

6.2 Similarity analysis

The unsteady disturbance field in a three-dimensional hypersonic boundary layer will be considered with the following assumptions: (i) The fluid is a perfect gas with constant Prandtl number Pr and specific heat ratio γ. Denoting starred quantities as dimensional, the viscosity-temperature law is $\mu^* = \mu_0^* T^{*\omega}$. (ii) The spatial scales of the disturbances are of the order of boundary layer displacement thickness δ^*; the time-scale is δ^* / U_e^*, where subscript e refers to the upper edge of the boundary layer. (iii) Boundary-layer disturbances weakly interact with the external inviscid flow and shock wave.

In the hypersonic boundary layer, the pressure is of the order of that of the external inviscid flow, and the temperature is of the order of the stagnation temperature $T_s^* \sim (\gamma-1)M_e^2 T_e^*$ This leads to asymptotic scaling for the flow variables within the boundary layer : The full Navier Stokes equations written in terms of this scaling contain only the lumped parameter $R = \varepsilon^{1+\omega} R$, where $\varepsilon \equiv \dfrac{1}{(\gamma-1)M_e^2} << 1$ and Re is the Reynolds number based on the displacement thickness= $Re = \delta^* U_e^* \rho_e^* / \mu_e^*$. The dependence on the similarity parameter R is valid for strong, moderate and weak viscous-inviscid interaction regimes. However, δ^* and, as a result, the Reynolds number Re, are sensitive to the interaction type. For example, the boundary layer on a flat plate has the displacement thickness $\delta^* \sim x^{*3/4}$ for strong interaction and $\delta^* \sim x^{*1/2}$ for a weak one.

Outside the boundary layer, the disturbances are assumed to vanish and weakly interact with the external inviscid flow . At the wall, the flow satisfies no-slip conditions, temperature is assumed to be constant. The upstream and downstream conditions as well as initial conditions for the disturbances are also assumed to depend weakly on Mach and Reynolds number. These additional provisions preserve the applicability of the R similitude previously indicated. It is therefore clear that the similarity law

$$f = fn(R, \gamma, T_f, Pr) \qquad (1)$$

holds, where f is any of the flow dependent variables, T_f is the wall temperature ratio, and fn signifies a functional dependence that can be obtained from solution of the initial value problem.

This similarity can be extended to the linear stability problem if a typical eigenmode wavelength, λ^* is of the order of the boundary layer thickness. If small disturbances are assumed in the original form of the Navier Stokes equations before the previously

mentioned rescaling is used, the general linearized equations (LSE) for small fluctuations are obtained. Within the spatial and temporal scaling implied by the wavelength assumption, the equations for the fluctuations depend again only on the parameters γ, T_f, Pr and R, if further, their initial and boundary conditions are consistent with this assumption. Therefore, the fluctuations obey a similarity law such as (1).

As an example, consider the two-dimensional vorticity mode (second mode according to Mack's classification [5]) in the boundary layer on a flat plate or sharp cone. In this case, the span component of the wave vector, $\beta = 0$ and the growth rate $\sigma = -\mathrm{Im}(\alpha)$ (α =the complex eigenvalue). If the Prandtl number, specific heat ratio and viscosity exponent parameters Pr, γ, ω, as well as the wall temperature factor $T_f = \frac{T_w^*}{T_{ad}^*}$ are fixed, where T_w^* is the wall temperature, T_{ad}^* is the adiabatic wall temperature, the maximum growth rate $\sigma(\Omega)$, ($\Omega = \Omega^* \delta^* / U_e^*$ the non dimensional frequency) is a function of Reynolds number Re and Mach number M_e.

In Fig. 1, calculations for σ_m from a linear stability code are shown as a function of the similarity parameter R at $M_e = 7$, 8, 10, 12 and 14. The following parameters were used in the computations: $Pr = 0.72$, $\gamma = 1.4$, $T_f = 0.2$ and $\omega = 0.75$. The stability characteristics have been computed by solving the eigenproblem for the LSE system of equations [5]. In this procedure, the mean flow in the boundary layer was approximated by the hypersonic weak interaction theory self-similar solution. Note that the similarity given by (1) collapses the $\sigma_m(Re, M_e)$ curves to $\sigma_m(R)$ at moderate values of R, as Mach number increases. At sufficiently large R, the curves tend to spread, because the wavelength of the vorticity mode $\lambda^* \ll \delta^*$ and Assumption (ii) is violated. This is consistent with the asymptotic theory for inviscid disturbances according to which the vorticity mode is concentrated in a thin transitional layer at the upper edge of the boundary layer. However, the region where similarity works well is sufficiently wide and relates well to practical applications.

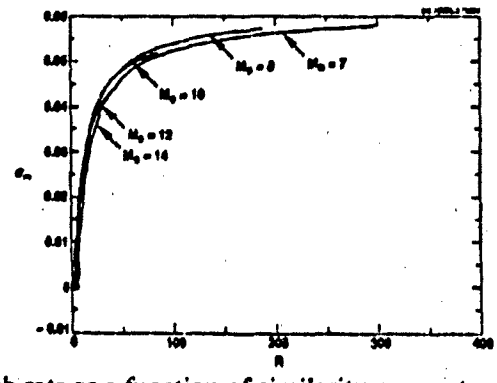

Fig. 1 Maximum growth rate as a function of similarity parameter R at various local Mach numbers M_e.

6.3 Application of similarity in hypersonic transition prediction

Hypersonic cones are used as a focus to explore the use of similarity in transition prediction herein. Reference [4] provides transition data for a slender cone at freestream Mach number 20 during reentry from altitudes of approximately 30.480 to 18.288 km, corresponding to the region of freestream Reynolds number 6.56 to 52.5 x 10^6 per meter. Experimental points representing transition onset Reynolds numbers $Re_{x,tr} = U_e^* x_{tr}^* / \nu_e^*$, ($\nu_e^*$= kinematic viscosity) as a function of local Mach number M_e are shown by the symbols in Fig. 2 In the figure, I denotes the sharp cone, II signifies entropy layer swallowing by the boundary layer close to the transition location and III represents swallowing downstream of transition. The similarity relation (1) applies for Regimes I and III.

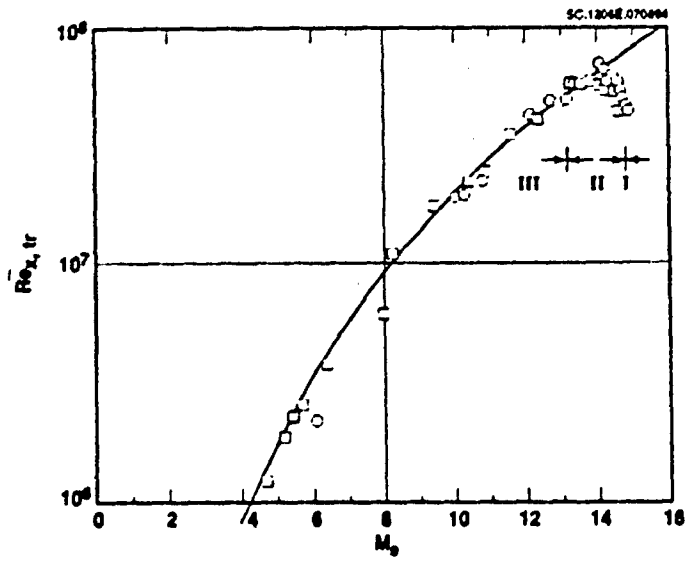

Fig. 2 Comparison of present theory with flight experiment. Solid line: theory, symbols: experiment.

Because of recession of the nose tip during reentry, the local Mach number at the upper edge of the boundary layer depends on the nose-radius history. The maximum M_e corresponds to a sharp nose. As the tip is blunted, the boundary layer grows in a higher entropy gas with smaller local Mach number. The transition Reynolds number depends on the location of the region where the entropy layer is swallowed by the boundary layer. More details are given in Ref. [6] of how this physics is related to the change in the monotonic trend of the Regime III data shown in Fig. 2 . For Regime II, only *local*

similarity rather than the *global* similarity (1) is valid that is associated with almost constant boundary layer edge flow quantities. The latter corresponds to sharp cone similitude at a given local Mach number. For this case, the flat plate mean flow viscous interaction parameter $\chi \equiv (\gamma-1)M_e^3\sqrt{Re_x}$, $(Re_x \equiv U_e^* x^*/\nu_e^*)$, derived in Ref. [7] is related to transition onset. The assumption of weak interaction $\chi << 1$ is well satisfied by experimental data of [4]. From [7], and application of the Blasius formula locally, the boundary-layer displacement thickness δ^*, local Reynolds number Re and similarity parameter, R are

$$\delta^* = \varepsilon^{\frac{1+\omega}{2}} \Delta \sqrt{\mu_e^* x^* / \rho_e^* U_e^*}, \tag{2}$$

$$Re = \Delta \varepsilon^{\frac{1+\omega}{2}} \sqrt{Re_x}, \tag{3}$$

using the perfect gas law, energy invariant, and the previously stated viscosity-temperature law, where $\Delta \equiv$ the constant of proportionality in this law.

In (2) and (3), Δ is a weak function of M_e. In the hypersonic limit, Δ is assumed independent of M_e. This approximation simplifies the prediction of the transition onset location that can be estimated by the e^N method. The amplification factor N for the two-dimensional second mode can be represented solely as a function of the similarity parameter R as

$$N(\Omega, x^*) \equiv \int_{x_0^*}^{x^*} \sigma^* dx^* = \frac{2}{\Delta^2} \int_{R_0}^{R} \sigma \, dR,$$

where $\sigma^* = \sigma\delta^*$. Applying the transition onset criterion $N = N_{cr}$, where N_{cr} is the critical amplification factor that is assumed to be a constant for Regime III data from [4], the corresponding similarity parameter R_{tr} can be obtained. According to (3), $Re_{x,tr} = \varepsilon^{-(1+\omega)} \Delta^{-2} R_{tr}^2$. Since N_{cr} =const independent of Mach number M_e and from $N = N_{cr}(R)$, R_{tr} also =const, independent of Mach number M_e. Therefore, the similarity rule

$$\frac{(Re_{x,tr})_1}{(Re_{x,tr})_2} = \left(\frac{M_{e1}}{M_{e2}} \right)^{2(\omega+1)} \tag{4}$$

is obtained on use of the definition of ε and the fact that the other parameters are fixed.

Equation (4), shown in Fig. 2 as a solid line for $\omega = 0.75$, agrees excellently with flight data and provides a useful prediction tool that can be applied for other zero incidence cones. With (4), characteristics at new Mach numbers can be obtained from computed or experimental points corresponding to a particular cone geometry and wall-to-freestream temperature ratio.

6.4 Discussion, future work and conclusions

Effort is in progress to extend the applicability of the similarity method to more general shapes than cones and treat angle of attack cases. In this connection, it should be noted that similarity gives a relation between the local characteristics of the boundary layer. The simple form of the similarity rule (4) was obtained under the assumption that the mean flow parameters at the boundary-layer edge are constant. Similarity appears also to be valid for transition due to some local process that is typical of nonlinear by-pass mechanisms. If transition depends on the disturbance streamwise history and the mean flow has a non uniform distribution in the x, z plane, similarity can be used to relate disturbance characteristics between two streamwise stations and account for the global process leading to transition. From the e^N method, the growth rate σ can be extrapolated to the new set of conditions at each point using similitude. This can be used to determine the amplification rate N to predict the transition Reynolds number. Since this approach would be derived under the other general conditions used here it would not only be applicable for more complicated geometries but linear and nonlinear regimes as well.

6.5 References

1. Malik, M., Zang, T., and Bushnell, D., "Boundary Layer Transition in Hypersonic Flows," AIAA Paper No. 90-5232, 1990.

2. Fedorov, A.V., Gushchin, V.R., and Tumin, A.M., "Transition to Turbulence on Hypersonic Vehicles," *Proc. ASME Fluid Engineering Conf.*, Washington, D.C., June 20–24, 1993; FED-Vol. 155, *Turbulent Flows—1993*, pp. 55–58.

3. Malmuth, N.D., "Stability of the Inviscid Shock Layer in Strong Interaction Flow Over a Hypersonic Flate Plate," *Instabilities and Turbulence in Engineering Flows, Fluid Mechanics and Its Applications Series*, Kluwer Press, Dordrecht, 1993, pp. 189–223.

4. Wright, R.L., and Zoby, E.V., "Flight Boundary Layer Transition Measurements on a Slender Cone at Mach 20," *AIAA Paper No. 77-719*, 1977.

5. Mack, L.M., "Boundary Layer Stability Theory," Jet Prop. Lab., Doc. 900-277, Rev. A, Pasadena, 1969.

6. Fedorov, A. and Malmuth, N., "Analysis of Similarity Methods in Hypersonic Transition Prediction," Rockwell International Science Center Report, RISC94NM2, August, 1994.

7. Hayes, W.D. and Probstein, R.F., *Hypersonic Flow Theory*, Academic Press, N.Y., 1959.

7. Transonic Wind Tunnel Wall Interference

7.1 Introduction

A central problem in aerodynamics is prediction of vehicle flight characteristics from wind tunnel tests of subscale models. Major factors in extrapolating the tunnel results to free flight are Reynolds number scaling as well as wall and sting interference. Currently, the issue of U.S. wind tunnel modernization is being addressed. A major thrust is attainment of near-flight Reynolds numbers. If large models are used, wall and sting interference are limiting factors in obtaining a tunnel flow even qualitatively resembling that of flight. In particular, testing at transonic speeds can produce steep wave fronts that reflect back on the model. Porous and other types of ventilated walls have been developed with the aim of canceling these reflections. In spite of the advances made in this technology as well as computational simulations, much still needs to be done to understand the tradeoffs in sizing wind tunnel models and test sections to minimize wall and sting effects while maximizing model Reynolds numbers.

References [1]-[3] exemplify early treatments of lifting flat plate wings in porous tunnels at subsonic speeds. This work did not address important nonlinearities associated with the transonic regime and assumed small wing dimensions compared to that of the test section. No framework was developed for systematic improvement of the approximation, and to our knowledge, the results were not compared with experiment. Computational treatments of transonic flows are discussed in [4]-[6] which remedy some of these deficiencies and deal with realistic airplane shapes. The large scale (CFD) computational approach can model geometric complexity and nonlinear effects but is usually expensive and time-consuming. Although considerable progress has been made, much user intervention is still required for geometric pre-processing to mate structured and even unstructured grids to the 3-D surface topology. This is an important issue for the test engineer who needs to quickly size the model, make test plan adjustments during the test and interpret the results afterwards. Combined asymptotic and computational (CAN) methods are discussed in [7] and [8] that address this need.

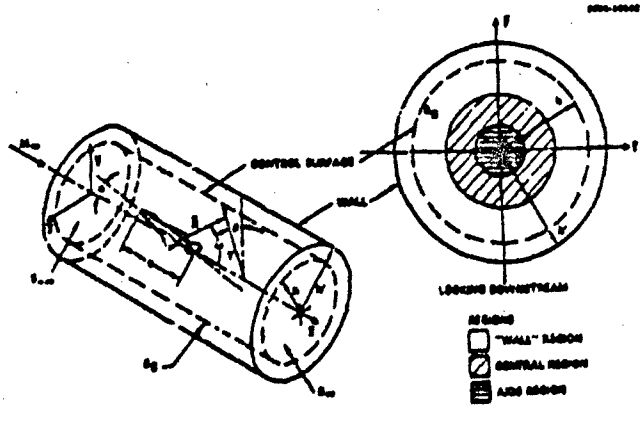

Fig. 1 Schematic of confined slender airplane.

These approaches reduce the size and computational intensity of the nonlinear problem and provide frameworks for approximation procedures that are capable of systematic refinement

As examples of the CAN approaches, [7] and [8] discuss transonic blockage interference for confined slender shapes such as those shown schematically in Fig. 1 and lift interference for high aspect ratio wings.

In this section, improvements of our previous theories will be discussed in four major areas delineated in the contract Statement of Work (SOW). These are:

1. Treatment of lift interference

2. Extension of large wall-height blockage interference to moderate height case

3. Porous wall effects

4. Non-circular wind tunnel test sections

7.2 Lift interference and porous wall effects

The thrust of this activity is to develop a systematic asymptotic framework for computation of lift corrections due to the interaction of a slender model with walls. Because of the resemblance of the asymptotic developments, to those for transonic flow, the subsonic case was considered for convenience. As indicated later, this approach actually seemed to provide good comparison with experiment at near-sonic speeds. The treatment was general enough to address Item 3.

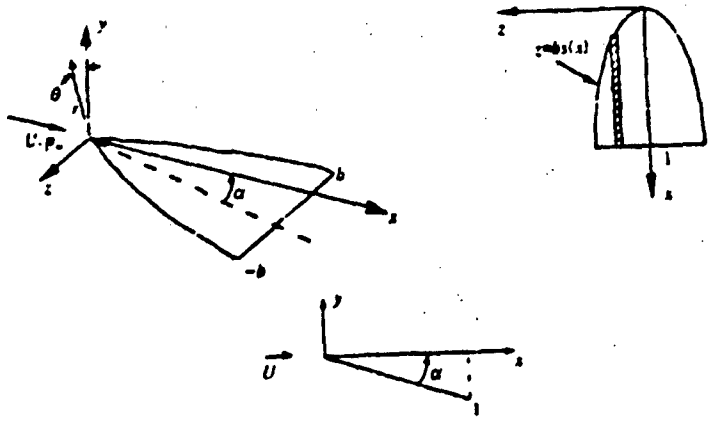

Fig. 2 Schematic of slender wing.

Initial developments under this contract are described in [9]. There, the free field and wind tunnel problem of the incompressible flow over a flat wing of arbitrary planform in a circular wind tunnel test section was outlined. An in-depth continuation of that introductory treatment will be summarized in what follows,. Expansions of limit process type have been used to the study the matching process in greater detail than in the preliminary analysis of [9]. In addition, the second order inner approximation has now been derived.

Letting Φ be the velocity potential, limits involving the semispan of the wing b and the angle attack α have been considered. Near the wing, a limit process in which $b \to 0$ is used. Referring to Fig. 2, an inner limit is defined as

$$\frac{\Phi_{inner}}{U} = x + ab\varphi_1(x, y^*, z^*) + ab^3 \log\frac{1}{b}\varphi_{21}(x, y^*, z^*) + ab^3\varphi_2 + \cdots \tag{1}$$

where the inner limit is

$$a = \tan\alpha,\ A = \alpha / b,\ y^* \equiv y / b,\ z^* \equiv z / b, \text{ fixed as } a, b \to 0 \tag{2}$$

In (2), the characteristic wing chord is fixed while the semispan b and angle of attack α tend to zero at the same rate. Near the wing, cross flow gradients dominate and these parameters give the characteristic lateral scale of the flow which is b. Equation (1) is an inner expansion for the velocity potential Φ in terms of approximating perturbation potentials φ_ν, (ν = order of the approximation). It contains the "switchback" term φ_{21} and the indicated gauge functions in anticipation of matching.

The problems for the φ_ν are obtained by substituting the asymptotic developments into the exact problem for Φ. For this exact problem, the equation of motion for the velocity potential is

$$\nabla^2\Phi = 0. \tag{3}$$

Bernoulli's Equation is

$$\frac{\rho q^2}{2} + P = \frac{\rho U^2}{2} + P_\infty. \tag{4}$$

The equation of the body is

$$B = y + ax = 0. \tag{5}$$

On this surface, the tangency boundary condition is

$$\vec{q}\cdot\nabla B = 0. \tag{6}$$

Darcy's law

$$\Delta P \sim RV, \tag{7}$$

is used to model the porous walls, where,

ΔP = Pressure difference across wall

R = Flow resistance constant

V = Transverse velocity.

The dominant orders in (1) solve harmonic boundary value problems in the cross plane perpendicular to the freestream and the higher orders solve Poisson problems. In particular, substitution of the inner expansion into the exact problem, gives the following problems:

$$\left.\begin{aligned} &\Delta_T^* \varphi_1 \equiv \varphi_{1y^*y^*} + \varphi_{1z^*z^*} \\ &\varphi_{1\bar{y}}(x,-Ax,z^*) = -1 \end{aligned}\right\} \tag{8a}$$

$$\left.\begin{aligned} &\Delta_T^* \varphi_{12} = 0 \\ &\varphi_{12_{y^*}}(x,-Ax,z^*) = 0 \end{aligned}\right\} \tag{8b}$$

$$\left.\begin{aligned} &\Delta_T^* \varphi_2 = -\varphi_{1_{xx}} \\ &\varphi_{2_{y^*}}(x,-Ax,z^*) = -\varphi_{1_x}(x,-Ax,z^*) \end{aligned}\right\} \tag{8c}$$

Problems (8) require far field boundary conditions for $r^* \equiv \sqrt{y^{*2} + z^{*2}} \to \infty$. These come from matching.

The dominant inner approximation from (8a) provides a first estimate for the flow and pressure field of the wing. The leading edge square root singularities dominate this flow field which is the stagnating flow on a finite flat plate. From a Joukowski mapping to the circle plane or the Circle Theorem, the solution of the problem (8a) is

$$\varphi_1 = -i\,\mathrm{Re}\left\{\left[\sigma^2 - s^2\right]^{1/2} - \sigma\right\} \quad \sigma \equiv z^* + i(y^* + Ax) \tag{9}$$

in which the freestream velocity has been normalized to unity through the non-dimensionalizations in (1). This solution has the proper far field (downwash at infinity) related to matching with outer solution.

A similar procedure gives the following for solution for φ_{12} which is

$$\varphi_{21} = -\,\mathrm{Re}\frac{i}{2}(ss')'\sqrt{\sigma^2 - s^2}\,. \tag{10}$$

This satisfies the surface boundary condition in (8b).

The far field for φ_2 as $r \to \infty$ is also needed for the matching. This can be obtained from particular solutions of the Poisson equation in (8c). This gives

$$\varphi_2 \equiv -\frac{1}{2}(ss')'(r^*\cos\theta)\log r^* + h_2(x)y^* + \cdots \text{ as } r \to \infty.$$

Refinements of the unconfined flow field and wall interactions come from coupling with the far field. An outer expansion involving an $O(1)$ transverse length scale as $b \to 0$ gives a semi-infinite line doublet for this part of the flow. In particular, for an outer limit

$$x, y, z, A \text{ fixed as } a, b \to 0,$$

the appropriate outer expansion is

$$\frac{\Phi_{outer}}{U} = x + ab^2\phi_1(x,y,z) + \cdots. \tag{11}$$

The quantity ϕ_1 solves the following problem:

$$\left.\begin{aligned} &\Delta\phi_1 = \phi_{1xx} + \phi_{1yy} + \phi_{1zz} = 0 \\ &\phi_1(x,r,\theta) \equiv \frac{s^2(x)\cos\theta}{2r} \text{ as } r \to 0 \\ &\phi_{1x}(x,h,\theta) + \beta\phi_{1y}(x,h,\theta) = 0 \end{aligned}\right\} \tag{12}$$

where $r = \sqrt{y^2 + z^2}$, $\tan\theta = z/y$ and the last relation is the approximate form of Darcy's law.

The solution of (12) can be written as

$$\phi_1 = -\frac{1}{4\pi}\frac{\partial}{\partial y}\int_0^\infty \frac{D(\xi)d\xi}{\sqrt{(x-\xi)^2 + r^2}} + \text{wall correction function} \tag{13}$$

where the first term is a line doublet distribution of strength $D(\xi)$ that satisfies the second relation of (12). The wall correction function is needed to satisfy Darcy's law in (12). In (13), the Kutta condition at the effective trailing edge provides the appropriate continuation of the line doublet to downstream infinity and its convergent integral representation. Furthermore, (13) gives upstream influence not present in the inner solutions.

The inner expansion of (13) can be obtained from the $r \to 0$ expansion of its Fourier transform. This gives

$$\phi_1 \equiv \frac{D(x)}{2\pi}\frac{\cos\theta}{r} - \frac{D''(x)}{2\pi}\left\{\frac{r}{2}\log r - \frac{r}{4}\right\}\cos\theta - G''(x)\frac{r}{2}\cos\theta + my + \cdots \text{ as } r \to 0$$

ADA310408

where

$$my \equiv \cos\theta\left\{\frac{D(x_T)r}{2h^2}\lambda - \frac{r}{2\pi h^2}\int_0^{x_T} D'(\xi)d\xi\int_0^{\infty} q\left[\frac{\beta^2(K_0 q + K_1)(I_1 - qI_0) + q^2 I_1 K_1}{\beta^2(qI_0 - I_1)^2 + q^2 I_1^2}\right]\sin\frac{q(x-\xi)}{h}dq\right\}$$

$$-\cos\theta\left\{\frac{\beta r}{2\pi h^2}\int_0^{x_T} D'(\xi)d\xi\int_0^{\infty}\frac{q^2}{\beta^2(qI_0 - I_1)^2 + q^2 I_1^2}\cos\frac{q(x-\xi)}{h}dq\right\}$$

$\lambda =$ 1 for $\beta \neq 1$, (includes porous and closed walls)

$= -1$ for $\beta = 0$, (free jet), (degenerate limit $\beta \to 0$)

$$G(x) \equiv -\frac{1}{4\pi}\int_0^1 D'(\xi)\,\mathrm{sgn}(x-\xi)\log 2|x-\xi|d\xi$$

$$D(x) \equiv \frac{s^2(x)}{2}\alpha$$

(16)

where h is the wall height in units of the body length and the term my in (16) is the wall interaction effect due to the imaging of the doublet in the walls. As an alternate approach for the first term of (13), the integral can be directly expanded for $r \to 0$. This delicate procedure is described in [10]. In the Fourier integral method used, the solution naturally decomposes into a free field (no walls present part) and a wall interaction portion as indicated in (19). Special limiting processes of the singular integrals were developed to handle zero and infinite porosity, corresponding to solid wall and free jet cases respectively. Equation (19) agrees with the results from [1]-[3] in the limit of vanishing chord to tunnel radius ratio. In future work, (19) will be used to compute the **camber effect** associated with non-vanishing chord. To our knowledge, this study has not been made and we believe it is an important factor entering the comparison of our results with experiment to be discussed.

The inner and outer solutions match directly to the orders to be considered here.* This can be shown by expressing each in terms of an intermediate variable r_η. For this purpose, an intermediate limit

$$r_\eta \equiv \frac{r}{\eta(b)} \text{ fixed as } b \to 0, \tag{17}$$

is used to compare the inner and outer representations in an "overlap domain" $r_\eta = O(1)$ in which both expansions are mutually valid. Note in the intermediate limit

*Other applications exist where intermediate expansions is required.

$$r^* = \frac{\eta r_\eta}{b} \to \infty,\ r = \eta r_\eta \to 0,\ \frac{\eta(b)}{b} \to \infty,\ \eta(b) \to 0.$$

The matching process consists of writing inner and outer expansions in terms of the intermediate variable r_η and comparing similar terms to determine unknown elements. Carrying out this process, the two expansions appear as follows in intermediate variables

$$\text{Inner} = ab\left(\frac{s^2(x)}{2\frac{\eta r_\eta}{b}}\cos\theta + O\left(\frac{1}{\left(\eta/b\right)^2}\right)\right) + ab^3 \log 1/b + \varphi_{21}\left(\frac{\eta r_\eta}{b}, \theta\right)$$

$$+ ab^3\left\{-\frac{1}{2}(ss')'\frac{\eta r_\eta}{b}\cos\theta\left(\log \eta r_\eta + \log 1/b\right) + h_2(x)\cos\theta\right\} + \cdots$$

$$\Leftrightarrow \text{Outer} = ab^2\left\{\frac{D(x)}{2\pi}\frac{\cos\theta}{\eta r_\eta} - \frac{D''(x)}{2\pi}\left(\frac{\eta r_\eta}{2}\log \eta r_\eta - \frac{\eta r_\eta}{4}\right)\cos\theta + \left(m - \frac{G''(x)}{2}\right)\eta r_\eta \cos\theta + \cdots\right\}$$

(18)

Based on (18), the following relations hold

$$O\left(\frac{ab^2}{\eta}\right): \qquad \frac{D(x)}{2\pi} = \frac{s^2(x)}{2}$$

$$O(ab^2 \log \eta): \qquad \frac{D''(x)}{2\pi} = (ss')'$$

$$O(ab^2\eta): \qquad \frac{D''(x)}{2\pi}\frac{1}{4} - \frac{G''(x)}{2} = \frac{(ss')'}{4} - \frac{G''(x)}{2} + m \Leftrightarrow h_2(x) \qquad (19)$$

$$O(ab^2\eta \log b): \qquad \text{switchback term}$$

$$\varphi_{21}\left(\frac{\eta r_\eta}{b}, \theta\right) \Leftrightarrow \frac{1}{2}\frac{\eta r_\eta}{b}\cos\theta$$

$$\Rightarrow \varphi_{21} \equiv \frac{1}{2}(ss')' y^* \text{ as } r^* \to \infty$$

Note that in (19) the essential wall interference effect is the additive term m affecting $h_2(x)$ in the $O(ab^2\eta)$ matching relationship. Another viewpoint is from (8b), the solution of which consists of a superposition of its homogenous solution (response to homogenous equation of motion and boundary conditions) and the effects of the forcing terms in the equation of motion and boundary conditions. The homogeneous solution is non-trivial because of the downwash far field associated with the line doublet imaging in the porous walls. Another interesting point is the surprising appearance of switchback terms. These normally are associated with transonic flow. They arise in this subsonic flow from logarithmic elements in the expansions.

The second order inner refinement of the free field lift and pressure distribution comes from the problem (8c) (complemented by a far field condition) for the inner potential φ_2. Techniques used to solve this problem involved matching considerations and exclusion

principles disallowing aperiodic logarithmic parts and removal of unallowed leading edge singularities to maintain finite forces.' The inhomogeneity in the equation of motion was treated by a particular solution φ_f satisfying

$$\frac{\partial^2 \varphi_f}{\partial \sigma \partial \bar{\sigma}} = \left(\mathrm{Im}\left(\sigma - \sqrt{\sigma^2 - s^2}\right)\right)_{cr},$$

where $\bar{\sigma}$ is the complex conjugate of σ. Other solution components are superposed to satisfy the far field boundary condition involving the free field and the wall correction to the downwash. Our analysis resembles that of Wang [11] in some respects who in contrast to our effort did not consider wall interference which is the central thrust of our work. Problems such as (8c) are typical of the transonic case.

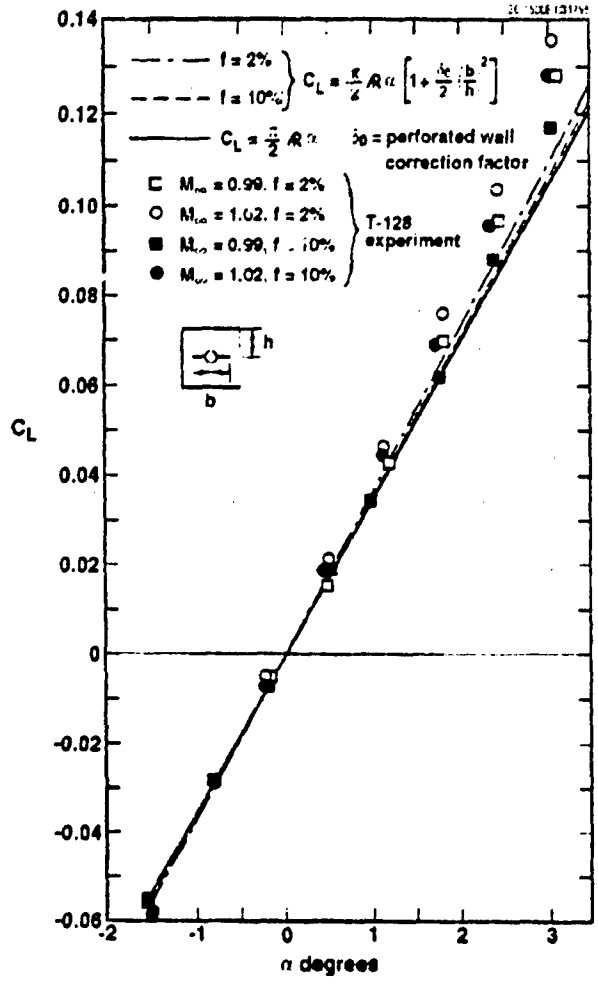

Fig. 3 Comparison of lift interference theory with TsAGI experiment.

'More details will be in our paper to be presented at the 1st AIAA Theoretical Fluid Dynamics Meeting. June 1996, New Orleans, La.

Integration of the pressures on the wing give the following expressions for the lift L. For the free field,

$$\frac{L}{\rho U^2} = b^2 \tan\alpha\, \ell_1 + b^4 \log\frac{1}{b} \tan\alpha\, \ell_{12} + b^4 \tan\alpha\, \ell_2 + \cdots \tag{20}$$

where

$$\ell_1 = \int_{-1}^{1} [\varphi_1]\, dz^* = \pi$$

$$\ell_{12} = \int_{-1}^{1} [\varphi_{12}]\, dz^* = \tfrac{\pi}{2}(ss')'_{\varepsilon=1} \tag{21}$$

$$\ell_2 = \int_{-1}^{1} [\varphi_{21}]\, dz^* = (\ell_{12}/2)(1+\log 2) - \tfrac{\pi}{2}\left(G''_{TE} + s'^2_{TE} + A^2\right)$$

The dominant term for the lift ℓ_1 and pressure distribution agrees with Jones' theory given in [12].

As an experimental validation of the lift interference theory, Fig. 3 compares lift versus angle of attack predicted by the our asymptotic theory with transonic tests of a wing-body combination at TsAGI in Moscow and reported in [9]. It is striking that the incompressible theory agrees so well with the experiment for the high transonic Mach numbers $M = .99$ and 1.02 tested. Plausibility of this finding is related to the elasticity of slender wing theory to not-so-slender planforms as $M \to 1$ as discussed in [13]-[14].

Approximations of wall interaction integrals give the porous wall corrections for wall openness factors $f = 2$ and 10% indicated in the figure. It shows that the experimental trend with increasing f is captured by the lift interference theory for vanishing chord to tunnel radius ratio. However, the comparison with the data shows an increasing slope with incidence not captured by the first order theory. Preliminary indications are that the free field second order effect shows a reduction in lift slope is counter to experimental evidence. It is likely that the reverse trend is due to leading edge viscous separation and vortex formation as well the need to account for the finite chord of the wing. A refinement accomplished is an estimate of the effect of a vortex at the wing-fuselage juncture occurring at higher angles of attack. An oil flow visualization of this phenomenon from the PI's Russian TsAGI experiment reported in [15] is shown in Fig 4. Results from a preliminary model based on conical invariance of the vortex field is shown in Fig. 5. The improvement in agreement is striking and suggestive of the importance of modeling discrete vortex effects. In spite of these, the wall interaction theory shows promise of modeling **relative** trends. As in the blockage theory work for wall height of the order of the body length to be discussed, estimation of the **absolute** levels can be improved independently of the interference estimations using vortex dynamic and leading edge separation approaches such as that just mentioned.

The main point of this effort is that it provides a natural launching pad for extension of the theory to nonlinear transonic flow, accounting for higher approximations, thickness, viscous interactions and finite chord to tunnel height as well as systematic higher order refinement. With the exception of switchback terms and gauge functions, the inner problems for the transonic case are expected to resemble those associated with the incompressible asymptotic theory. However, the outer expansions will solve the three-dimensional Karman-Guderley instead of Laplace equation in the dominant approxima-

tion, and forced versions in the higher orders. However, a major simplification of the usual lifting surface (transonic small disturbance theory) numerical problem is anticipated since the angular variation can be separated out by matching with the inner multipole structure.

Fig. 4. Wing-body-juncture vortex formation in TsAGI wind tunnel.

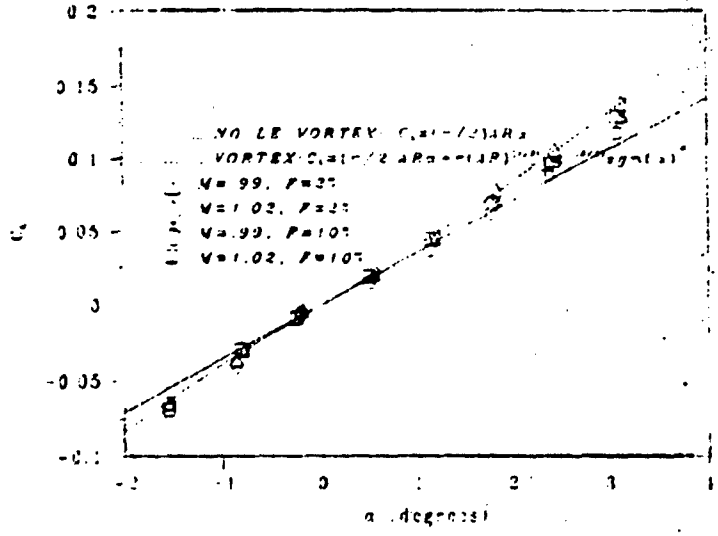

Fig.5 Comparison of vortex improved theory with experiment.

7.3 Extension of large wall-height blockage interference to moderate wall height case

Major thrusts of this work in this phase were

1. Validating a transonic small disturbance model for the flow in a wind tunnel against experimental data

2. Validating the equivalence rule for transonic wall interference.

Referring to Fig. 1, the walls or pressure interface boundary where pressures are assumed to be specified from experiment are at $r = h$, where h is assumed constant for convenience herein (circular test section).* Defining $H = \delta\, h$, the case (*i*) $H = O(1)$ was considered in the research reviewed here, in contrast to the less practical situation (*ii*) in [7] where $H \to \infty$. As will become clear, the asymptotic solution of the Full Potential formulation, for Case (*i*) leads to two, rather than three decks associated with (*ii*), *i.e.*, no wall layer is required, the confined flow consisting only of a nearly axisymmetric "outer" region and a cross flow gradient-dominated inner core which is the near field of the body. In an inner limit in which

$$r^* \equiv r/\delta\ ,\ K \equiv \left(1 - M_\infty^2\right)/\delta^2,\ A \equiv \alpha/\delta \text{ fixed as } \delta \to 0, \tag{22}$$

where α is the angle of attack, δ is the maximum thickness ratio of the equivalent of body of revolution and M_∞ is the freestream or tunnel Mach number which will correspond for convenience to the flight Mach number. The inner expansion (near field) of the slender airplane model $B = r - \delta F(x,\theta) = 0$ is

$$\frac{\Phi_{inner}(x,r,\theta;M_\infty,\delta,\alpha)}{U} = x + \left(2\delta^2 \log\delta\right) S_1(x) + \delta^2 \varphi_1(r^*,\theta\ ;x) + \cdots \tag{23}$$

where $S_1(x)$ is a source strength determined by matching with the outer solution. The inner problem is

$$\Delta_T^* \varphi_1 \equiv \left(r^* \varphi_{1r^*}\right)_{r^*} + \frac{1}{r^{*2}} \varphi_{1\theta\theta} = 0 \tag{24a}$$

$$\frac{\partial \varphi_1}{\partial n} = \frac{FF'(x)}{\sqrt{F^2 + F_\theta^2}} \tag{24b}$$

where n denotes the normal direction to an x=const. cross sectional contour of the surface B=0. Further details are in [13,17]Application of Green's theorem to (24) shows that

$$\varphi_1 \equiv \frac{1}{2\pi} \log r^* \int_0^{2\pi} \frac{F^2}{2} d\theta + \cdots = \frac{A'(x)}{2\pi} \log r^* + \cdots \text{ as } r^* \to \infty, \tag{25}$$

i.e., the asymmetric body appears as a line source in its far field of intensity $A'(x)$ where $A(x)$ is the cross sectional area at the station x of the body B=0. Equation (25) determines $S_1(x)$ in (23) as will be seen in the discussion on matching that follows.

The outer limit (with a slight change in notation from Section 2) is

$$\bar{r} \equiv \delta r,\ K \equiv \left(1 - M_\infty^2\right)/\delta^2,\ \mathrm{A} \equiv \alpha/\delta \text{ fixed as } \delta \to 0. \tag{26}$$

For (26), the appropriate outer expansion is

$$\frac{\Phi_{outer}(x,r,\theta;M_\infty,\delta,\alpha)}{U} = x + \delta^2 \phi_1(x,\bar{r},\theta\ K,\mathrm{A}) + \cdots \tag{27}$$

*All lengths are in units of the body length.

Substituting (27) into the Full Potential equation gives the Karman-Guderley (KG) equation

$$\left(K-(\gamma+1)\phi_{1x}\right)\phi_{1xx}+\left(\tilde{r}\phi_{1\tilde{r}}\right)_{\tilde{r}}=0 \tag{28}$$

Appropriate to the confined case considered in the research, the approximate Darcy law porous wall boundary condition for (28) is

$$\phi_{1\tilde{r}}(x,H,\theta)+\Lambda\phi_{1x}(x,H,\theta)=0, \tag{29}$$

where Λ is the Darcy porosity constant. If experimental pressure data is available on the interface $\tilde{r}=H$, then

$$\phi_1(x,H,\theta)=f(x,\theta) \tag{30}$$

Appropriate inflow and outflow conditions as well as an inner boundary conditions are required to complete the formulation for (28) for subsonic far field. The first of these are discussed in [7]. Gauss' theorem shows a uniform outflow is required as $x\to\pm\infty$ for the solid wall, ($\Lambda=0$ in (29)) which is linearly proportional to the body base area.

As in the unconfined case, the inner and outer expansions can be matched to dominant orders. However, intermediate expansions are required for the higher orders. This was demonstrated for the unconfined case in [13]. Matching is performed in the same manner as in Section 2 using intermediate variables. The appropriate intermediate limit is

$$r_\eta\equiv\frac{r}{\eta(\delta)}\ \text{ fixed as } \delta\to 0. \tag{31}$$

Under (31),

$$r^*=\frac{\eta r_\eta}{\delta}\to\infty,\ \tilde{r}=\delta\eta r_\eta\to 0,\ \frac{\eta(\delta)}{\delta}\to\infty,\ \eta(\delta)\to 0. \tag{32}$$

The inner expansion written in intermediate variables is

$$\frac{\Phi_{\text{inner}}}{U}=x+\underbrace{\left(2\delta^2\log\delta\right)S_1(x)}_{1}+\underbrace{\delta^2\left(\varphi_1^{(R)}\left(\frac{\eta r_\eta}{\delta},\theta;x\right)\right.}_{2}+\underbrace{\frac{A'(x)}{2\pi}\left(\log\eta r_\eta}_{3}-\underbrace{\left.\log\delta\right)\right)}_{4}+\cdots \tag{33}$$

where $\varphi_1^{(R)}$ is the portion of φ_1 that is regular at $r^*=\infty$. Terms 3 and 4 arise from (25). Term 1 in (33) is a switchback term that is needed for matching with the outer expansion. In anticipation of matching, the x derivative terms are assumed small and the solution of the remaining equation

$$\left(\tilde{r}\phi_{1\tilde{r}}\right)_{\tilde{r}}=0,$$

is

$$\phi_1\cong S(x)\log\tilde{r}+g(x)+\cdots \text{ as } \tilde{r}\to 0.$$

This implies that the outer expansion in intermediate variables is

$$\frac{\Phi_{outer}(x,r,\theta;M_\infty,\delta,\alpha)}{U} = x + \delta^2\Big\{S(x)\big(\underset{1'}{\log \eta r_\eta} + \underset{2'}{\log\delta}\big) + \underset{3'}{g(x)} + \cdots\Big\} + \cdots. \tag{34}$$

Matching of Term 2′ in (34) with Term 1+Term 4 in (33) implies that

$$S(x) = S_1(x) = \frac{A'(x)}{2\pi} \tag{35}$$

Also, matching of Term 3′ in (34) with Term (2) in (33) gives

$\varphi_1^{(R)}(r^*,\theta;x) \cong g(x)$ as $r^* \to \infty$.

Finally, Term 1' in (34) matches with Term 3 in (33). From this matching and (35), the appropriate boundary condition to complete the formulation for (28) and (29) or (30) is

$$\lim_{\tilde r\to 0} \tilde r \tilde\phi_1 = \frac{A'(x)}{2\pi}. \tag{36}$$

The pressure on the body can be obtained from substitution of the inner expansion into the exact formula obtained from the energy invariant

$$\frac{a^2}{\gamma-1} + \frac{q^2}{2} = \frac{a_\infty^2}{\gamma-1} + \frac{U^2}{2}. \tag{37}$$

where a is the local speed of sound, U is the freestream velocity and the subscript ∞ refers to freestream conditions. From (37) and isentropy, the pressure coefficient, C_p is

$$C_p \equiv \frac{P-P_\infty}{\frac{\rho_\infty U^2}{2}} = \frac{2}{\gamma M_\infty^2}\left\{\left[1+\frac{\gamma-1}{2}M_\infty^2\left(1-\frac{q^2}{U^2}\right)\right]^{\frac{\gamma}{\gamma-1}} - 1\right\}, \tag{38}$$

where P is the pressure, ρ is the density and $q = |\bar q|$.

Substitution of (23) into (38) gives

$$-\frac{C_p}{2\delta^2} = \frac{A''(x)}{2\pi}\log\delta + \left\{\varphi_{1x} + \tfrac{1}{2}|\nabla_T\varphi_1|^2\right\}_{r^*=F} + \cdots \tag{39}$$

for the pressure on the body, $r^* = F(\theta;x)$, where $|\nabla_T\varphi_1|^2_{r^*=F} = \left\{\varphi_{1r^*}^2 + \frac{\varphi_{1\theta}^2}{F^2}\right\}\Big|_{r^*=F}$. A crucial step for our final conclusion about wall interference comes from the interpretation of (23) and the matching between (33) and (34) and the decomposition

$$\varphi_1 = \underset{1}{g(x)} + \underset{2}{\hat\varphi_1}. \tag{40}$$

Term 1 is a component determined only by the solution of the outer problem (28), (29) or (30) and (36). From (36), it is influenced only by the cross sectional area and not the cross sectional contour of the body at the streamwise station x as well as the wall boundary conditions. By contrast, Term 2 depends solely on the inner boundary value problem (24) and is independent of the wall boundary conditions. **These statements lead directly to the extension of our transonic area rule for wall interference (TARWI)**

from $H \to \infty^*$ **to** $H = O(1)$, *a major impact of this phase of the research.* From this generalization, more practical situations than those for $H \to \infty$ can be considered in which the model distance from the walls is of the order of its length. These are typical of transonic testing. It should be noted that angle of attack effects are higher order for this $A = O(1)$ case as contrasted to $A \to \infty$ cases where they will interact with the near field in the dominant orders through line doublet-wall-imaging/reflection-induced downwash.

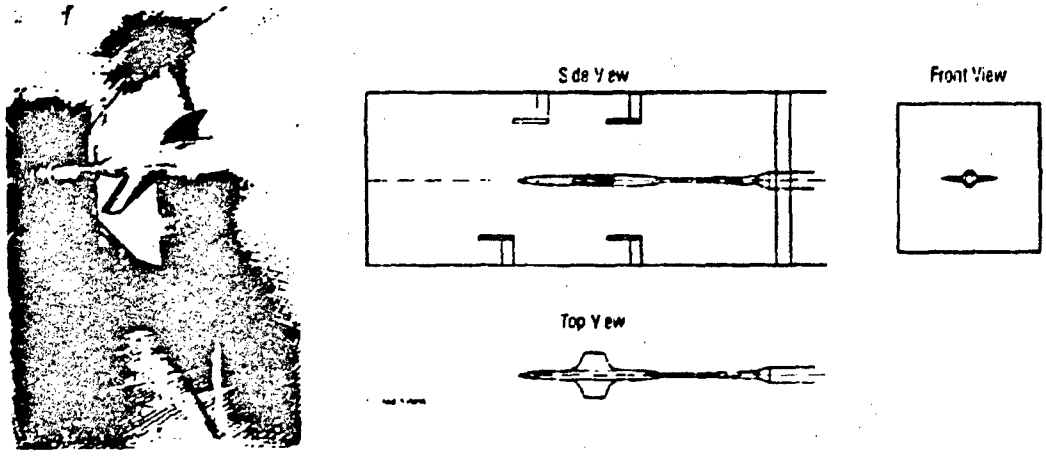

Fig. 6 Wing-body tested in TsAGI T-128 wind tunnel.

7.4 Validations of theoretical and computational simulations for moderate wall height case

Experiments in TsAGI's T-128 wind tunnel in Moscow, Russia, described in [9], have been performed to validate the theoretical work conducted under the contract. Figure6 shows one of the wing-body configurations tested. Results for pressures over the equivalent body of revolution (EBR) for this wing body are shown in Figure 7 that compares the combined asymptotic and numerical method developed in the contract with the TsAGI experiments for the $H = O(1)$ case discussed in the previous section.

The code is quite efficient, requiring only a minute of execution time on a VAX 3100 work station and only 100 iterations to obtain the 2000 iteration fully converged solution. Fig. 7 shows excellent agreement between the theory and experiment. To achieve this fidelity, it was important to accurately simulate the sting model support. This element was necessary to capture the proper recompression process to ambient levels. Additional validations discussed in [9] are that the shock position estimates from [16] agree well with the TsAGI measurements. Work continues on specially designed experiments to adjust

* Enunciated in [7,8]

the level of interference by altering the wall porosity. This will provide a useful database for comparison with the $H=O(1)$ theory.

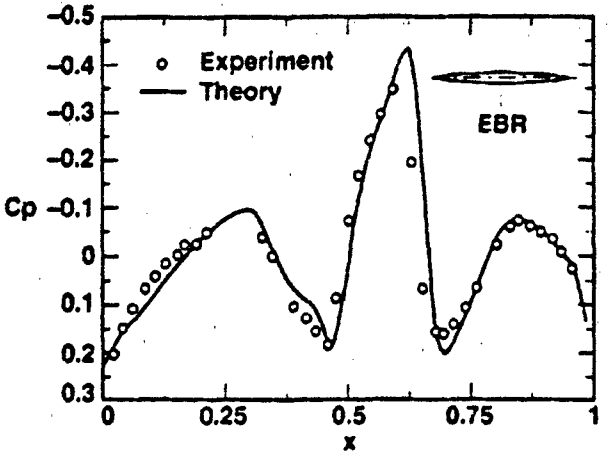

Fig. 7 Comparison of present theory with TsAGI experiment.

In 1995, a larger aspect ratio model was tested in the TsAGI T-128 wind tunnel program. A comparison of the larger aspect ratio wing-body with smaller version is shown in Fig. 8. Figures 9 and 10 compare the drag rise of the smaller and larger aspect ratio wing body WB1 and WB2 respectively with their equivalent bodies EB1 and EB2 for two different wall porosities. These are expressed in terms of the wall openness area ratio, f, which is the area of the wall perforations as a percentage of the test section cross section area. Values of f were 2 and 10% for this study. Figures 9 and 10 are, to the PI's knowledge, the first experimental confirmation of the transonic area rule for wall interference (TARWI) previously discussed, *i.e.*, if

$$\Delta C_D \equiv C_D\big|_{f=10\%} - C_D\big|_{f=2\%}$$

then

$$\Delta C_D\big|_{WB} = \Delta C_D\big|_{EBR} \tag{41}$$

where C_D is the drag coefficient, subscripts WB and EBR denote the wing-body and its equivalent body respectively. Figure 10 shows the TARWI (41) has surprising robustness, *i.e.*, although the aspect ratio of WB2 is considerably larger than WB2, the TARWI (41) still holds near $M_\infty = 1$. This is related to the elasticity of slender body theory to not-so-slender shapes near sonic speeds. It is associated with the coefficient of the x derivative terms in the KG equation (28) being proportional to $M_{local} - 1$ as $M_\infty \to 1$, where M_{local} is the local Mach number. Thus, although the cross flow gradients are no longer $O(1/\delta)$

but $O(1)$ for not-so-slender shapes such as WB2, the x derivative terms are still higher order. Accordingly, the near field remains harmonic in cross flow planes as in the classical slender body theory. Other robustness of (41) should also noted. Although (41) is applicable to $H = O(1)$, the *nominal* H is closer to 0.1 for the Figs. 9 and 10 cases. This is related to the larger length body associated with inclusion of the sting in its definition for the computational modeling. However, if a large part of the sting is at nearly ambient conditions, $H = O(1)$ rather than the nominal $H = o(1)$.

As a final comment, new effort in generalizing the experimental validations of the theory to more realistic configurations has started with 1996 wind tunnel testing of the Tupolev Tu-144 supersonic transport in the TsAGI T-128 program.* One aspect of the work will be investigation of the inlets. The model is modular in the sense that it can be tested with inlet on and off it.

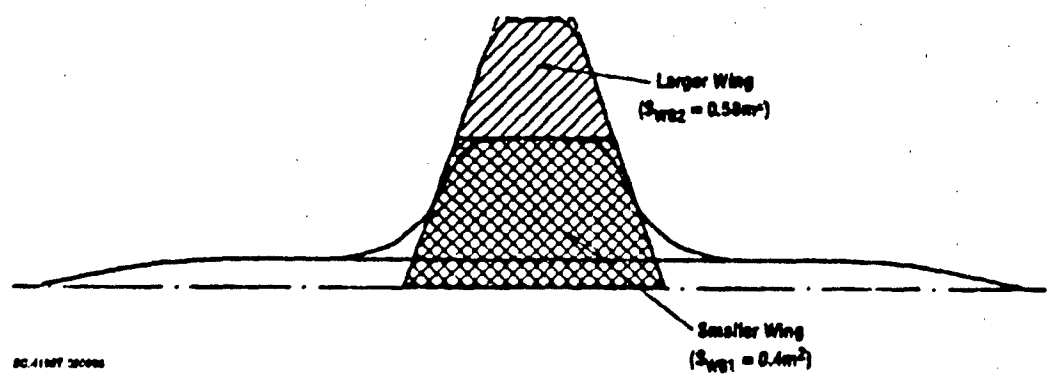

Fig. 8 Wing-body configurations tested.

* A re-engined, refurbished version of this aircraft is being prepared for special U.S.-FSU flight test program to start in April 1996.

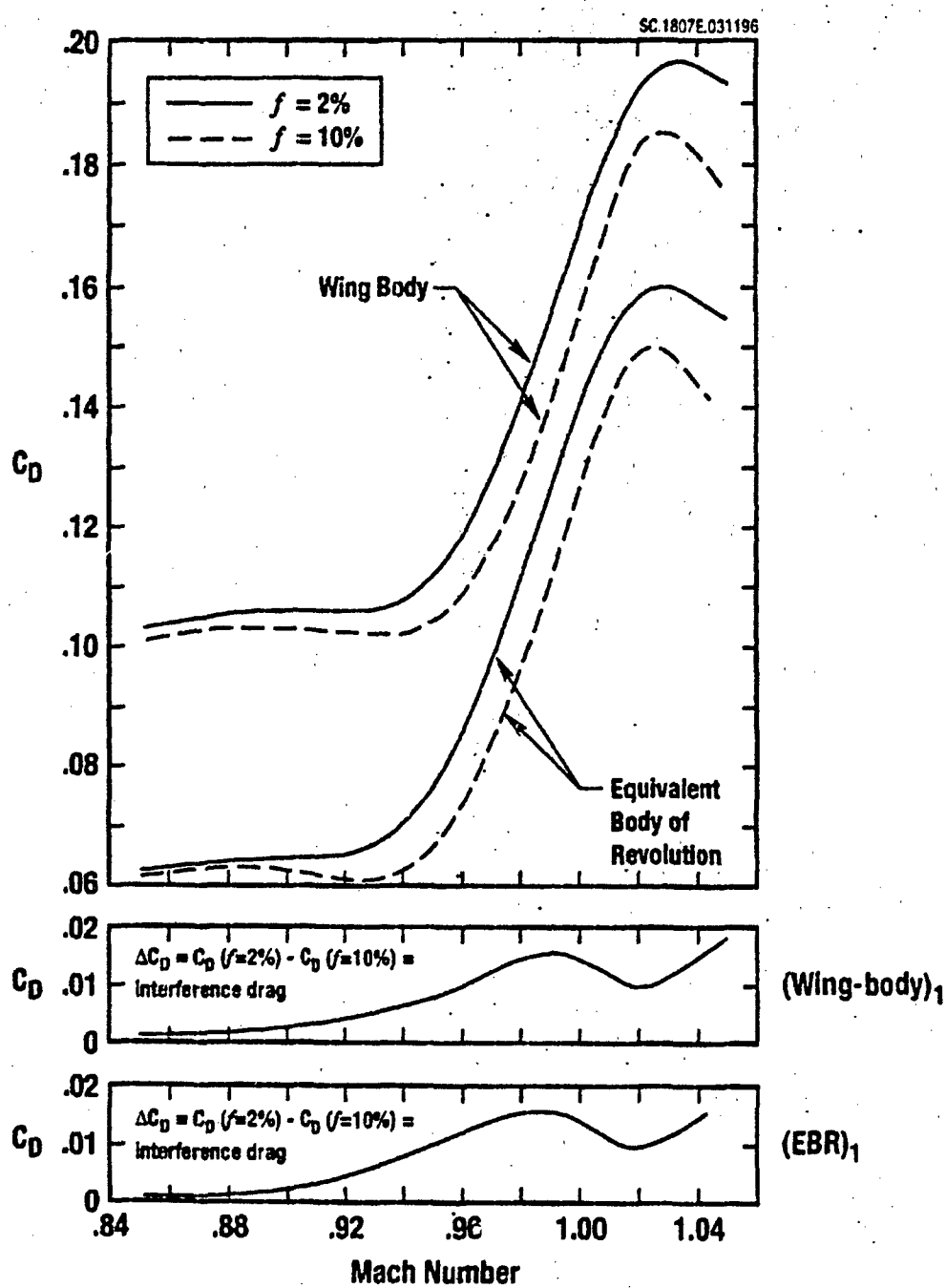

Fig. 9 Comparison of wave drag for wing-body WB1 and its equivalent body EBR1.

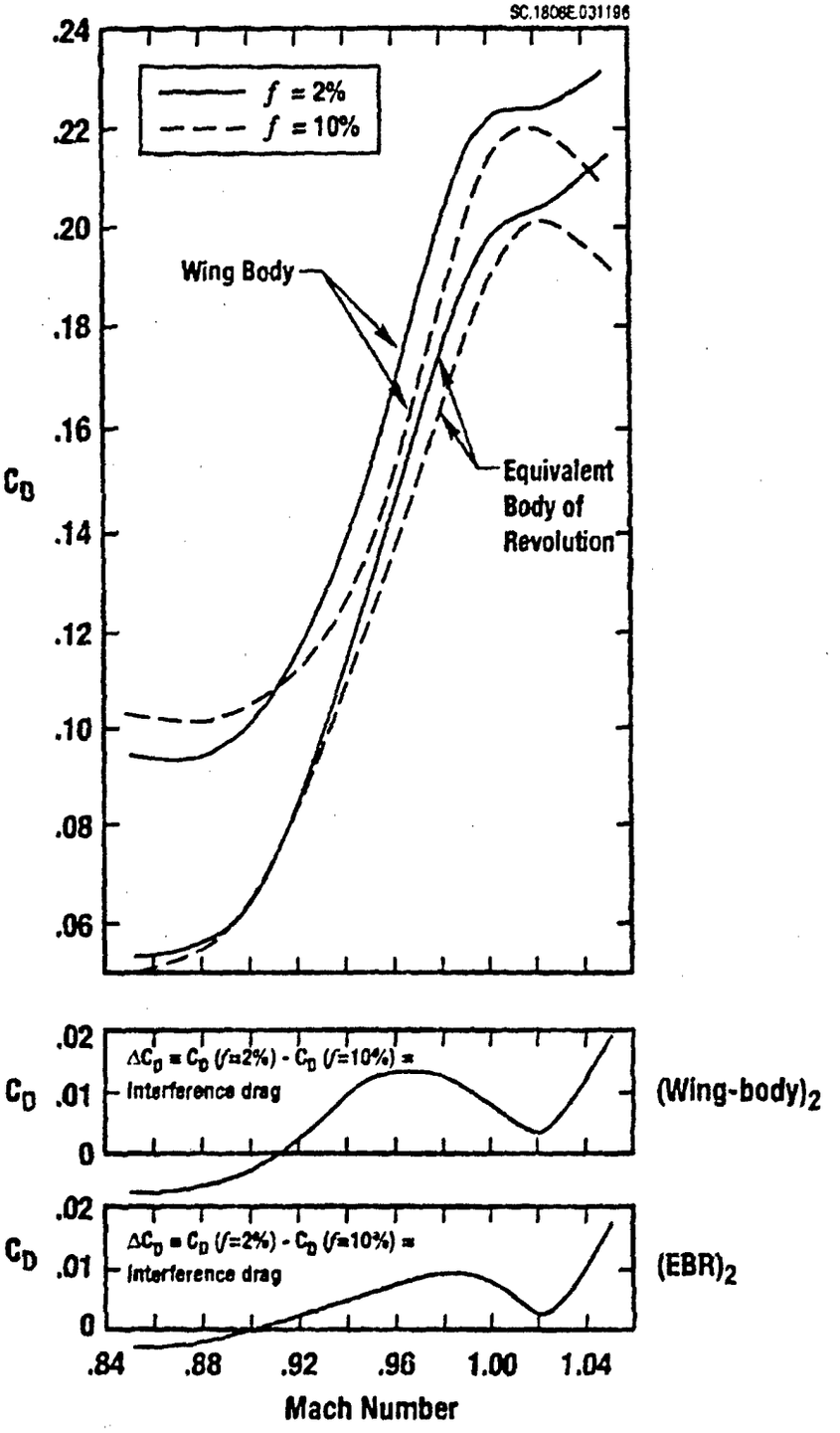

Fig. 10 Comparison of wave drag for wing-body WB2 and its equivalent body EBR2.

7.5 Non-circular wind tunnel sections

Many wind tunnel test sections are non-circular. Typical U.S. installations have octagonal and rectangular test sections. The PI's testing in the T-128 wind tunnel strongly suggests that these non-circular cross sections have only a mild influence on the axisymmetric far field of a slender model tested at transonic Mach numbers. This observation motivated the phase of the research to be described.

If the flow near the walls is subsonic which is the case in transonic flow with a subsonic freestream, it is reasonable to expect rapid elliptic decay of the disturbances inward toward the centerline of the wind tunnel. This contrasts to other cases such as slightly supersonic freestreams, near choking and supersonic bubbles of the unconfined flows penetrating the walls. To explore this hypothesis, the flow inside a test section that is a slight perturbation of circular section will be treated. Figure 11 shows an example of such as perturbation which is an octagon. For generality, the following wall shape .

$$R = h + \varepsilon g(\theta) \tag{42}$$

in which $\varepsilon << 1$ and h is a constant. For specific shapes, it is possible to get an approximate numerical order of magnitude for ε which can be written as

$$\varepsilon = \frac{g_{\max\limits_{0\le\theta\le\frac{\pi}{4}}} - g_{\min\limits_{0\le\theta\le\frac{\pi}{4}}}}{h} \tag{43}$$

Values of ε for square, hexagonal and octagonal test sections are given in Table 1.

Table 1

Section	n	ε
square	4	.414
hexagon	6	.155
octagon	8	.082

These are based on the following relations for an n-sided polygon:

$$\frac{g}{h} = \frac{\sec\left(\theta - \frac{2k\pi}{n}\right) - 1}{\sec\left(\frac{\pi}{n}\right) - 1}, \quad k\frac{\pi}{4} \le \theta \le (k+1)\frac{\pi}{4}, \quad k = 1,2,3,\ldots,n, \tag{44a}$$

$$\varepsilon = \sec\left(\frac{\pi}{n}\right) - 1. \tag{44b}$$

In the first quadrant,

$$k = 0,1,2,3,\ldots,n/4, 0 \le \theta \le \pi/2.$$

Using the polar coordinates previously introduced and referring to Fig. 11, as well as the outer limit (26) and expansion (27) as well dropping the subscript unity notation in ϕ_1, the equation for the perturbation potential in the outer region is

$$\left(K - (\gamma+1)\phi_x\right)\phi_{xx} + +\tilde{r}^{-1}\left(\tilde{r}\phi_{\tilde{r}}\right)_{\tilde{r}} + \tilde{r}^{-2}\phi_{\theta\theta} = 0. \tag{45}$$

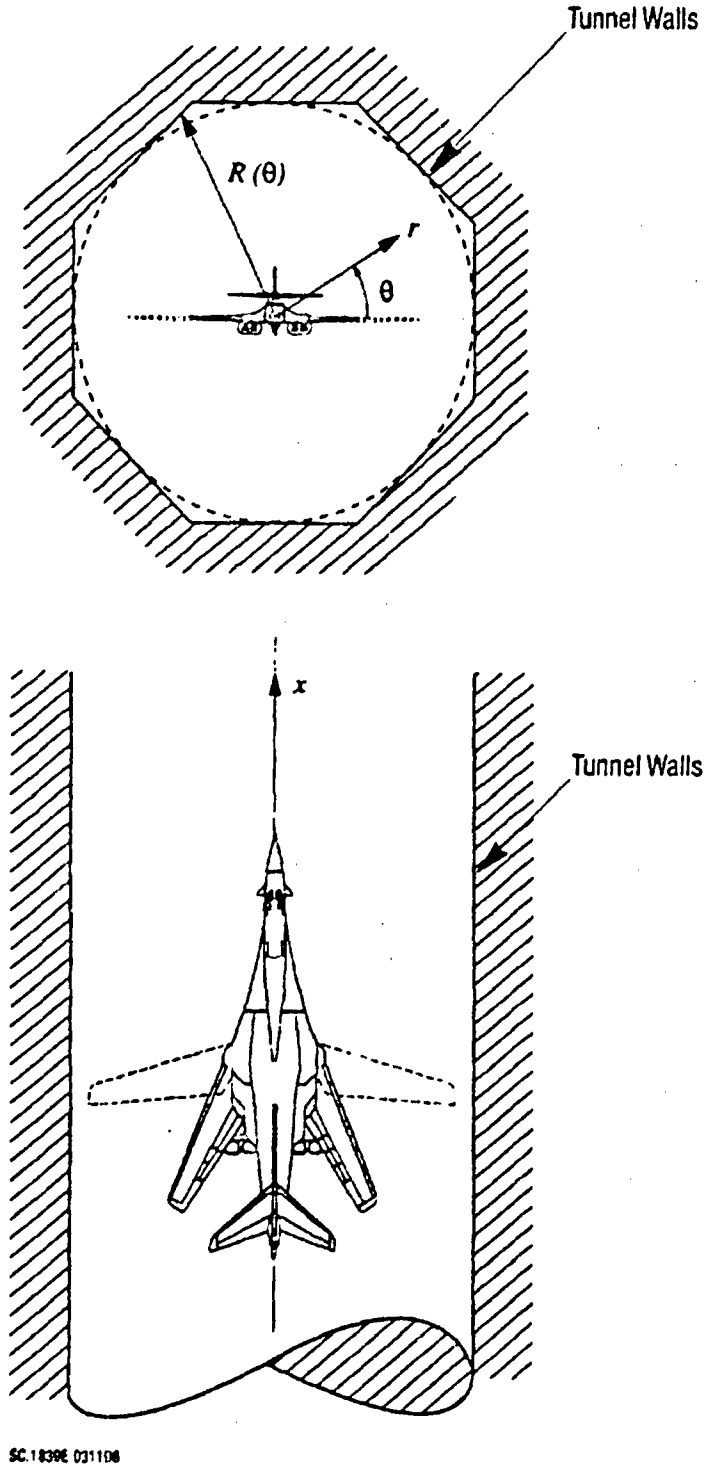

Fig. 11 Schematic of model in non-circular test section.

For convenience, a free jet boundary condition, corresponding to $\Lambda \to \infty$ in (29) is considered. Accordingly, the exact boundary condition

$$C_p(x, R(\theta)) = 0$$

implies

$$\phi_x(x, R, \theta) = 0.$$

Since R is independent of x,

$$\phi(x, R, \theta) = \text{constant}. \tag{46}$$

The constant can be assumed to be zero without loss of generality. Corresponding to (42), the perturbation potential ϕ can be decomposed into the axially symmetric outer part corresponding to $\varepsilon = 0$ and the secondary perturbation associated with the deviation of the walls from a circular cross section. Thus,

$$\phi(x, \tilde{r}, \theta) = \phi_0(x, \tilde{r}) + \varepsilon\phi_1(x, \tilde{r}, \theta) + \ldots \tag{47}$$

Substituting into (45) gives

$$\left\{K - (\gamma+1)\left(\phi_{0_x} + \varepsilon\phi_{1_x} + \ldots\right)\right\}\left(\phi_{0_{xx}} + \varepsilon\phi_{1_{xx}} + \ldots\right) +$$

$$\frac{1}{\tilde{r}}\left(\tilde{r}\left(\phi_{0_{\tilde{r}}} + \varepsilon\phi_{1_{\tilde{r}}} + \ldots\right)\right)_{\tilde{r}} + \frac{1}{\tilde{r}^2}\left(\phi_{0_{\theta\theta}} + \varepsilon\phi_{1_{\theta\theta}} + \ldots\right) = 0,$$

which implies for the respective orders

$$O(1): \left\{K - (\gamma+1)\phi_{0_x}\right\}\phi_{0_{xx}} + \frac{1}{\tilde{r}}\left(\tilde{r}\phi_{0_{\tilde{r}}}\right)_{\tilde{r}} = 0 \tag{48a}$$

$$O(\varepsilon): \left\{K - (\gamma+1)\phi_{0_x}\right\}\phi_{1_{xx}} - (\gamma+1)\phi_{1_x}\phi_{0_{xx}} + \frac{1}{\tilde{r}}\left(\tilde{r}\phi_{1_{\tilde{r}}}\right)_{\tilde{r}} + \frac{1}{\tilde{r}^2}\phi_{1_{\theta\theta}} = 0 \tag{48b}$$

Equation (48b) is the so-called variational transonic small disturbance equation considered in [7,8] in connection with other applications.

Substituting (47) into the boundary conditions near the tunnel centerline gives

$$\lim_{\tilde{r}\to 0} \tilde{r}\phi_{0_{\tilde{r}}} = \frac{A'(x)}{2\pi} \tag{49a}$$

$$\lim_{\tilde{r}\to 0} \tilde{r}\phi_{1_{\tilde{r}}} = 0,$$

where $A(x)$ is the cross sectional area. (49b)

On the (non-circular) cylindrical walls,

$$\tilde{r}_{\text{walls}} = H + \varepsilon g(\theta), \tag{50}$$

a Taylor series expansion for the free jet condition (46) gives

$$\phi(x, H + \varepsilon g + \ldots, \theta) = \phi_0(x, H + \varepsilon g + \ldots) + \phi_1(x, H + \varepsilon g + \ldots, \theta) + \ldots$$

$$= \phi_0(x, H) + \varepsilon\left(g\phi_{0_{\tilde{r}}}(x, H) + \phi_1(x, H) + \ldots\right) + \ldots$$

Equating like orders gives

$$O(1): \phi_0(x, H) = 0 \tag{51a}$$

$$O(\varepsilon): \phi_1(x, H) = -g(\theta)\phi_{0_{\tilde{r}}}(x, H). \tag{51b}$$

A Fourier decomposition to reduce the three-dimensional Transonic Small Disturbance (TSD) problem "P1" (48b), (49b) and (51b) for a wall perturbation from cylindrical to one in two-dimensions is

$$\phi_1 = \sum_{n=0}^{\infty} \phi_{1_n}(x,\tilde{r})\cos n\theta. \tag{52}$$

This decomposition exploits the fact that the only way that asymmetry is introduced into the perturbation problem is through the multiplicative factor $g(\theta)$ in (51b). Note also that the assumption of small perturbations allows the boundary conditions to be transferred from the perturbed surface to the simpler cylindrical test section's. This is essential to the reduction of the dimensionality of the problem. Equation (52) is a **factorization** that reduces the problem P1 to the form

$$\left\{K-(\gamma+1)\phi_{0_x}\right\}\phi_{1_{n_{xx}}} - (\gamma+1)\phi_{1_{n_x}}\phi_{0_{xx}} + \frac{1}{\tilde{r}}\left(\tilde{r}\phi_{1_{n_{\tilde{r}}}}\right)_{\tilde{r}} - \frac{n^2}{\tilde{r}^2}\phi_{1_n} = 0 \tag{51a}$$

$$\lim_{\tilde{r}\to 0}\tilde{r}\phi_{1_{n_{\tilde{r}}}} = 0 \tag{51b}$$

$$\phi_{1_n}(x,H) = \phi_{0_{\tilde{r}}}(x,H)A_n \tag{52c}$$

$$A_n \equiv \tfrac{4}{\pi}\int_0^{\frac{\pi}{2}} g(\theta)\cos n\theta d\theta, (n>0) \tag{52d}$$

$$A_0 \equiv \tfrac{2}{\pi}\int_0^{\frac{\pi}{2}} g(\theta)\cos n\theta d\theta \tag{52e}$$

By (40) and the italicized paragraph following it, the function $g(x)$ which controls the drag and pressure distribution is the only part of the dominant near field that interacts with the dominant outer solution. Since their is no θ dependence in this portion, the only solution of interest of (51a) is that corresponding to n=0. Thus the effect of the higher harmonics A_n for $n>0$ are negligible to this order. Effectively, the angular dependence is "averaged out". **This is another kind of area rule for the effect of slightly asymmetric wall sections.**

To quantify this effect, the mild transonic case corresponding to large K in (51a) was considered. To simplify the analysis, the problem is reduced to a harmonic (incompressible) one by scaling out K by an x transformation and noting that the second and third terms in (51a) are negligible in this approximation. The x transformation is

$$\tilde{x} = x/\sqrt{K} \tag{53}$$

This is equivalent to another procedure that relates the KG to the Prandtl-Glauert (PG) equation from the definition of K in (26) and the fact that the appropriate outer variable for subsonic flow is r rather than $\tilde{r}$ in the KG regime. This gives the reduced PG equation

$$\phi_{1_{n\,xx}} + \frac{1}{r}\left(r\phi_{1_{n_r}}\right)_r - \frac{n^2}{r^2}\phi_{1_n} = 0. \tag{54}$$

where with some redundancy in notation used in a previous section, the transformation

$$X = x/\beta$$

in which

$$\beta \equiv \sqrt{1-M_\infty^2}$$

is used.

The boundary conditions (51b) and (52c) are unaffected by the large K approximation. These relations and (54) constitutes the problem P1′ which can be solved by the exponential Fourier transform pair

$$\overline{\phi_{1_n}} = \int_{-\infty}^{\infty} e^{-ik\alpha}\phi_{1_n}dx \tag{55a}$$

$$\phi_{1_n} = \tfrac{1}{2\pi}\int_{-\infty}^{\infty} e^{ik\alpha}\overline{\phi_{1_n}}dk \tag{55b}$$

The subsidiary equation or Fourier transform of (54) is

$$\frac{d^2\overline{\phi_{1_n}}}{dr^2} + \frac{1}{r}\frac{d\overline{\phi_{1_n}}}{dr} - \left(\frac{n^2}{r^2}+k^2\right)\overline{\phi_{1_r}} = 0. \tag{56a}$$

The transformed boundary conditions are

$$\lim_{r\to 0} r\overline{\phi_{1_n}} = 0 \tag{56b}$$

$$\overline{\phi_{1_n}}(h;k) = A_n \left.\frac{d\overline{\phi_0}}{dr}\right|_{r=h} \tag{56c}$$

Equations (56) lead to the solution

$$\overline{\phi_{1_n}} = \frac{A_n}{2\pi}\int_{-\infty}^{\infty} \frac{I_n(kr)}{I_n(kh)}\left.\frac{d\overline{\phi_0}}{dr}\right|_{r=h} e^{ikX}\,dk. \tag{57}$$

where I_n denotes the modified Bessel function of the second kind of n^{th} order. Equation (57) can be further simplified from the solution for the transform of a similar boundary value problem to P1′ for ϕ_0. This gives

$$\left.\frac{d\overline{\phi_0}}{dr}\right|_{r=h} = \frac{\overline{A'}}{2\pi}\left\{\frac{K_0(kh)I_1(kh)+K_1(kh)I_0(kh)}{I_0(kh)}\right\} = \frac{\overline{A'}}{2\pi h I_0(kh)}, \tag{58}$$

where the Wronskian relation is used to get the third member of the equality. The difference of the non-circular and circular cross section wind tunnel pressures on a body is given by the formula

$$\Delta C_p \equiv C_p\big|_{\varepsilon\neq 0} - C_p\big|_{\varepsilon=0} = -2\varepsilon\delta^2\left(g_1'(x)-g_0'(x)\right) = -2\varepsilon\delta^2\phi_{10_x}(x,0), \tag{59}$$

where the g_i $(i=0,1)$ are the $O(1)$ terms of the inner $(r\to 0)$ expansion of the outer solutions for ϕ_{1_0} and ϕ_0 respectively, and δ is the maximum thickness ratio of the body. The $\phi_{1_{n_x}}(x,0)$ for $n\neq 0$ do not contribute in (59) since

$$I_0(0) = 1,$$

$$I_n(0) = 0,\ n>0.$$

Finally, from the Convolution Theorem, (57) and (58), the change in the body pressures due to wall asymmetry ΔC_p is

$$\Delta C_p = \frac{\delta\varepsilon}{\beta\pi^2 h} A_0 \int_0^{\beta^{-1}} A'(\xi) d\xi \int_0^{\infty} \frac{\sin k(X-\xi)}{I_0^2(kh)} dk. \tag{60}$$

To illustrate (60), a parabolic arc body of revolution inside a square cross section tunnel is considered. For this case

$$r_b(x) = \delta x(1-x), 0 \le x \le 1,$$

where r_b is the body radius. Accordingly,

$$A = \pi r_b^2 = \pi\delta^2\left(x^2 - 2x^3 + x^4\right) \tag{61}$$

and

$$A_0 = \frac{2^{-1/2}}{\left(\sqrt{2}-1\right)\pi}\left\{\log\left(\frac{\tan\frac{3\pi}{8}}{\tan\frac{\pi}{8}}\right) + \frac{\pi}{2}\right\} = 1.81. \tag{62}$$

Figure 12 shows the effect of increasing Mach number on the normalized correction of the pressures from a circular to a square test section, $\Delta\tilde{C}_p$, where,

$$\Delta\tilde{C}_p \equiv -\frac{\Delta C_p}{\frac{\delta\varepsilon}{\beta\pi^2 h} A_0}, \tag{63}$$

when $h=1$ for a parabolic arc body, *i.e.*, the tunnel average radius is equal to the body length. Note that although the body is in the interval $0 \le x \le 1$, wall asymmetry influences the flow considerably upstream of the body nose. Moreover, the largest effects appear at the nose and tail of the body and the correction increases with Mach number as expected. Another observation is the rapid upstream and downstream decay of the effect. This is consistent with the flow ellipticity. Lastly and most important is the smallness of the effect which is in sharp contrast with the results for $h=.5$ which shows a dramatic ten-fold increase with merely halving the wall height. This effect is brought out in Figs. 13 and 14 for $M_\infty=0$ and .7 respectively. In accord with expectations, Fig. 15 shows that compressibility increases the change in pressure associated with wall asymmetry.

7.6 Summary, conclusions and recommendations

Development under the contract effort and related work of a number of unique and useful tools to the wind tunnel test engineer has been described in the previous sections. These are:

1. Extension of the area rule for blockage interference to wall heights of the order of the body length.
2. A systematic asymptotic theory for lift interference.
3. Simplified corrections for asymmetric deviations of circular wind tunnel sections.
4. Emerging database for transonic wall interference theories from Russian tests. Items 1 and 2 apply to porous wind tunnels. Item 3 can be readily extended to such sections.

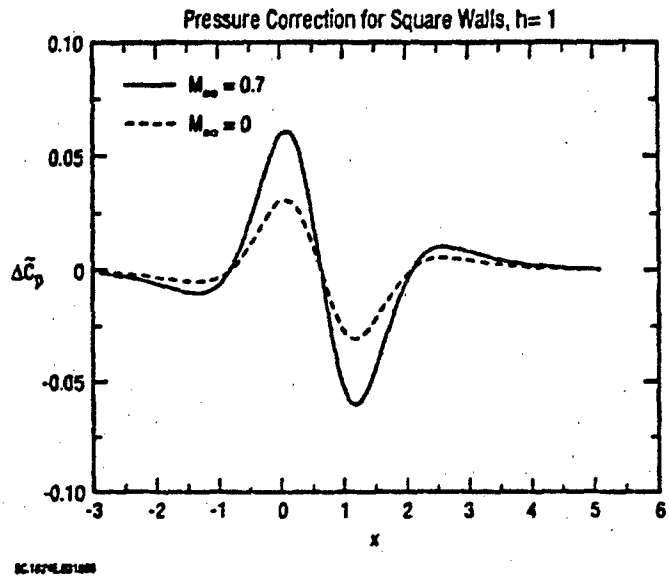

Fig. 12 Pressure corrections from circular to square test sections, parabolic body, $h=1$.

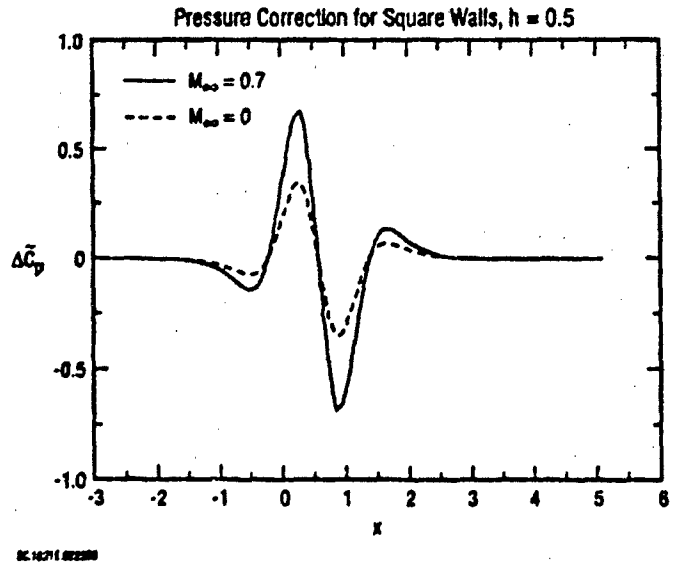

Fig. 13 Pressure corrections from circular to square test sections, parabolic body, $h=.5$.

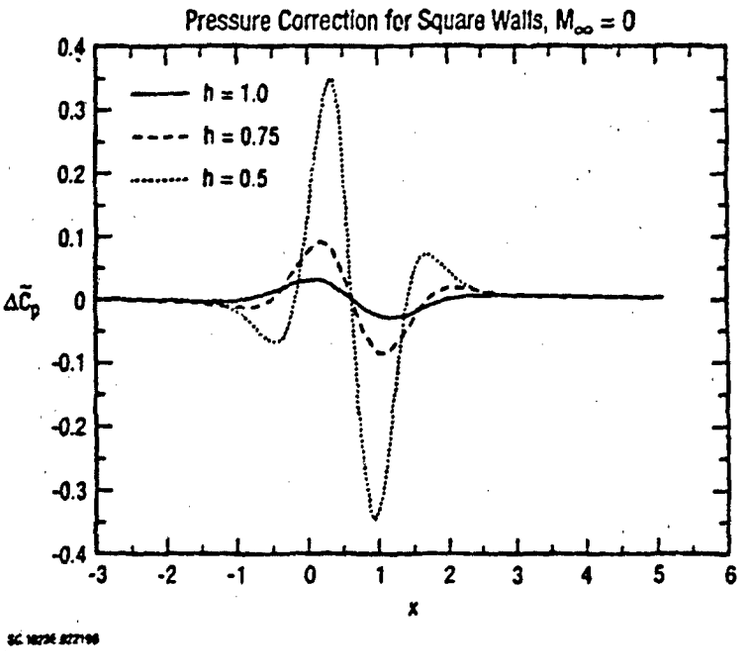

Fig. 14 Pressure corrections from circular to square test sections, parabolic body, effect of h for M_∞=0.

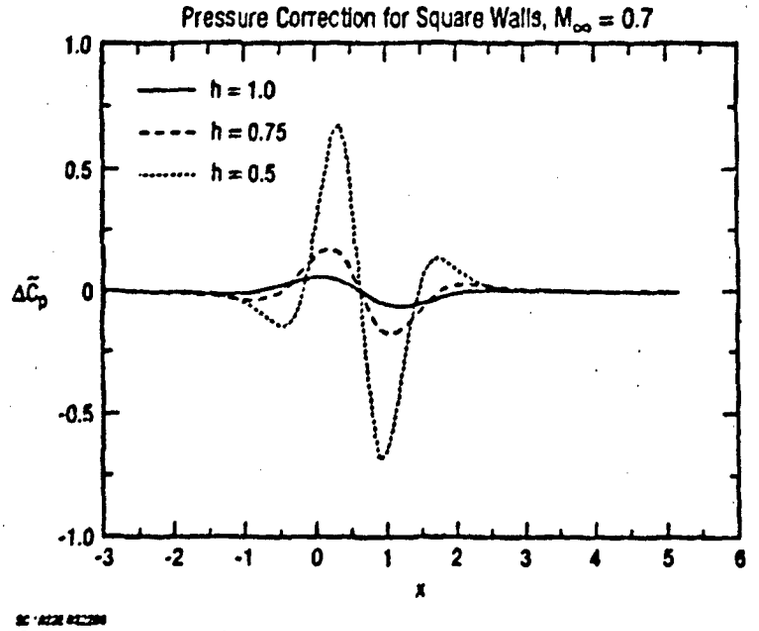

Fig. 15 Pressure corrections from circular to square test sections, parabolic body, effect of h for M_∞=.7.

The ultimate impact of this work is to

- Reduce computational intensity of transonic wall interference estimation.
- Help optimize model sizing to maximize test Reynolds number while minimizing wall interference.
- Provide a quick means of extrapolating ground tests to free flight.

To enhance the utility of these tools the following further effort is recommended:

- Apply Items 1 and 2 to corrections to drag polars
- Extend Item 2 to transonic flow, moderate chords, and thickness
- Extend Item 3 to the moderate K case.
  - Strong evidence exists that the $n=0$ solution of (51a) is appropriate to the strongly nonlinear transonic case. The argument is similar to that following (59).
  - It is envisioned that $\delta'(x)$ "spiky" behavior of the variational solution near shocks will be the principal modification of the solutions previously discussed for the high subsonic large K case.
  - Validation of the subsonic solutions against the exact eigenfunction and elliptic function Green's functions should be performed

7.7 References

1. Goodman, T.R., "The Porous Wind Tunnel, Part IV, Subsonic Interference Problems in a Circular Tunnel," Cornell Aeronautical Laboratory Report AD-706-A-2, 1951.

2. Baldwin, B.S. and Turner, J.B., "Wall Interference in Wind Tunnels with Slotted and Porous Boundaries at Subsonic Speeds," NACA TN 3176, May, 1954.

3. Pindzola, M. and Lo, C.F., "Boundary Interference at Subsonic Speeds in wind Tunnels with Ventilated Walls," U.S. Air Force Arnold Engineering Report, AEDC-TR-69-47.

4. Kraft, E.M., Ritter, A. and Laster, M., "Advances at AEDC in Treating Transonic Wind Tunnel Wall Interference," presented at the 15th Congress of the International Council of Aeronautical Sciences, London, U.K., ICAS Paper, 86-1.6.1, September 9-12, 1986.

5. Newman, P.A., Kemp, W.B., and Garriz, J.A., "Wall Interference Assessment and Corrections," Transonic Symposium, Theory, Application and Experiment, NASA CP-3020, 1988, pp. 817-852.

6. Sickles, W.L. and Erickson, J.C., "Evaluation of Wall Interference and Correction Techniques," AEDC Report TR-87-45 AD-A195873, June 1988.

7. Malmuth, N.D., Wu C.C., Jafroudi, H. Mclachlan, R. Cole, J. and Sahu, R. , "Asymptotic Theory of Transonic Wind Tunnel Wall Interference," Air Force Systems Command, Arnold Air Force Base, Arnold Engineering Development Center Report AEDC-TR-91-24, December 1991.

8. Malmuth, N.D., Jafroudi, H. Wu, C., Mclachlan, R. and Cole, J. "Asymptotic Methods Applied to Transonic Wall Interference," *AIAA J.* **31** 5, pp.911-918, May 1993.

9. Malmuth, N.D. Neyland, V.M., and Neiland, V. Ya."Wall Interference Over Small and Large Aspect Ratio Wings in Wind Tunnels," *invited paper*, Second Pacific International Meeting in Aerospace Technology PICAST2-AAC6, *in proceedings*, Melbourne, Australia, March 1995.

10. Kevorkian, J. and Cole, J., *Perturbation Methods in Applied Mathematics*, Springer-Verlag, New York, 1980.

11. Wang, K.C. "A New Approach to Not-So-Slender-Wing Theory," *Studies in Applied Math* **4**, 1968, pp.391-406.

12. Jones, R.T., "Properties of Low-Aspect Ratio Pointed Wings at Speeds Below and Above the Speed of Sound," NACA Report 835, 1946.

13. Cole, J.D. and Cook, L.P., *Transonic Aerodynamics*, North Holland, N.Y., 1986.

14. Adams, M.C. and Sears, W.R., "Slender-Body Theory, Review and Extension," *J. Aero. Sci.*, 1953, pp. 85-98.

15. Neyland, V.M. and Neiland V. Ya, "Special Features of Transonic Flows Over Models RI-1 and RI-2 in a Wind Tunnel and Infinite Flow," Final Report B4563029, 1994.

16. Malmuth, N.D. "Some Applications of Combined Asymptotics and Numerics in Fluid Dynamics and Aerodynamics," invited chapter in *Frontiers in Applied Mathematics (SIAM), and Numerical Methods for Partial Differential Equations with Critical Parameters, (AGARD)*, Kluwer Press, H.G. Kaper and M. Garbey, ed., Dordrecht, Holland, 1993, pp.53-79.

17. Malmuth, N.D. "An asymptotic theory of wind-tunnel-wall interference on subsonic slender bodies," *J. Fluid Mech.* **177** 1987 , pp. 19-35.

8. Significance, Impacts of Research, Recommendations and Future Work

Various aspects of hypersonic stability and transition as well transonic wall interference problems have been addressed in the effort previously described. Major observations are:

1. Solutions exhibiting a **special waveguide behavior** not previously studied reveal disturbance amplification and transition mechanisms in which acoustic disturbances reflect against the edge of the boundary layer as if it were a solid wall. Similar phenomena occur in the region between the edge of the shock and the boundary layer sonic line. This work is an outgrowth of the previous effort of the Principal and Co-Investigators concerning nonparallel and shock effects in hypersonic boundary layers as well as waveguide energy trapping **that are not modeled by current state-of-the-art stability or transition prediction codes.** These mechanisms compete with conventional processes such as amplification of Tollmein Schlichting waves and crossflow instabilities as paths to transition. Our identification of this physics should be useful to designers and engineers. They also will be helpful in pre and post processing of direct-simulations and interpretation of such solutions. It is recommended that the waveguide solutions be extended to three-dimensional flows and that unit experiments be performed to validate the results of our theoretical analyses such as those that have been initiated by Maslov and his IPTAM group in Novosibirsk.

2. We have developed an **unsteady Newtonian shock layer theory** to treat aeroelastic and unsteady aerodynamic effects as well as finite amplitude hypersonic stability. From this model we have discovered inflectional instabilities that can be exploited to enhance scramjet combustor burning processes.

3. The initial boundary value problem of **hypersonic three-dimensional unsteady stability has been considered within an asymptotic framework for the first time to our knowledge.** A major contribution is the response of a point vibrator. We recommend that comparable experiments be performed using the IPTAM spark discharge technique. Our work contrasts with previous **two-dimensional** analyses such as (Neiland 1970, Brown and Stewartson 1975) for the viscous steady case or (Malmuth 1993, Blackaby *et al.*, 1993) for unsteady inviscid flow. Perturbations within the framework of an initial boundary-value problem instead of the conventional eigenproblem provide important insight into the space-time evolution of instabilities and receptivity. A significant impact is that it reveals other instability paths besides Tollmein-Schlichting, cross-flow, bypass types and those mentioned in Item1. The main feature is global interaction between shock and boundary layers as well as the role of strong wall cooling in such interactions. Additionally, we have shed further light on the role of three-dimensionality in connection with upstream influence in hypersonic strong interactions since the (Neiland 1970, Brown and Stewartson 1975) studies. With this new knowledge, it is possible to dilineate regions

of influence from three-dimensional perturbation sources. For steady and low frequency fluctuations, the most intensive influence appears in the downstream wake within the downstream Mach cone. At high frequencies, effects are concentrated on the source axis.

This theory gives improved basic understanding of the interaction of separation, stability and transition. The practical implication for hypersonic vehicle design is that shock interference heating induced by different devices within the boundary layer and strong separation can be reduced by techniques suggested by our triple-deck models. Moreover, instabilities and other unsteady effects can be exploited to enhance mixing for scramjet propulsion such as with vibrating elements with tailored or maximized receptivity. In addition, our analyses could with further development provide engineers and designers manufacturing and flow quality tolerances for surface roughness, such as near leading edges.

We recommend that increased understanding of disturbance propagation from this phase of the work be used to improve computational schemes. They could suggest stable and fast running algorithms for hypersonic interactive flows with strong ellipticity such as shock-boundary layer interactions, and even separated "self-interaction" flows behind a body flap or spoiler. Other recommended generalizations that appear within our grasp are more complex flows involving chemical reactions and radiation.

5. Our asymptotic formulations give basic similitudes that we have applied to collapse hypersonic cone transition data to universal curves which is the basis of fast preliminary design-oriented aerodynamic and heat transfer prediction methods. We recommend that our procedure be extended to handle bluntness. This is a major gap in the design of reusable launch vehicles such as the X-33.

6. From a new stability analysis with application of a Darcy law boundary condition, we have obtained strong evidence that absorbing walls such as those associated with thermal protection systems (TPS) can quench second-mode inviscid instabilities within hypersonic boundary layers. We recommend that the approach be generalized to viscous disturbances. Ground and flight experimental validations of the benefits should be performed so that a practical system can be developed.

7. At transonic speeds, our transonic area rule for wall interference (TARWI) was extended from cases where the wall height parameter in units of the model length $h = o(1)$ to $h = O(1)$. We have performed experiments in Russia in the TsAGI T-128 wind tunnel that validate this rule. It reduces the problem for transonic blockage interference from three to a two-dimensions. We have also applied matched asymptotics to provide a consistent approximation scheme to estimate porous wall lift interference corrections. This theory has been refined in our effort to account for the influence of concentrated wing-body juncture vortices that give nonlinearities in the variation of lift with incidence. A recommended refinement is to generalize the

approximations in the same fashion as those for blockage, *i.e.*, the lift interference theory assumed that $h = o(1)$. Extension to $h = O(1)$ will give a camber effect associated with the variable tunnel induced upwash field along the model length. An immediate output of our wall interference model is that it can be used to extrapolate polars from the wind tunnel to free flight or another facility. The TARWI allows this estimation to be made without the need for a large scale CFD process involving significant gridding pre-processing. Instead, only a desktop computation is required to obtain the nonlinear blockage effect. This will help optimize model sizing to maximize test Reynolds number while minimizing wall interference. Further validations and extensions of the theory are planned such as our imminent tests of a 4% Tupolev supersonic transport Tu-144 model in the TsAGI T-128 wind tunnel in the near future. A three view of this configuration and the location of the pressure taps are shown in Figs. 1 and 2.

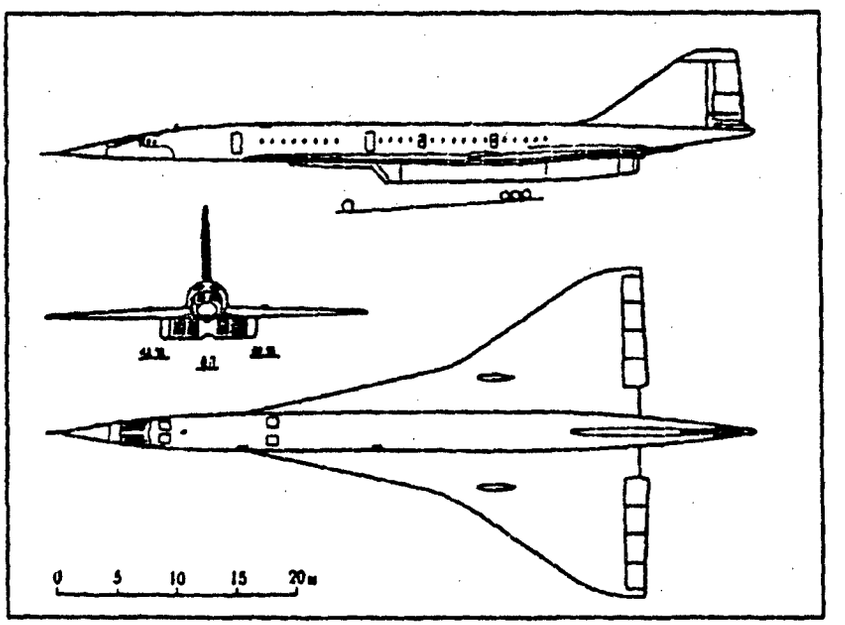

Fig. 1 Tu-144 three-view.

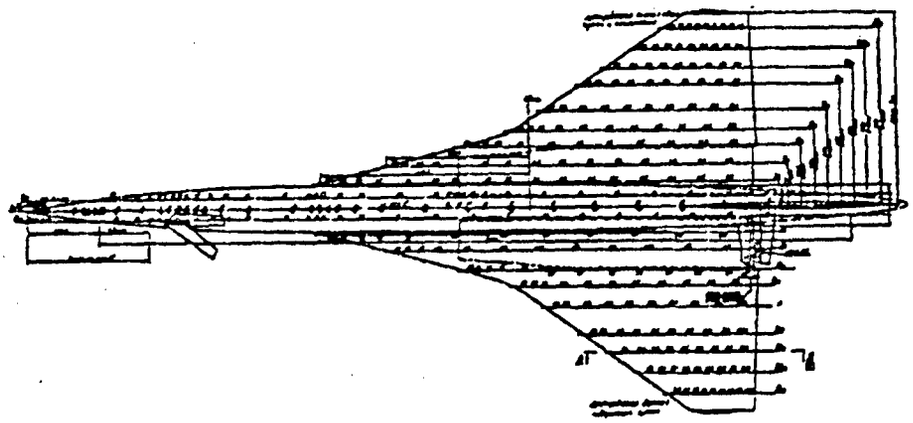

Fig. 2 Tu-144 4% model.